Deutsche Geodätische Kommission
der Bayerischen Akademie der Wissenschaften

Reihe C | Dissertationen | Heft Nr. 728

Alexander Schunert

Assignment of Persistent Scatterers to Buildings

München 2014

Verlag der Bayerischen Akademie der Wissenschaften
in Kommission beim Verlag C. H. Beck

ISSN 0065-5325 ISBN 978-3-7696-5140-9

Diese Arbeit ist gleichzeitig veröffentlicht in:
Wissenschaftliche Arbeiten der Fachrichtung Geodäsie und Geoinformatik der Leibniz Universität Hannover
ISSN 0174-1454, Nr. 311, Hannover 2014

DGK Deutsche Geodätische Kommission
der Bayerischen Akademie der Wissenschaften

Reihe C Dissertationen Heft Nr. 728

Assignment of Persistent Scatterers to Buildings

Von der Fakultät für Bauingenieurwesen und Geodäsie
der Gottfried Wilhelm Leibniz Universität Hannover
zur Erlangung des Grades
Doktor-Ingenieur (Dr.-Ing.)
genehmigte Dissertation

von

Dipl.-Ing. Alexander Schunert

München 2014

Verlag der Bayerischen Akademie der Wissenschaften
in Kommission bei der C. H. Beck'schen Verlagsbuchhandlung München

ISSN 0065-5325 ISBN 978-3-7696-5140-9

Diese Arbeit ist gleichzeitig veröffentlicht in:
Wissenschaftliche Arbeiten der Fachrichtung Geodäsie und Geoinformatik der Leibniz Universität Hannover
ISSN 0174-1454, Nr. 311, Hannover 2014

Adresse der Deutschen Geodätischen Kommission:

Deutsche Geodätische Kommission

Alfons-Goppel-Straße 11 ● D – 80 539 München

Telefon +49 – 89 – 23 031 1113 ● Telefax +49 – 89 – 23 031 - 1283 / - 1100

e-mail hornik@dgfi.badw.de ● http://www.dgk.badw.de

Prüfungskommission

Referent:	Prof. Dr.-Ing. Ingo Neumann
Korreferenten:	Prof. Dr.-Ing. Christian Heipke
	Prof. Dr.-Ing. Steffen Schön
	Prof. Dr.-Ing. Uwe Sörgel

Tag der mündlichen Prüfung: 27.01.2014

© 2014 Deutsche Geodätische Kommission, München

Alle Rechte vorbehalten. Ohne Genehmigung der Herausgeber ist es auch nicht gestattet,
die Veröffentlichung oder Teile daraus auf photomechanischem Wege (Photokopie, Mikrokopie) zu vervielfältigen

ISSN 0065-5325 ISBN 978-3-7696-5140-9

Erklärung

Ich erkläre, dass ich die vorliegende Dissertation selbständig verfasst habe, die benutzten Hilfsmittel vollständig angegeben sind und die Dissertation nicht als Diplomarbeit, Masterarbeit oder andere Prüfungsarbeit verwendet wurde. Weiterhin erkläre ich, dass ich keine anderen Promotionsgesuche eingereicht habe.

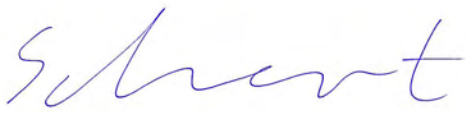

Hannover, 15. November 2013

Statement

I hereby declare that I am the sole author of this thesis. I have fully acknowledged the work of others in this dissertation. This thesis has not been submitted as a Diploma thesis, Master thesis or as any other written examination. Furthermore, I declare that I have not submitted any other application for a doctorate.

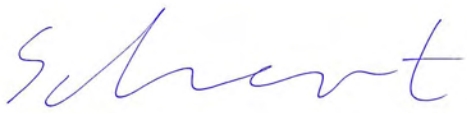

Hannover, 15th November 2013

Abstract

Persistent scatterer interferometry (PSI) is a technique to monitor millimeter scale surface deformation from space using stacks of synthetic aperture radar (SAR) images. The method relies on the identification of point scatterers that show temporally stable reflection properties. Those point scatterers are referred to as as persistent scatterers (PS). As PS are predominantly found at man made structures, PSI is especially suited for urban areas. Using data of the highest resolution, as provided by the TerraSAR-X or the COSMO-Skymed satellite, a plethora of PS is potentially available per structure. That renders the monitoring of single buildings feasible. The spatial distribution of the PS exhibits regular patterns at frontages caused by the rectilinear arrangement of facade details (e.g. windows) that induce the PS. Those spatial regularities contain information that is very useful for PS processing.

The main focus of this thesis lies on the assignment of PS to buildings using a three-dimensional city model. A method for the assignment of the PS to the bounding surfaces of this three-dimensional city model is proposed. The main aim of the conducted experiments is the identification of effects hampering such assignment. It turns out that PS and map data compare well at the facades but less so at roofs. The latter is mostly due to generalization issues, which are more pronounced at housetops. One of the major findings is the presence of PS inside of buildings. The physical nature of such PS remains unknown. However, such PS could cause major problems in the interpretation of deformation results.

In order to allow for an assignment of the PS to the bounding surfaces of the city model, an approach for the alignment of both datasets is proposed. This approach is based on an Iterative Closest Plane algorithm, which is adapted to the specific characteristics of PS point clouds. The plausibility of the results is demonstrated in case studies and based on the convergence behavior of the iterative procedure.

The number and distribution of the PS depends on the scene and cannot be chosen to match the monitoring demands. This is one of the major drawbacks of PSI. As a result, actual deformation may remain unidentified. In order to mitigate this issue, the established relations between PS and city model are used to compile a map of the PS density per building face. Although this does not solve the underlying problem, it enables the identification of structures that are not properly sampled. This density map is used to identify some of the main factors influencing the PS density. Those factors are discussed in detail using case studies.

In order to utilize the spatial arrangement of PS along facades, a production system that focuses on the identification of regular horizontal patterns of PS is proposed. The obtained results are quite heterogeneous. At some facades, many groups can be identified, while at others hardly any patterns can be detected. This is mostly due to layover effects, which can disturb regular patterns considerably. The obtained grouping information can be used to improve the height estimate of each pattern. In order to determine this height, the weighted mean value of the heights of the single PS contained in each group is used. The expected precision gain is assessed on a theoretical basis starting from the Cramer-Rao Lower Bound (CRLB) of a single height estimate by means of error propagation.

Finally, the vertical distances between PS groups and horizontal structures in light detection and ranging (LIDAR) data are evaluated. The aim of this study is the assignment of PS to real world structures, which are represented by the LIDAR data. The study is limited to the facades of two buildings featuring a very simple setup.

Zusammenfassung

Persistent Scatterer Interferometrie (PSI) ist eine Methode zur Erfassung von Deformationen der Erdoberfläche im Millimeterbereich mithilfe eines Stapels von SAR-Bildern. Die Technik beruht auf der Erkennung von Punktzielen mit zeitlich konstanten Reflexionseigenschaften. Diese Punktziele werden als Persistent Scatterer (PS) bezeichnet. Da PS überwiegend an künstlichen Objekten zu finden sind, ist die Technik vor allem für die überwachung von Städten geeignet. Die Anzahl von PS pro Gebäude ist üblicherweise recht groß, wenn hochauflösende SAR-Daten (z.B. TerraSAR-X oder COSMO-Skymed Spotlight-Daten) verwendet werden, so dass eine Überwachung einzelner Gebäude auf Basis von PSI möglich erscheint. Die PS zeigen oft regelmäßige Muster an Fassaden, was durch die rechtwinklige Anordnung der Strukturen bedingt wird, die diese PS erzeugen. Diese Regelmäßigkeiten enthalten Information, die für die PS-Auswertung nützlich sind.

Der Schwerpunkt dieser Arbeit ist die Zuordnung von PS zu Gebäuden unter Zuhilfenahme eines dreidimensionalen Stadtmodells. Es wird eine Methode entwickelt, um die PS den Gebäudegrenzflächen dieses Stadtmodells zuzuordnen. Das Ziel der durchgeführten Experimente ist vor allem die Erkennung von Effekten, die diese Zuordnung stören. Es zeigt sich, dass PS und Kartendaten an Fassaden weitestgehend übereinstimmen, während an Dächern stärkere Unterschiede auftreten. Das liegt größtenteils an Generalisierungseffekten, die an Dachstrukturen deutlich stärker ausgeprägt sind. Eine wesentliche Feststellung ist, dass sich einige PS innerhalb von Gebäuden befinden können. Die Ursachen, die zur Entstehung solcher PS führen, konnten nicht abschließend geklärt werden. Allerdings könnten diese PS wesentliche Probleme bei der Interpretation von Deformationsergebnissen verursachen.

Um eine Zuordnung der PS zu den Grenzflächen des Stadtmodells zu ermöglichen, wird ein Verfahren zur geometrischen Registrierung beider Datensätze entwickelt. Die Grundlage der Methode bildet ein Iterative Closest Plane Algorithmus, der auf die speziellen Charakteristika der PS-Punktwolke angepasst wird. Die Plausibilität der erhaltenen Ergebnisse wird in Fallbeispielen und anhand des Konvergenzverhaltens der iterativen Prozedur gezeigt.

Anzahl und Verteilung der PS hängen von der Szene ab und können der Überwachungsaufgabe nicht angepasst werden. Das stellt eines der größten Nachteile von PSI dar, da auftretende Boden-Bewegungen unter Umständen nicht erkannt werden. Um dieses Problem zu mildern wird eine Karte, die die PS-Dichte für jede Grenzfläche des dreidimensionalen Stadtmodells zeigt, aus der bereits bekannten Zuordnung zwischen PS und Gebäuden erzeugt, was zumindest die Erkennung unterabgetasteter Gebiete ermöglicht. Die Dichte-Karte wird zur Erkennung einiger Faktoren genutzt, die die PS-Dichte wesentlich beeinflussen. Letztere werden anhand von Fallbeispielen diskutiert.

Um die regelmäßige Anordnung der PS an Gebäudefassaden auszunutzen, wird ein Produktionssystem zur Erkennung regelmäßiger horizontaler Muster entwickelt. Die erhaltenen Ergebnisse sind heterogen. Manche Fassaden enthalten eine Vielzahl von Gruppen, während an anderen Fassaden kaum Muster erkannt werden. Das kann zu großen Teilen auf Layover-Effekte zurückgeführt werden, die Muster erheblich stören können. Die gewonnene Gruppierungsinformation kann zur Verbesserung der Höhenschätzung des kompletten Musters genutzt werden. Für die Bestimmung der vertikalen Position jeder Gruppe wird das gewichtete Mittel der Höhen der einzelnen PS diskutiert. Der erwartete Genauigkeitsgewinn wird theoretisch auf Basis des Cramer-Rao Lower Bound (CRLB) einer einzelnen Höhenschätzung durch Fehlerfortpflanzung bestimmt.

Schließlich werden die vertikalen Distanzen zwischen PS-Gruppen und horizontalen Strukturen in light detection and ranging (LIDAR) Daten ausgewertet. Ziel dieser Untersuchung ist die Zuordnung der PS zu real existierenden Strukturen, die durch die LIDAR Daten repräsentiert werden. Die Untersuchung beschränkt sich auf die Fassaden zweier Gebäude mit sehr einfachem Aufbau.

Contents

1. Introduction **17**
1.1. Motivation . . . 17
1.2. Structure of the thesis . . . 18
1.3. State-of-the-art . . . 19
1.3.1. Persistent Scatterer Interferometry . . . 19
1.3.2. Detection of regular patterns . . . 24
1.4. Objectives . . . 26

2. Basics **27**
2.1. Synthetic Aperture Radar . . . 27
2.1.1. Introduction . . . 27
2.1.2. SAR image resolution . . . 27
2.1.3. Single and multiple scatterers . . . 29
2.1.4. Foreshortening, Layover and RADAR shadow . . . 31
2.2. InSAR . . . 32
2.3. Persistent Scatterers . . . 36
2.3.1. Detection of PS . . . 38
2.3.2. Reference Network Estimation . . . 38
2.3.3. Final Estimation and Geocoding . . . 39
2.3.4. Precision of PS location . . . 39

3. Methods **43**
3.1. Grouping of PS at building facades . . . 43
3.1.1. Automatic detection of linear PS patterns . . . 43
3.1.2. Parameter Settings . . . 48
3.1.3. Accuracy of group height estimation . . . 50
3.1.4. Improvement of the group localization . . . 54
3.2. Alignment of Persistent Scatterers with 3D city model . . . 55
3.2.1. Correspondence Estimation . . . 55
3.2.2. Transformation Estimation . . . 57
3.3. Assignment of Persistent Scatterers to city model . . . 58

4. Experiments **61**
4.1. Test site and datasets . . . 61
4.1.1. Persistent Scatterers . . . 62
4.1.2. Reference data . . . 69
4.2. Grouping of PS at building facades . . . 71
4.2.1. Parameter Settings . . . 71
4.2.2. Results . . . 73
4.3. Alignment of PS to city model . . . 79
4.3.1. Parameter Settings . . . 79
4.3.2. Results . . . 80
4.4. Assignment of Persistent Scatterers to buildings . . . 81
4.4.1. Matching of Persistent Scatterers to building model faces . . . 81
4.4.2. Assignment to facade details . . . 88
4.4.3. Density Map . . . 92

5. Summary **99**
5.1. Findings . . . 99
5.2. Future Work . . . 102
5.3. Conclusion . . . 103

A. Appendix A **109**

B. Appendix B **113**

C. Appendix C **117**

D. Appendix D **123**

Nomenclature

Abbreviations

2-D two-dimensional

3-D three-dimensional

APS atmospheric phase screen

CRLB Cramer-Rao Lower Bound

DEM digital elevation model

DHHN Deutsches Haupthöhennetz

DTM digital terrain model

dInSAR differential SAR interferometry

DLR German Aerospace Center

GENESIS Generic System for Interferometric SAR

InSAR interferometric SAR

ICP iterative closest point

i.i.d. independent and identically distributed

KDE kernel density estimation

LAMBDA least-squares ambiguity decorrelation adjustment

LOD level of detail

LoS line of sight

LIDAR light detection and ranging

LSA least-squares adjustment

MRF markov random field

MSE mean squared error

OGC Open Geospatial Consortium

PDF probability density function

PRF pulse repetition frequency

PSI persistent scatterer interferometry

PS persistent scatterers

PSC persistent scatterer candidates

RADAR radio detection and ranging

RAR real aperture radar

RCS radar cross section

SCR signal to clutter ratio

SAR synthetic aperture RADAR

SBAS small baseline subset

SNR signal to noise ratio

StaMPS Stanford Method for PS

SVD singular value decomposition

TSVD truncated singular value decomposition

TomoSAR SAR tomography

TEC total electron content

TUM Technische Universität München

TOA time of arrival

UTM Universal Transverse Mercator Coordinate System

WGS84 World Geodetic System 84

List of symbols

General

c	speed of light
j	complex unit
$E[x]$	expectation value of x
$W\{\bullet\}$	wrapping operator

SAR system parameters

BW	bandwidth of the RADAR chirp signal
λ	wavelength of the RADAR system
τ	pulse length of the RADAR system
θ	look angle of the RADAR system
H	heading of the satellite
ρ_r	slant range resolution of a RADAR sensor
ρ_{gr}	ground range resolution of a RADAR sensor
ρ_a^{SAR}	azimuth resolution of a synthetic aperture RADAR
ρ_a^{RAR}	azimuth resolution of a real aperture RADAR
L_a	azimuth extent of the RADAR antenna
L_a^{syn}	length of the synthesized antenna

SAR

A_x	amplitude of the signal at image position x
ψ_x	phase of the signal at image position x
s_x	complex signal at image position x

InSAR

v_x	complex interferometric observable at image position x
ϕ_x	interferometric phase at image position x
$r_{M,x}$	distance of master sensor at image position x
$r_{S,x}$	distance of slave sensor at image position x
Δr_x	distance difference between master and slave at image position x
$\Delta\theta$	parallax relevant for height determination from the interferometric phase

$B_\perp$	perpendicular baseline between master and slave acquisition
δ_P/δ'_P	deformation of point P /deformation of point P in line of sight
$\Delta\phi_x$	flattened interferometric phase at image position x
h_P	height of point P above reference surface
s_P	elevation position of point P above reference surface
Γ_x	coherence at image position x
σ_ϕ	phase noise
$(\bullet)^w$	wrapped phase
$\Delta\phi^w_{x,y,i}$	phase difference between points x and y in the i-th interferogram
T_i	temporal baseline associated with the i-th interferogram
ν_x/ξ_x	seasonal motion parameters at image position x
$\Delta\nu_{x,y}/\Delta\xi_{x,y}$	difference of seasonal motion parameters between image positions x and y
$\Delta h_{x,y}$	height difference between image positions x and y
σ_B	standard deviation of $B_\perp$ within data stack
σ_s	standard deviation of PS elevation position
σ_r	standard deviation of PS range position
σ_a	standard deviation of PS azimuth position

Grouping of facade PS

α	angle between building outline and sub-satellite track
$\sigma_{\Delta\mathrm{X}'}$	standard deviation of X′-difference
$\sigma_{\Delta\mathrm{Y}'}$	standard deviation of Y′-difference
$\Delta\mathrm{X}'_{tol}$	tolerance for deviation from expected point spacing parallel to outline
$\Delta\mathrm{Y}'_{tol}$	tolerance for distance difference to outline along range
κ	scaling factor controlling the confidence level of $\Delta\mathrm{X}'_{tol}$ and $\Delta\mathrm{Y}'_{tol}$

Group height estimation

w_i	weight of i-th PS in group height estimation
N	number of PS in group
$\hat{\sigma}_{s,i}$	estimated standard deviation of the elevation position of the i-th PS in group height estimation

Alignment PS to city model/Assignment of PS to buildings

$\mathbf{F}$	set of all building faces contained in the city model
F_q	q-th building face
$\mathbf{n}_q/c_q$	unit normal vector/distance to origin of plane associated with F_q (Hessian normal form)
Q	number of faces contained in the city model
$\mathbf{P}$	set of all geocoded PS
$\mathbf{p}_i$	i-th PS of geocoded point cloud
M	number of PS in point cloud
$\mathbf{C}$	set of correspondences
K	number of correspondences
$d_{\mathbf{p}_i,F_q}$	distance between i-th PS and q-th building face
$\sigma_{d_{\mathbf{p}_i,F_q}}$	standard deviation of the distance between i-th PS and q-th building face
$\mathbf{\Delta}$	shift between PS and city model
$d_{k,\mathbf{\Delta}}$	distance associated with the k-th correspondence after application of shift $\mathbf{\Delta}$
w_k	weight of k-th correspondence in shift estimation
$\mathbf{x}_{s,k}$	unit vector in elevation direction for PS associated with the k-th correspondence
$\mathbf{x}_{r,k}$	unit vector in range direction for PS associated with the k-th correspondence
$\mathbf{x}_{a,k}$	unit vector in azimuth direction for PS associated with the k-th correspondence
$\mathbf{\Sigma}_{\mathbf{p}_k}$	covariance matrix of the position of the PS associated with the k-th correspondence
$\mathbf{\Sigma}_{\mathbf{p}_k,c_k}$	joint covariance matrix of the position of the PS and the parameter c_k of the plane associated with the k-th correspondence
σ_{c_k}	standard deviation of the plane parameter c_k associated with the k-th correspondence
J_k	Jacobian containing the partial derivatives of $d_{k,\mathbf{\Delta}}$ with respect to $\mathbf{p}_k$ and c_k
W_{ol}	width of the outline buffer
W_{pl}	width of the polygon buffer at every building face

Least Squares Adjustment

$\mathbf{A}$	design matrix in least-squares adjustment
$\mathbf{x}$	vector of parameters in least-squares adjustment
$\mathbf{b}$	vector of observations in least-squares adjustment
$\mathbf{p}$	weight matrix in least-squares adjustment

Comparison of PS groups with LIDAR

$\overline{\Delta}$	mean vertical distance between PS groups and LIDAR patterns
$\sigma_{\overline{\Delta}}$	standard deviation of mean vertical distance between PS groups and LIDAR patterns

1. Introduction

1.1. Motivation

The determination of topography and deformation of the Earth's surface is one of the key points in geodetic research. Traditionally, terrestrial methods, such as leveling, as well as optical imagery provided by planes or satellites are used for that purpose. Terrestrial methods usually give very accurate and reliable results at comparably high costs. Optical imagery is suited for the estimation of surface topography and large deformations. However, it is not accurate enough to measure small deformation signals (i.e. millimeters to centimeters). Furthermore, the acquisition of optical imagery is often hampered by cloud coverage and restricted to day time due to the passive sensor principle.

In order to monitor small deformation signals over long time spans, independent of weather and lighting conditions, the persistent scatterer interferometry (PSI) has become increasingly popular. PSI is a relatively new technique, which is based on radio detection and ranging (RADAR). It utilizes a stack of synthetic aperture RADAR (SAR) images in an interferometric processing framework. Deformation and topography are estimated on a sparse grid of strong and stable radar reflectors, referred to as persistent scatterers (PS). Those are characterized by a high signal to noise ratio (SNR) during the whole observation time and are usually situated on man-made objects. As a consequence, the technique is most often limited to urban areas.

In contrast to terrestrial techniques, where the number of measurements and their location is chosen by a human operator, the distribution of PS is governed by the scene and cannot be increased by the operator without allowing for estimates of potentially lower quality (i.e. by lowering the acceptance threshold). This is a principal drawback of the method as comprehensive coverage is very important for monitoring tasks.

The precision of the obtained parameter estimates is mainly a function of the number of acquisitions, the SNR of the observed PS, and the observation baselines, which characterize the degree of temporal or spatial separation of the images. As the last two depend on the acquisition and maneuvering schedule of the satellite and the scene respectively, they cannot be influenced substantially. Thus, increasing the number of acquisitions is the only way to effectively improve the achievable precision. This obviously increases the costs and requires more data to be available. Under favorable conditions and assuming a typical stack configuration, the accuracy of deformation estimates is in the order of a few millimeters, while the accuracy of the topography estimate ranges from some decimeters to one meter. The disbalance is due to the different sensitivity of the interferometers (i.e. all the interferometric pairs in the stack) to topography and deformation signal.

Typical point densities for medium resolution data (as provided by the ERS and ENVISAT satellites) are in the order of 100-500 PS per km^2. This is sufficient to reliably monitor deformation phenomena of at least some hundreds of meters extension. In case data of the new generation satellite systems TerraSAR-X or COSMO-Skymed are used, which provide very high resolution of one meter or even below, PS densities of up to 100,000 PS per km^2 are possible. This tremendous increase in point density enables the estimation of small scale deformation, such as the motion of single buildings.

Furthermore, as the resolution increases, the PS distribution shows an increasing amount of regular patterns which is especially true at building facades. Those are usually induced by regularly distributed building details such as windows, balconies, and chimneys. This patterns contain information that is useful for PS processing to constrain the parameters of interest. Practically, such information results in constraints imposed on the unknowns. Each constraint increases the redundancy of the problem and, thus, the precision of the estimated parameters.

Because of the limited positioning accuracy, an identification of the real world structure that induces the PS is very difficult. Besides the scientific relevance of this question, it constitutes a major problem for PSI applications. Without having an association of identified PS to actual structures in the real world, a check of the obtained PSI results with auxiliary measurements (such as leveling) is difficult. Furthermore, interpretation of deformation results can be problematic since urban deformation processes may exhibit a complex structure and are only understandable if the physical nature of the observed PS is known.

1.2. Structure of the thesis

This thesis is structured as follows. Firstly, the state-of-the-art in research fields that are relevant for this thesis is outlined followed the objectives of the presented work. Within chapter 2, fundamentals of SAR imaging, interferometric SAR (InSAR), and PSI are addressed. The newly developed methods for the assignment of PS to buildings and the detection of horizontal PS patterns are described in chapter 3. In particular, the detection of horizontal PS patterns, the alignment of PS and map data, and the assignment of PS to building faces are covered. The part dealing with the grouping approach includes an assessment of the precision gain achievable with the obtained additional information. In chapter 4 experimental results are presented. They comprises a validation of the outcome of the grouping approach, an assessment of the assignment procedure for two exemplary buildings, a comparison of light detection and ranging (LIDAR) data with horizontal PS patterns, and the derivation and discussion of the PS density map, derived from the affiliation of PS to building faces. In chapter 5 the results are summarized and conclusions are drawn. Finally, directions for future work are proposed.

1.3. State-of-the-art

This thesis covers topics, which can be mainly attributed to two communities. On the one hand, the study of PSI is mainly addressed by the remote sensing community. Research on the detection of regular patterns in image data, on the other hand, has rather been conducted in the computer vision and pattern recognition community. However, many of the developed methods have been adapted and applied to remote sensing data. In the following the main ideas leading to the topics covered within this work are presented and the corresponding publications are addressed.

1.3.1. Persistent Scatterer Interferometry

In this section the developments in PSI that are of interest for this thesis are summarized. It is divided into five parts. The first part deals with the signal processing methods used to estimate deformation and topography from a given stack of interferograms. Subsequently, PSI using high resolution data is addressed. In the third part publications on the introduction of additional knowledge into the PS processing framework are discussed. Recent work on the assignment of PS to real world structures is presented in the fourth part. Finally, research on the assessment of the PS density is addressed.

Signal processing

The basic idea of exploiting a subset of sufficiently coherent pixels in a multi-interferogram framework dates back to the pioneering work presented in Ferretti et al. [2000, 2001]. In order to identify PS and to separate topographic and deformation signal from nuisance terms, like atmospheric phase screen (APS), a spatio-temporal analysis of the interferometric phase is conducted. Deformation and topography are represented by a parametric model, which is inverted by means of a periodogram estimator adapted for irregularly spaced data ([Ferretti et al., 2000]. The original method for regularly spaced data has been presented in Rife & Boorstyn [1974]). Theoretical and experimental validations have proven the method to be able to estimate deformation with millimeter precision [Colesanti et al., 2003a,b].

In Kampes [2006] an alternative method for PS processing, that replaces the periodogram estimator with the least-squares ambiguity decorrelation adjustment (LAMBDA), is proposed. Within the LAMBDA estimator observations are modeled as Gaussian random variables known up to integer multiples of 2π. Consequently, a covariance matrix of the measurements can be introduced into the estimation process and a fully populated covariance matrix of the estimated parameters is available after processing. The natural handling of imprecise and correlated observations is one of the major advantages of the LAMBDA method compared to the periodogram estimator.

It is worth mentioning, that PSI can be seen as a special case of SAR tomography (TomoSAR) [Bamler et al., 2009]. In PSI the presence of only one dominant scatterer per resolution cell is

assumed. The result is an estimate of this target's height and deformation. It can be, consequently, regarded as a parametric method. In case the assumption of a single scatterer is not fulfilled, the resolution cell is most likely rejected since it contradicts the assumed model. Opposed to that, TomoSAR aims at reconstructing the reflectivity distribution of a resolution cell along the elevation direction (i.e. perpendicular to the range-azimuth plane, see section 2.1). The whole problem comes down to the estimation of a signal from its irregularly sampled fourier transform. Inversion strategies are presented in Reigber & Moreira [2000], Fornaro et al. [2003], Zhu & Bamler [2010], and Zhu & Bamler [2011b]. An extension to four dimensional imaging (i.e. reconstruction of the reflectivity in the elevation-velocity domain) has been considered in Lombardini [2003], and Fornaro et al. [2009]. Finally, seasonal motion is addressed in Zhu & Bamler [2011a], who reveal deformation due to thermal expansion.

High resolution PSI

A major step forward for the whole SAR community was the advent of the high resolution satellite systems TerraSAR-X and COSMO-SkyMed. First PS results obtained with TerraSAR-X high resolution spotlight data are presented in Bamler et al. [2009]. The main finding is the massive increase in PS density. In contrast to medium resolution data, plenty of PS can be found on a typical building. According to model calculations, a trihedral structure has to exhibit a side length of 30 cm to induce a PS in medium resolution data. This side length is reduced to 8 cm if data of the highest resolution is used (e.g. TerraSAR-X high resolution spotlight) [Bamler et al., 2009]. Since typical elements of buildings are recognizable in the data, the interpretation of the physical nature of the PS is also massively supported.

Additional Knowledge in PSI

In all PS processing schemes, assumptions about the spatio-temporal characteristics of the respective phase contributions are made. Those assumptions are necessary to discriminate the signal of interest from nuisance terms. Usually, the utilized models are simple and generic. Deformation, for instance, is often assumed to be a linear or periodic function of time plus a non-parametric, time-dependent term accounting for deviations from this model (cf. [Ferretti et al., 2000; Colesanti et al., 2003a; Gernhardt, 2012]).

In Ferretti et al. [1999] the derivation of an optimum filter for the estimation of non-linear target displacement from unwrapped phase data is discussed. It is stressed that this requires knowledge of the underlying physical process that induces the deformation. For example, a filter expression for deformation consistent with a diffusion process is derived.

Hooper [2006] models the source of deformation present in the caldera of Volcan Alcedo (Galapagos) as a contracting, finite ellipsoid. The model is fitted to displacement rates obtained from an ascending and a descending data stack by means of Markov Chain Monte Carlo sampling. In

contrast to Ferretti et al. [1999], where the goal is the retrieval of optimal parameter values, the focus here is on the physical interpretation of the results.

In Ketelaar [2010] a subsidence prognosis (e.g. based on a deformation model) is used to calculate a variogram of the expected deformation process. This is in turn used to reject PS that are not consistent with the model. Among others a case study dealing with subsidence of the Rotterdam gas field is presented. The main aim is to distinguish different deformation regimes (i.e. discrimination of subsidence due to gas extraction from e.g. natural soil compaction).

A radargrammetric approach for the positioning of point scatterers[1] based on Bayesian inference is presented in Goel & Adam [2012]. Those point scatterers which are situated close to each other in the same range line (i.e. sharing the same azimuth coordinate) are assumed to be located on a vertical or a horizontal plane. This results in a model linking the height of point scatterers along range direction.

Although the work presented in Shabou et al. [2012] does not deal with PS, the considered method is, due to its generality, of interest in this discussion. Furthermore, the employed data and the application are very similar. The goal is to reconstruct scene topography from multibaseline InSAR data, which is done by energy minimization. The associated cost function consists of two terms. The first accounts for the fit of the model to the data, while the second imposes a local smoothness constraint on the solution. This formulation constitutes a markov random field (MRF). For the purpose of inference in MRFs powerful solvers are available.

Gernhardt & Hinz [2008] deal with PS results obtained from high resolution data (i.e. many PS per building are available). The key idea is to identify groups of PS that are situated on the same building and to jointly model their deformation. Specifically, the model is chosen to correspond to a non-destructive deformation.

Finally, in Gernhardt [2012] regular horizontal patterns of PS are exploited to estimate the point localization precision. The patterns are manually selected and introduced into a least-squares adjustment (LSA) which models the PS to be situated on a horizontal line at constant distances.

The approaches presented in Ferretti et al. [1999], Hooper [2006], and Ketelaar [2010] are very similar in that knowledge about the underlying physical process is used to define a refined model for the deformation. Those models are tailored to describe the spatial behavior of the deformation over hundreds of meters to kilometer scales, which matches the resolution of the data involved in the conducted case studies. Thus, the expected movement for close PS is very similar (i.e. the model involves some kind of spatial smoothness). Furthermore, it does not take the affiliation of PS to scene structures into account. For instance, PS on the ground and at building facades are treated the same way. Similarly, Shabou et al. [2012] and Goel & Adam [2012] use quite general spatial models for the parameters. Higher level knowledge about the investigated scene, like all pixels showing a facade should result in a vertical planar structure, is not involved.

[1] Note that PS and point scatterers are not necessarily equivalent, as the point scatterers are not required to exhibit phase stability.

In contrast to this, higher level knowledge is used in Gernhardt & Hinz [2008] and Gernhardt [2012]. Both approaches are tailored to high resolution data which provide enough detail to deduce the additional information. While regular horizontal patterns of PS are manually selected in Gernhardt [2012], Gernhardt & Hinz [2008] propose some strategies to infer the required knowledge but do not present real data examples. Altogether, the focus in both approaches is on the utilization rather than on the deduction of the additional information.

Assignment of PS to real world structures

An issue of major interest for PSI is the assignment of PS to real world structures. Technically, the problem consists in the identification and localization of all reflections contributing to the PS. Besides scientific interest, the question is of practical importance since the measured deformation may be a superposition of the motions of all structures hit on the respective signal path. Thus, in order to interpret the obtained results, information about the involved real world objects is very important. The work that has been done on this topic can be roughly divided into two kinds of approaches. The first is data driven and relies on the estimation of parameters characterizing each target. The second approach is model driven and aims at reconstructing the complete signal path with ray tracing simulations.

In Perissin & Ferretti [2007] a data driven approach is presented. In order to determine the nature of scattering mechanisms, parameters describing the target characteristics are estimated. Those are, for instance, the radar cross section (RCS), the target extension[2], and the height of the scatterer's phase center. Finally, a comparison with theoretical values of canonical scattering mechanisms enables a classification into one of the following categories: Roof (monohedral), Grating (resonating monohedral), Dihedral, resonating Dihedral, Pole, and Trihedral. An investigation using a mixed stack of ERS1/ERS2 and ENVISAT acquisitions including images of different polarization (i.e. HH and VV images) of Milan (Italy) is presented. Interestingly, most of the PS are affiliated to monohedral roof scattering (50%), while only 8% are attributed to trihedral scattering mechanisms.

Gernhardt [2012] deals with the affiliation of PS obtained from high resolution SAR data to the ground, facades, and roofs. Thereby, only the geopositions of the PS are used. First of all, a filter separating facade from non-facade PS is applied. Subsequently, the height histogram of the non-facade PS is inspected in order to separate targets on the ground and on roofs. In the conducted case study PS obtained from two high resolution spotlight data stacks of Berlin (Germany) are examined. The result suggests the following distribution: 50% at facades, 25% at low heights and on the ground, and 25% on roofs.

In contrast to that, Auer [2011] uses highly detailed building models together with ray tracing simulations to facilitate the interpretation of urban reflection scenarios. The focus lies on the understanding of high resolution spaceborne SAR data. In order to investigate reflection mechanisms

[2]To be more precise, the extension of an equivalent, uniformly scattering, and tilted plane in cross-slant range and azimuth direction is estimated.

inducing RADAR targets with temporally stable backscattering characteristics, PS identified in real data are manually compared to bright point-like signatures present in the simulated SAR images. For each signature the number and location of bounces is determined within the simulation. Thus, a complete characterization of the scatterers under investigation is provided. The results suggest that a significant number of PS are induced by triple- or even fivefold reflections. Furthermore, trihedral reflectors inducing PS are often formed by building details, such as window sills. In some cases the trihedral reflection is induced by separated building parts forming a section of a trihedral corner reflector. The phase centers of those PS do not physically exist leading to targets which seem to be distributed randomly. The fivefold bounces often involve three reflections at the building and two additional reflections at the ground surface. That gives rise to so called Ghost-PS which are apparently located underneath the ground level (cf. Auer et al. [2011a]).

Although the approaches presented in Gernhardt [2012] and Perissin & Ferretti [2007], respectively, are both data driven, the basic idea and the results are quite different. While Perissin & Ferretti [2007] use a variety of data to enable an estimation of the scattering characteristics per point, Gernhardt [2012] considers the local spatial distribution of the PS to discriminate facade and non-facade PS. The former approach assigns each point to one of the defined canonical scattering mechanisms. The latter method is not concerned with the single PS, but gives some insight into the spatial distribution of PS in an urban environment. It is worth to note that the distinction of ground and roof PS in Gernhardt [2012] is facilitated by the horizontal ground surface of the test site. In case of undulated terrain, the height histogram of non-facade PS would, certainly, become flatter, which would hamper the discrimination of ground and roof points. Although the approach of Perissin & Ferretti [2007] reveals the type of reflection, the location of the respective bounces remains unknown. Consequently, neither Perissin & Ferretti [2007] nor Gernhardt [2012] establish a connection between single PS and specific urban objects. On the contrary the simulation used in Auer [2011] results in a complete description of the signal path. However, since highly detailed building models are needed, the approach is limited to few case studies.

Assessment of PS density

One of the major problems of PSI is the opportunistic sampling of the monitored environment. Classical geodetic techniques refer to benchmarks, which are mounted at locations selected prior to the monitoring. Opposed to that, the position of PS cannot be chosen by the operator. As deformation may not be detected due to missing point coverage, it is important to assess the PS density. So far, just few work has been conducted on this topic.

In Gernhardt [2012] the influence of acquisition parameters on the PS density is investigated. For that purpose, the number of points per unit area is determined for different test sites and several data stacks. In order to derive the density, a sliding window with a certain width is used. An affiliation of PS to real world objects is not taken into account.

The approach has two main disadvantages. Firstly, setting the size of the sliding window is often critical. If the window is too large, the result is over-smoothed. In case the window is too small, the density estimate is inaccurate. Secondly, the point density per building or building part cannot be inferred because no information about the scene objects is available. From a practical point of view, the density per building part is the important piece of information since it determines if the structure can be properly monitored.

1.3.2. Detection of regular patterns

For this work pattern recognition techniques aiming at the detection of geometric regularities in two-dimensional iconic and symbolic data are of interest. Many of such methods are used in remote sensing to find and reconstruct man-made structures. In computer vision applications a lot of related work has been done on texture analysis.

A production system aiming at the detection and reconstruction of buildings in high resolution SAR data is presented in Michaelsen et al. [2006]. It essentially encodes principles of human perceptual grouping to assemble complex objects from simpler ones. Those comprise concepts such as proximity, good continuation, similarity, and symmetry, which originally emerged in perceptual psychology but proved to be helpful also in computer vision applications [Desolneux et al., 2004]. The whole framework is referred to as Gestalt theory [Wertheimer, 1923]. Technically, those laws constitute the knowledge base, which is represented by a set of production rules. The order in which possible productions are applied to primitives or already assembled objects is determined by a control unit based on a set of assessment rules. More information on the control, including strategies for fast and approximate image interpretation, can be found in Michaelsen et al. [2009]. As Michaelsen et al. [2006] use no prior knowledge about building location and orientation (e.g. available map data), the number of possible productions is large. Thus, the computational complexity of the method is very high. An alternative approach can be found in Michaelsen et al. [2002], where building locations and orientations are inferred from InSAR data. A digital elevation model (DEM) is produced from the filtered interferometric phase and searched for elevated regions, which serve as building cues. Building outlines are subsequently obtained by approximating those cues by polygons. Finally, the resulting outlines are used to guide the grouping of salient spots to rows. This approach is a practical way to infer prior information about the building location and orientation in case layover induced problems can be neglected. If the buildings exhibit a complicated setup or several buildings are close to each other, which is often the case in densely built-up areas, the extraction of building cues (i.e. the elevated regions) may fail.

The detection of lattices is a major issue in the field of texture analysis, which has led to many sophisticated methods. In case a texture is assembled of periodically appearing texture elements (i.e. it is not random), one is interested in inferring their position as well as the global topology. All of that is provided by the underlying lattice. A method based on finding peaks in the autocorrelation function of the image is proposed in Liu et al. [2004]. In Hays et al. [2006] the problem is reformulated

as a correspondence problem. This is advantageous as powerful solvers exist for this sort of task. Recently, Park et al. [2009] proposed the use of a MRF to model periodicity of appearance and similarity of texture elements. In this way radiometric and geometric constraints between several texture elements are dealt with simultaneously, leading to a more robust result. Certainly, the formulation in a stochastic framework additionally enables the natural handling of uncertainty. The problem of texture analysis is different from the one presented in Michaelsen et al. [2006] because the primitive objects are extended image patches and not points. Since the centers of those texture elements are not known in advance, they have to be determined during processing. This complicates the problem. On the other hand, for extended image patches more information is available than for points (e.g. mean and standard deviation of grey values), which facilitates the lattice detection.

Summary

The advent of high resolution spaceborne SAR data has triggered new research directions in PSI. Due to the high level of detail, constructive elements of buildings are visible in the image data. This finding shifted the focus from the assessment of medium to large scale deformation processes to the monitoring of single buildings, which certainly requires automated methods to assign PS to building structures. However, just few work has been done on this issue so far. Gernhardt & Hinz [2008] propose some strategies, but do not provide case studies. In Gernhardt [2012] the movement of the main train station in Berlin (Germany) is assessed and analyzed in detail. However, the affiliation of the PS to the building is done manually.

It is important to stress that monitoring of single buildings using high resolution PSI is only possible if the objects under investigation are properly sampled. As PSI is characterized by an opportunistic sampling (i.e. the points cannot be chosen by the operator), sufficient coverage is not guaranteed for all buildings. Thus, an assessment of the PS density is very important for practical applications. In Gernhardt [2012] the influence of the acquisition parameters on the PS density is investigated. However, no connection to building structures is established.

As constructive elements of the buildings are observable in the SAR data, refined models of the building motion are conceivable. Those models couple the deformation of PS that are situated on the same building or building part. Since this leads to additional constraints or equivalently to less parameters, the precision of the motion estimates is increased. An approach addressing non destructive deformation is outlined in Gernhardt & Hinz [2008]. However, only results using simulated data are presented.

Similar to the deformation, the topography estimate can be improved by introducing additional constraints. For that purpose, regular patterns of PS at building facades, which are often encountered in high resolution SAR data, can be exploited. In Gernhardt [2012] the position of PS arranged in horizontal rows at constant distances is enhanced using a LSA. The patterns are, however, manually selected, hampering the operational applicability of the method.

Pattern recognition techniques aiming at the detection of geometric regularities in image data could be used to automate the identification of such regularly arranged PS. As the task then becomes the detection of regularities in a two dimensional point set, approaches focusing on symbolic data (opposed to iconic or image data), similar to Michaelsen et al. [2006], seem to be suited.

1.4. Objectives

This thesis focuses on the relation of PS to buildings in an urban environment. The PS are a set of RADAR point targets that show temporally stable reflection properties. For the investigations two distinct sets of PS are available which are both obtained from TerraSAR-X high resolution spotlight data. The buildings are represented by a level of detail (LOD) 2 city model. Each building is described by its bounding surfaces. Oblique view aerial images are used to obtain information about the setup of particular facades or roofs. Finally, LIDAR data is utilized as a geometric reference for both the city model and the PS set.

In order to fully exploit the potential of high resolution PSI results, an affiliation of PS to the monitored objects is of major importance to allow for advanced modeling and interpretation of the deformation of single buildings. Therefore, the focus of this work is the assignment of PS to building structures. This includes the development of an automatic method that relates the PS to auxiliary map data. Since this is the first attempt to systematically investigate the affiliation of PS to buildings using map data, the experiments are mostly concerned with an assessment of the comparability of both data sets. Special emphasis is on the identification of effects hampering the assignment procedure.

One of the main drawbacks of PSI is the inherent opportunistic sampling of the scene. For a practical application, the documentation of the PS density with regard to the structures under investigation is very important. Furthermore, the factors influencing the PS density are far from being understood. This work aims at tackling both issues using the established relations between PS and buildings. The latter are used to produce a density map (i.e. a map stating the number of PS per unit area for every bounding surface).

Regular patterns of PS contain information that is useful to better constrain the parameters of interest. In this thesis a strategy to improve the height estimate of PS is presented. This involves the development of a method for the detection of horizontal PS patterns and the proposition of an estimator exploiting the obtained knowledge. Besides an evaluation of the algorithms performance, the experimental evaluation focuses on investigating the conditions that are required for the emergence of such regular patterns.

The affiliation of PS to real world structures is very important for the interpretation of the deformation results. This is especially true in complex scenarios, such as dense build up areas. In this work the feasibility of such assignment is investigated exemplarily using oblique view aerial images and a LIDAR point cloud as auxiliary data.

2. Basics

2.1. Synthetic Aperture Radar

2.1.1. Introduction

This section gives a brief summary of the geometric and radiometric properties of SAR images. For more information about the process of SAR image formation, the reader is referred to Cumming & Wong [2005] and Bamler & Schättler [1993]. A comprehensive treatment of SAR imaging properties as well as geocoding of SAR acquisitions can be found in Raggam et al. [1993], Meier et al. [1993], and Soergel [2003]. Contrary to optical sensors, RADAR sensors are active devices. They emit radio waves which are reflected by objects in the scene. The echos are in turn received and recorded by the sensor. Since no external radiation source is needed, RADAR sensors can acquire data independent of lighting conditions. Typically RADAR operates with signal wavelengths ranging from some millimeters to some decimeters. Since the signal attenuation caused by scattering at atmospheric water vapor or even rain for wavelengths longer than approximately one centimeter is practically negligible, most RADAR systems are capable of acquiring data regardless of weather conditions. The independence of lighting and weather renders RADAR especially useful for rapid mapping scenarios after the occurrence of natural disasters as well as for military applications.

2.1.2. SAR image resolution

The SAR imaging geometry is sketched in figure 2.1. While moving on its trajectory, the sensor repeatedly emits pulses of length τ and records the echos of each pulse. The direction in which the pulses are sent is called slant range or across track, while the direction along the sensor's trajectory is referred to as azimuth or along track. Those two axes form the imaging grid of the SAR acquisition. The direction perpendicular to the range-azimuth plane is termed elevation. Targets along elevation cannot be distinguished using a single SAR image. The part of the Earth's surface which is illuminated by one transmitted pulse is called the antenna footprint. In slant range direction a distance measurement based on the time of arrival (TOA) principle is performed to map the scene. Objects in slant range can be discriminated if their echos do not overlap. Consequently, the SAR slant range resolution ρ_r as a function of the pulse length τ and the speed of light c is given by:

$$\rho_r = \frac{c\tau}{2}. \tag{2.1}$$

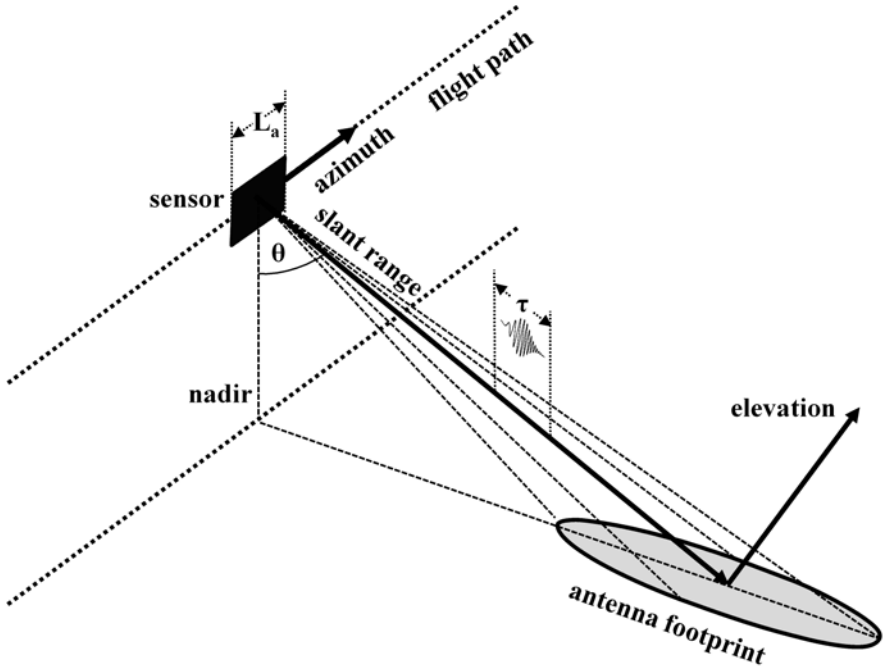

Figure 2.1.: Illustration of SAR imaging geometry

The ground range resolution additionally depends on the look angle θ of the RADAR system:

$$\rho_{gr} = \frac{c\tau}{2\sin\theta}. \tag{2.2}$$

In azimuth direction the scene is mapped by the movement of the antenna footprint. The resolution is determined by the width of the footprint, which depends on the target distance and the angular spread of the radar beam. The latter is determined by diffraction effects at the antenna and is proportional to the wavelength λ of the RADAR and inversely proportional to the length of the antenna in azimuth direction L_a. Two objects on the ground sharing the same slant range coordinate r can be discriminated if they are not both within the RADAR beam at the same time. Consequently, the azimuth resolution ρ_a^{RAR} is given by

$$\rho_a^{RAR} \approx \frac{\lambda \cdot r}{L_a}\,. \tag{2.3}$$

This simple configuration is called a real aperture radar (RAR). For common spaceborne systems the resulting azimuth resolution would be in the order of some kilometers and would depend on the target distance. Especially the poor azimuth resolution renders RAR sensors useless for most remote sensing applications. In order to improve the azimuth resolution and to eliminate the range dependency, a synthetic aperture is generated by combining many overlapping RAR acquisitions. The resulting imaging RADAR system is called synthetic aperture RADAR (SAR). While the sensor proceeds on its trajectory, a point target is illuminated several times. The distance between target and sensor varies between consecutive illuminations leading to differences in the signal runtime and,

consequently, to phase differences of the echos. Since the echos are received and recorded coherently, the phase history of a point target can be tracked along the flight path [Bamler & Schättler, 1993]. In order to locate the point target in azimuth, the fact that the phase history is a function of the targets azimuth position is exploited. Technically, the range variation between sensor and point target along azimuth, referred to as range cell migration, has to be considered. For simplicity this effect is ignored for the following illustration. The synthetic aperture is generated by correcting the echos of every point target for the distance variation and coherently summing them up. The resulting image turns out to be equivalent to a RAR image acquired with an antenna featuring a large azimuth extent. In case the slant range direction is perpendicular to the flight path during data acquisition, the length of the synthetic aperture is $L_a^{syn} = \frac{\lambda}{L_a} \cdot r$. The azimuth resolution of the SAR system is the product of the opening angle of the synthetic aperture, being approximately $\frac{\lambda}{2L_a^{syn}}$, and the target distance

$$\rho_a^{SAR} \approx \frac{\lambda \cdot r}{2 \cdot \frac{\lambda}{L_a} \cdot r} = \frac{L_a}{2} \ . \tag{2.4}$$

The SAR azimuth resolution only depends on the extent of the actual antenna in azimuth direction, which is in the order of some meters for typical spaceborn sensors. The acquisition mode with the slant range direction perpendicular to the flight path and the antenna beam maintained within a contiguous swath on the ground is called a stripmap SAR. Virtually all spaceborne SAR systems operate by default in stripmap mode since it enables the mapping of large areas at relatively high resolution. Current high resolution SAR satellite missions, like TerraSAR-X, can be operated in a so called spotlight mode, too. Thereby, the beam of the sensor is steered towards a certain area, which enables longer illumination time leading to better azimuth resolution at the cost of a smaller scene extent. More information about possible acquisition modes of TerraSAR-X can be found in Breit et al. [2010].

The resulting image is complex valued. Thus, for every pixel amplitude and phase information is available. The amplitude is a measure of the amount of radiation that is scattered back or reflected from the observed ground patch and is, as mentioned earlier, hardly attenuated by atmosphere. The phase is a function of the distance to the observed ground patch and is strongly influenced by the water vapor distribution along the signal path.

2.1.3. Single and multiple scatterers

The complex valued signal of a resolution cell at location x is modeled to be the coherent sum of N mutually independent reflections occurring within the observed ground patch:

$$s_x = A_x \cdot exp(j \cdot \psi_x) = \sum_{i=1}^{N} A_{x,i} \cdot exp(j \cdot \psi_{x,i}) \ , \tag{2.5}$$

where A_x is the amplitude of the sum signal, $A_{x,i}$ the amplitude of the i-th target, ψ_x the phase of the sum signal, $\psi_{x,i}$ the phase of the i-th target. Finally, j denotes the imaginary unit. This

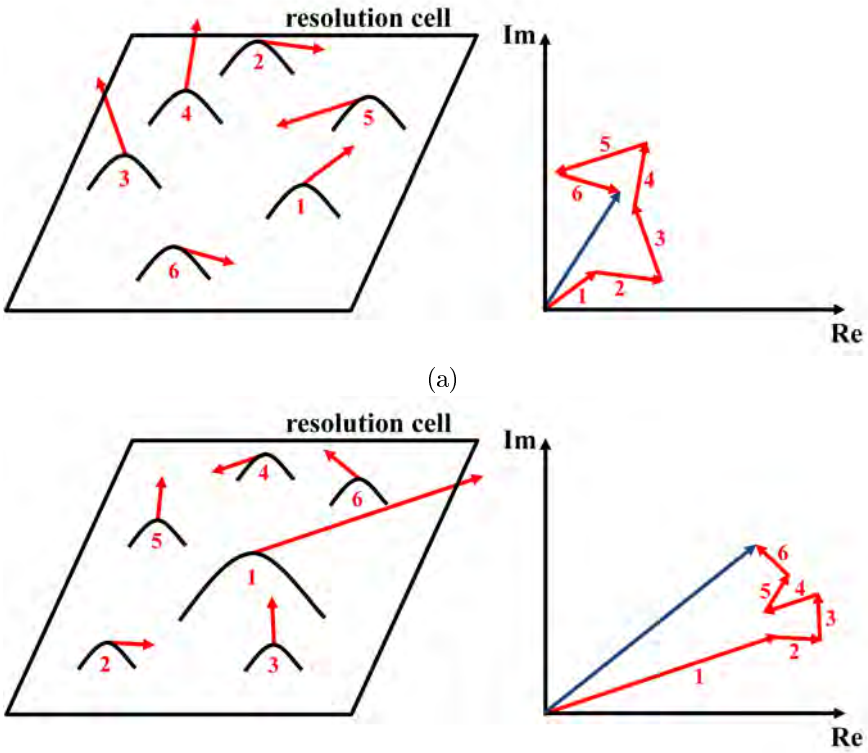

(a)

(b)

Figure 2.2.: Left: Sketch of targets within one resolution cell that contribute to the measured signal. The arrows indicate the strength and the phase of each contribution by their length and direction, respectively. Right: Coherent summation of the signal contributions in the complex plane. While each targets contribution is approximately equal in situation (a), one target is much stronger than all others in situation (b).

is sketched schematically for two different situations in figure 2.2. In the left column the targets contributing to the sum signal are shown. The size of the targets and the length of the arrows indicate the strength of the single reflections, while the direction of the arrows corresponds to the phase. On the right, the summation of the measured signal in the complex plane is shown. The sum signal is depicted as blue arrow, whereas the contribution of each target is shown in red. In situation (a) all targets are almost equally strong. One of the key observations is the strong dependence of the measured signal amplitude on the phase distribution of the involved scatterers. If all targets exhibit the same phase, constructive interference occurs and the final signal shows a very high amplitude. Opposed to that, destructive interference may happen, which results in zero amplitude. The phase of each scatterer depends on its position in the resolution cell (i.e. on the distance to the sensor) and on its physical properties. Especially for natural surfaces, the spatial distribution of scatterers can vary strongly from resolution cell to resolution cell even in areas of homogeneous land cover. Thus, this distribution is often modeled as a random process (cf. [Bamler & Hartl, 1998] for details on distributed scattering). The resulting amplitude fluctuation, causing the grainy appearance of SAR images, is called speckle effect. Even though speckle is not noise, it is often considered as a disturbance and modeled as multiplicative noise (i.e. the Speckle effect is stronger,

the stronger the average signal is). Typically, situations similar to (a) are found in vegetated areas. In contrast to that, the resolution element in (b) is dominated by one scatterer. As a result, the sum signal's amplitude and phase mainly depend on the amplitude and phase of this dominant signal contribution. Such situations are often but not exclusively observed in urban areas. While case (a) is an example of distributed scattering, the setting in (b) can be better modeled as point scattering, approaching the ideal case as the signal strength of the small reflectors tend to zero. The number of signal contributions, certainly, depends on the size of the resolution cell. For high resolution data (resolution in the order of one meter) less scatterers contribute to the measured signal, leading to a notable reduction of speckle in comparison to medium resolution data (resolution in the order of ten meter).

The notion of point-like targets, although useful to explain the radiometry of SAR images, constitutes a major simplification of the actual reflection mechanisms. In reality a target may be spatially extended and the corresponding signal contribution may itself be an aggregation of several reflections occurring at the target. Typical examples in urban areas are double bounce lines and trihedral corner reflectors. Both mechanisms are analyzed on a theoretical basis together with single bounce reflections in Dong et al. [1997]. As all signal paths share the same length, the resulting echo appears to originate from a line or a point, respectively. In Auer [2011] simulation studies using ray tracing techniques and highly detailed models of urban structures have shown that prominent point-like reflections are mainly induced by triple bounce reflections at trihedrals or even fivefold bounces, often including two additional reflections on the ground.

2.1.4. Foreshortening, Layover and RADAR shadow

In case the trajectory of the sensor is a straight line, the SAR imaging geometry results in a projection of the 3D space into a two-dimensional cylinder coordinate system. The coordinate axes are given by the azimuth (i.e. the sensors trajectory) and the range direction, respectively. Due to the projection of the real world into a two dimensional coordinate system, information about the three dimensional distribution of the scatterers is lost. Since the scene is mapped in azimuth direction without distortions, the discussion of the geometrical effects in SAR images will be restricted to planes perpendicular to the trajectory of the sensor (i.e. planes of constant azimuth). The three geometric effects present in SAR data, foreshortening, layover, and shadow, are shown in figure 2.3. The sensor illuminates the scene with a looking angle of θ[1]. Foreshortening occurs if the surface is tilted towards the sensor by an angle smaller than θ with respect to the horizontal plane. This is the case for the slope between the points A and B, slanted by an angle β_1. The corresponding points A' and B' are mapped closer together than their real world counterparts. A plane tilted by an angle larger than θ gives rise to layover, which is the case between points C and D ($\beta_2 > \theta$). Although the point C is located in front of D in the real world, C is further away from the sensor and, thus, mapped to a point C' located behind the point D' in the slant range geometry. Finally,

[1] For simplicity the wavefronts are assumed to be planar, which is justified by the large target distance.

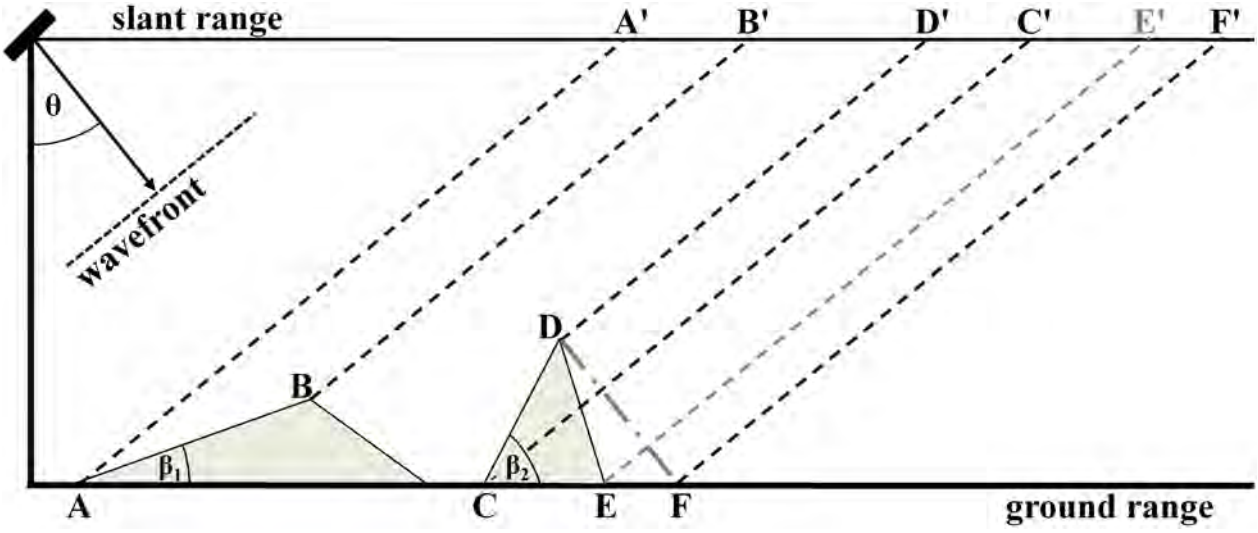

Figure 2.3.: Illustration of the three geometrical effects present in SAR images. Foreshortening appears between the points A and B, while Layover arises between the point C and D. Finally, no information is acquired between the points D and F due to shadowing.

the side looking geometry of SAR results in shadowing behind elevated objects. Between the points D and F no signal is measured since the corresponding area in the real world is occluded by the slope between points C and D. Thus, the point E is not mapped to the SAR image.

2.2. InSAR

In general, InSAR[2] refers to techniques exploiting the phase difference of two or more SAR images acquired with slightly different acquisition parameters [Bamler & Hartl, 1998]. Within this work the term InSAR is used to refer to across-track SAR interferometry, which is capable of measuring surface topography and deformation. Furthermore, only repeat-pass monostatic systems are discussed, implying temporally and spatially separated acquisitions. Typically, the time difference between two images is in the order of weeks or months and is called temporal baseline. The spatial separation between acquisitions ranges from some tens to some hundreds of meters and is referred to as spatial baseline. For the sake of simplicity, the case involving two images is discussed here. One of the images is called the master M, while the other is referred to as the slave S. For standard InSAR the choice of master and slave is arbitrary. After proper pre-processing we assume the slave image to be geometrically aligned with the master image (i.e. image position x in both images refer to the same patch of the earth's surface). More information about the pre-processing can be found in Hanssen [2001], Massonnet & Feigl [1998], DORIS User Manual [1998], and Wilkinson [1997]. For meter resolution SAR data, which is of specific interest for this thesis, special treatment may be necessary depending on the spatial separation of the the acquisitions [Eineder et al., 2008] (i.e. the use of an a-priori DEM is very beneficial).

[2]In the USA the abbreviation IfSAR is often used instead.

After resampling of the slave image to the master grid, an interferogram is formed by multiplying the master image $s_{x,M}$ with the complex conjugate of the slave image $s^*_{x,S}$ on a pixel by pixel basis leading to

$$v_x = s_{x,M} \cdot s^*_{x,S} = A_{x,M} \cdot A_{x,S} \exp(j \cdot (\psi_{x,M} - \psi_{x,S})) = \bar{A}_x \exp(j \cdot \phi_x) \; . \tag{2.6}$$

Neglecting all disturbances, the interferometric phase ϕ_x is a very precise measure of the distance difference between master and slave acquisition

$$\phi_x = -\frac{4\pi(r_{M,x} - r_{S,x})}{\lambda} = -\frac{4\pi\Delta r_x}{\lambda} \; . \tag{2.7}$$

For simplicity the fact that the measured phase is actually the 2π-modulus of ϕ is ignored for the remainder of this section. The process of estimating the unknown number of complete phase cycles is called phase unwrapping. More information about problem formulation and solutions can be found in Goldstein et al. [1988], Ghiglia & Romero [1996], Chen & Zebker [2000], Chen [2001] and references therein.

If the images are taken at distinct times and from slightly different positions with respect to the observed scene, the interferometric phase is a sum of three contributions.

$$\phi_x = -\frac{4\pi\Delta r_x}{\lambda} = \phi_{geom,x} + \phi_{topo,x} + \phi_{defo,x} \tag{2.8}$$

The geometric phase term ϕ_{geom} is caused by the oblique viewing geometry and can be thought of as the phase generated by an ideally flat earth at a given reference height [Bamler & Hartl, 1998]. Topography and deformation give rise to the phase contributions ϕ_{topo} and ϕ_{defo}, respectively. Since ϕ_{geom} is of no interest, it is removed.

$$\Delta\phi_x = \phi_x - \phi_{geom,x} = \phi_{topo,x} + \phi_{defo,x} \tag{2.9}$$

The basic principle of an across track interferometer is sketched in figure 2.4 for a plane perpendicular to the trajectory of the sensor. It observes the point P on the earths surface, which is located at height h_P above the reference surface and moving by δ_p between both acquisitions[3].

The spatial separation of the sensor at the two epochs of data acquisition leads to the topographic phase term ϕ_{topo}. The geometrical setup is depicted in figure 2.4 window **win1**. Both antennas are separated by a baseline B. The projection of the baseline onto the slant range is called the perpendicular baseline $B_\perp$ and directly determines the sensitivity of the interferometer to the topographic signal. In order to estimate the height of a point P above a reference surface, the parallax $\Delta\theta$ between P and a point on the reference surface P' at the same distance has to be estimated. It turns out that $\Delta\theta$ is related to the distance difference Δr, which can be estimated with high accuracy from the interferometric phase, leading to the important relation of the terrain height h_p

[3]For simplicity, the dependence of the observed point P on the spatial index x (i.e. $P = P(x)$) is not denoted.

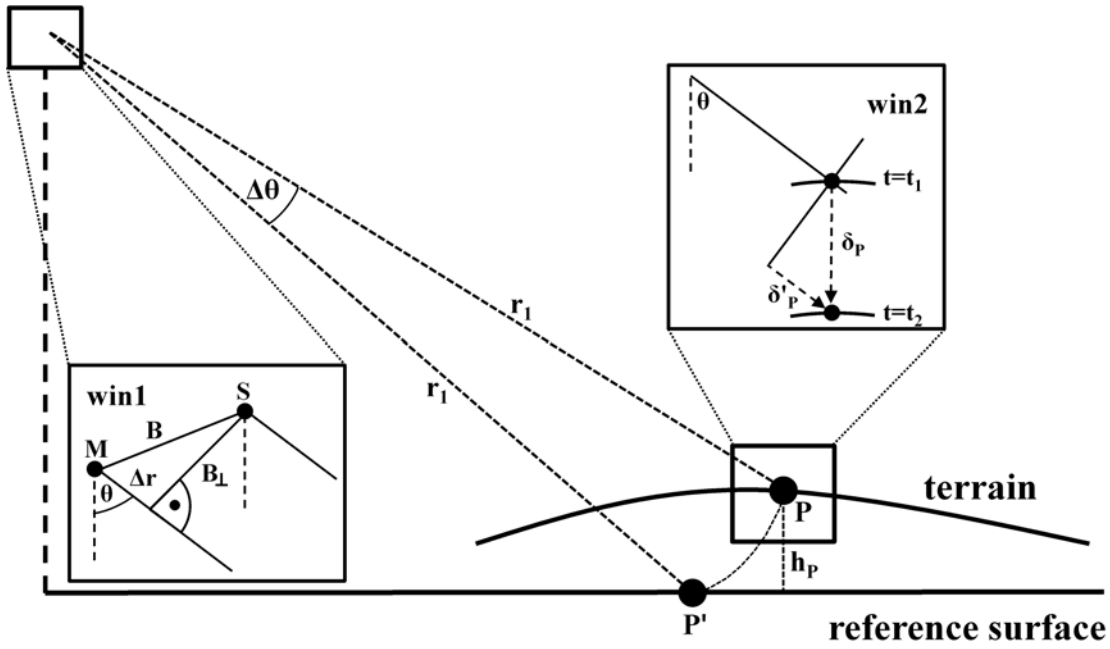

*Figure 2.4.: Sketch of the basic principle of SAR interferometry. A point P on the Earth's surface, which is located at height h_P above the reference surface is observed. Window **win1** shows the geometrical configuration of master and slave acquisition, which are separated by a baseline B. The sensitivity of the interferometer to topography is determined by the baseline $B_\perp$ perpendicular to the range direction. Window **win2** illustrates the effect of deformation. The traversed signal path becomes longer, leading to a phase difference. Only the projection of the deformation vector δ_p into the LoS, termed δ'_P, is measured.*

above the reference surface to the interferometric phase

$$\phi_{topo,x} = -\frac{4\pi \cdot B_\perp}{\lambda \cdot r_1 \cdot \sin\theta} h_P \ . \tag{2.10}$$

It is worth to note that the height h_p of P is related to the point's elevation s_p, which is the distance between the points P and P' (the arc can be approximated by a straight line due to the large target distance). Consequently, $\phi_{topo,x}$ as a function of the elevation s_p can be written as:

$$\phi_{topo,x} = -\frac{4\pi \cdot B_\perp}{\lambda \cdot r_1 \cdot} s_P \ . \tag{2.11}$$

As InSAR is concerned with the determination of DEM, the height is usually used for convenience. However, in SAR tomography the use of the elevation coordinate is more common.

The temporal separation gives rises to the phase term ϕ_{defo}, which is induced by possible surface deformation between the two acquisitions. The situation is shown in figure 2.4 window **win2**. The point P moves between the acquisitions by δ_P in vertical direction. Since the distance difference is measured in slant range direction, only the projection of δ_P onto the LoS of the sensor, termed δ'_P, can be measured

$$\phi_{defo,x} = -\frac{4\pi}{\lambda} \delta'_P \ . \tag{2.12}$$

Finally, by plugging equations (2.10) and (2.12) into (2.9), the flattened interferometric phase can be expressed as a function of height and deformation of point P

$$\Delta\phi_x = -\frac{4\pi \cdot B_\perp}{\lambda \cdot r_1 \cdot \sin(\theta)} h_P - \frac{4\pi}{\lambda}\delta'_P \ . \tag{2.13}$$

The distinction of topographic and deformation phase using one interferogram only is not possible. In order to determine topography, a short revisit time is mandatory. If the deformation is to be estimated, the topographic phase can be removed with an external DEM. Alternatively, methods involving more images, such as the three- or four-pass method (cf. [Hanssen, 2001]), or more sophisticated stacking techniques, such as PSI, can be applied.

In order to characterize the sensitivity of an interferometer to topographic or deformation signal, it is convenient to consider the height or motion corresponding to a full phase cycle[4]. Expressions for both can be easily found using equations (2.10) and (2.12), respectively

$$\delta'_{2\pi} = \frac{\lambda}{2} \ , \tag{2.14}$$

$$h_{2\pi} = \frac{\lambda}{2} \cdot \frac{r_1 \sin(\theta)}{B_\perp} \ . \tag{2.15}$$

The sensitivity to deformation in LoS is by a factor of approximately 1000 better than to topographic signal. This is due to the ratio of the target distance r_1 to the perpendicular baseline $B_\perp$ in (2.15). The former is at the order of some hundreds of kilometers, while the latter is at most some hundreds of meters. Therefore, the determination of the deformation of the observed ground patch with millimeter accuracy is theoretically possible, whereas its location can only be estimated with meter accuracy.

The assumptions leading to equation (2.7) are virtually never completely fulfilled for a repeat-pass interferometer. Spatially distributed scattering, temporally variable signal propagation delay, errors in satellite positioning and attitude control, processing errors, and thermal noise contribute to the measured phase. The plethora of disturbances limits the operational applicability of InSAR and led to the advent of more sophisticated methods involving stacks of interferograms. One of the most prominent examples is PSI, which will be outlined in the next section.

A very important measure for the accuracy of the interferometric phase is the complex correlation between two SAR images, commonly referred to as coherence [Bamler & Hartl, 1998]. It is defined as:

$$\Gamma_x = \frac{E[s_{x,M} \cdot s^*_{x,S}]}{\sqrt{E[|s_{x,M}|^2] \cdot E[|s_{x,S}|^2]}} \tag{2.16}$$

where $E[\bullet]$ denotes the expectation operator. The magnitude of the coherence is confined to values between zero and one (i.e. $0 \leq |\Gamma_x| \leq 1$). Values close to one indicate a very low phase noise, while values close to zero imply a complete loss of coherence (i.e. no exploitable signal). In practice, the

[4] In case of the topographic signal, the term height of ambiguity is often used.

coherence is estimated with a sliding window assuming ergodicity. A discussion of the properties of this estimator can be found in [Hanssen, 2001] and references therein.

2.3. Persistent Scatterers

The limitations of InSAR can be mitigated by exploiting time series of point-like RADAR targets exhibiting temporally stable reflection properties. This is the main idea of persistent scatterer interferometry (PSI). In order to generate the required time series, a stack of N interferograms is created from $N+1$ SAR images. A common master image is chosen and the process of interferogram generation is performed separately for every master slave pair. The extended model accounting for all disturbances of a resolution cell at spatial position x and temporal index i can be stated as [Hooper, 2006]:

$$\phi^{w}_{x,i} = W\{\phi_{defo,x,i} + \phi_{topo,x,i} + \phi_{orb,x,i} + \phi_{atm,x,i} + \phi_{n,x,i}\} \,, \tag{2.17}$$

where $\phi_{orb,x,i}$ incorporates all phase terms caused by orbit inaccuracies. Phase contributions due to time varying signal propagation delay are accounted for by $\phi_{atm,x,i}$. Thermal noise, effects due to distributed scattering, and processing errors are included in the noise term $\phi_{n,x,i}$. Note that equation (2.17) accounts for the fact, that the measured phase is only known up to integer multiples of 2π indicated by the superscript on the left side and the wrapping operator $W\{\bullet\}$ on the right hand side.

The signal propagation delay $\phi_{atm,x,i}$ is caused by the variation of the total electron content (TEC) in the ionosphere and the water vapor concentration of the troposphere along the signal path [Hooper, 2006]. The resulting effect exhibits a spatial correlation length much bigger than the size of a resolution cell [Hanssen, 2001; Zebker et al., 1997] and a temporal correlation length much shorter than the revisit time [Hooper, 2006]. Orbital inaccuracies give rise to an erroneous determination of the geometric phase term $\phi_{geom,x,i}$ [Hanssen, 2001]. The resulting contribution is spatially smooth and exhibits no temporal correlation.

All phase disturbances incorporated in $\phi_{n,x,i}$ exhibit neither spatial nor temporal correlation and can be treated as noise. According to [Hanssen, 2001], those contributions are collectively referred to as sources of decorrelation. The most prominent effects are due to distributed scattering. The single targets within a resolution cell may move incoherently or change their electromagnetic properties between master and slave acquisition. This phenomenon is referred to as temporal decorrelation and is particularly dominant in vegetated areas. Due to slightly different illumination directions of master and slave (i.e. $B_\perp \neq 0$), the distances to the targets change, altering the phase of the sum signal. The effect is referred to as spatial or baseline decorrelation [Hooper, 2006; Zebker & Villasenor, 1992]. A comprehensive description of the sources of decorrelation including quantitative evaluations can be found in Hanssen [2001].

It is important to note that the most significant contributions to the phase term $\phi_{n,x,i}$ vanish if a temporally stable point scatterer is observed. Temporal stability requires the target to exhibit

constant electromagnetic properties and deformation which is correlated in time. As shown in Hooper [2006] for a resolution cell similar to figure 2.2 (b), the mentioned effects are present but much weaker than for situations similar to figure 2.2 (a). By focusing on such targets, the estimation of the topographic and the deformation signal by means of a spatio-temporal analysis becomes feasible.

A first approach to PSI was introduced in the early 2000s by Ferretti et al. [2001]. Since then several augmentations as well as different processing frameworks by other groups have been published [Ferretti et al., 2000; Hooper, 2006; Kampes, 2006; Adam et al., 2003; Liu et al., 2009]. All approaches basically exploit the different spatio-temporal correlation properties of the phase contributions to discriminate the signal of interest from disturbances. Since PS are less strongly affected by decorrelation effects (i.e. $\phi_{n,x,i}$ is small), the main task is to remove the atmospheric contribution $\phi_{atm,x,i}$ and the phase term due to orbital inaccuracies $\phi_{orb,x,i}$. As both contributions are spatially correlated, the effects are heavily reduced by taking phase differences of neighboring PS, enabling the estimation of deformation and height increments [Ferretti et al., 2000]. This is done by considering the time series of double differences relative to some model of the temporal evolution of the deformation phase. In most cases a parametric description of the deformation is employed [Ferretti et al., 2000; Kampes, 2006], but also non-parametric approaches are possible [Hooper, 2006]. In case a functional model is used, a parameter estimation problem given phase values which are only known up to integer multiples of 2π (i.e. the observations are wrapped) has to be solved. This can, for instance, be achieved by means of a periodogram estimator [Ferretti et al., 2000; Rife & Boorstyn, 1974] or with the LAMBDA estimator, known from GPS processing [Kampes, 2006; Teunissen, 1995]. Deformation and height estimates for the PS are retrieved by integration of the determined increments. In order to assure a consistent solution, a redundant number of double differences is formed (e.g. by Delaunay triangulation), enabling a proper handling of estimation errors.

In this work results of the PS processor included in the Generic System for Interferometric SAR (GENESIS) of the German Aerospace Center (DLR) are used. The data have been gratefully provided by DLR and the remote sensing group of Technische Universität München (TUM) within the Very High Resolution Synthetic Aperture Radar (VHR SAR) project. It is worth to point out that GENESIS is a very well tested and reliable PSI algorithms [Adam et al., 2009]. This is very advantageous for this work as all investigations are based on trustworthy results. A general system overview is given in Adam et al. [2003]. A detailed description of the processing chain and the models utilized for the generation of the results employed in section 4 can be found in [Kampes, 2006; Gernhardt, 2012]. The method can be divided into three steps:

1. Detection of PS
2. Reference Network Estimation
3. Final Estimation and Geocoding

2.3.1. Detection of PS

In order to detect PS, an estimate of the phase noise $\phi_{n,x,i}$ is desirable. However, it is hard to infer this value from the phase observations directly because the noise term is masked by all other contributions appearing in equation (2.17). Also the interferometric coherence, defined in equation (2.16) and calculated with a sliding window, is not an appropriate measure since it leads to either low resolution or a large number of false positives [Ferretti et al., 2001]. Instead, the phase noise can be directly estimated from the amplitude data [Adam et al., 2004; Ferretti et al., 2001]. In this case the signal to clutter ratio (SCR) is used. It is determined for every pixel using a certain spatial estimation window[5] and is linked to the standard deviation of the phase noise by the following relation.

$$\hat{\sigma}_\phi \approx \frac{1}{\sqrt{2 \cdot SCR}} \tag{2.18}$$

According to Gernhardt [2012], a SCR of 2 is a reasonable threshold corresponding to PS with $\sigma_\phi < 0.5$. All pixels that exhibit a SCR above threshold are retained and referred to as persistent scatterer candidates (PSC).

2.3.2. Reference Network Estimation

The locally best PSC are used to build a reference network. As described above deformation and height increments are estimated employing the difference phase of neighboring PSC. In order to mitigate the influence of the atmospheric and the orbital phase contributions, the PSC within the reference network are chosen sufficiently close to each other. Every point is linked to as many other points as possible, depending on the distance, to ensure redundancy. The link between two PSC is called an arc. The wrapped phase difference of two neighboring PSC at positions x and y respectively can be stated as

$$\Delta\phi^w_{x,y,i} = W\{\Delta\phi_{defo,x,y,i} + \Delta\phi_{topo,x,y,i} + \Delta\phi_{noise,x,y,i}\} \, , \tag{2.19}$$

where $\Delta\phi_{noise,x,y,i}$ contains all disturbances due to differences of the atmospheric and orbital phase terms and decorrelation noise. The deformation is modeled as a parametric function of time accounting for a linear trend and seasonal motion (cf. [Gernhardt, 2012]).

$$\Delta\phi_{defo,x,y,i} = -\frac{4\pi}{\lambda} \cdot (\Delta v_{x,y} \cdot T_i + \Delta\nu_{x,y} \cdot \sin(2\pi \cdot T_i) - \Delta\xi_{x,y} \cdot (\cos(2\pi \cdot T_i) - 1)) \tag{2.20}$$

where T_i denotes the temporal baseline (in years) and $\Delta v_{x,y}$ the difference of the deformation velocity between the points x and y in LoS of the sensor. The parameters $\Delta\nu_{x,y}$ and $\Delta\xi_{x,y}$ are related to the differential amplitude of the seasonal motion $\Delta\alpha_{x,y}$ and the offset of the estimated sinusoid t_0 by:

$$\Delta\nu_{x,y} = \Delta\alpha_{x,y} \cos(2\pi t_0) \, , \tag{2.21}$$

$$\Delta\xi_{x,y} = -\Delta\alpha_{x,y} \sin(2\pi t_0) \, . \tag{2.22}$$

[5] In contrast to coherence estimation, the size of the window can be chosen quite small.

The topographic phase can be expressed as a linear function of the perpendicular baseline (cf. equation (2.10)), where r and θ refer to the target distance and the incidence angle in the geometry of the master acquisition, respectively.

$$\Delta\phi_{topo,x,y} = -\frac{4\pi \cdot B_{\perp,i}}{\lambda \cdot r \cdot \sin(\theta)} \Delta h_{x,y} \tag{2.23}$$

The estimation is carried out per arc, using the LAMBDA method. The integration of the increments within the network to obtain estimates for the PSC as well as the rejection of erroneous arcs and points are performed according to Liebhart et al. [2010]. All PSC consistent with the network are accepted as PS. The result is an estimate of deformation (i.e. the magnitude of linear and seasonal motion) and topography of all PS in the reference network relative to a reference point. Additionally, a covariance matrix is available for the determined parameters.

2.3.3. Final Estimation and Geocoding

Finally, all PSC exhibiting a SCR above a certain threshold which are not already included in the reference network are processed. Every PSC is linked to the next PS of the reference network and a parameter estimation as described above is conducted. A PSC is discarded if it shows unrealistic parameter estimates or residuals to the assumed model above a certain threshold. Otherwise, the PSC is accepted as PS. In order to account for unmodeled deformation, the residual phase (with respect to the assumed model) can be further analyzed (cf. [Kampes, 2006] for a detailed description).

For every PS the position in a geographic coordinate system has to be determined. The orbital state vectors of the satellite and the position of the PS in the range-azimuth plane constrain the position to a circle. The center of the circle is the point on the satellite's orbit corresponding to the azimuth position of the PS, while its radius is determined by the slant-range location of the PS. The final position can be found by intersection of this circle with a surface defined by the reference body and the height of the PS.

2.3.4. Precision of PS location

It is convenient to discuss the precision of the PS location in the orthogonal coordinate system given by the axes range, azimuth, and elevation. Range and azimuth location of a PS are determined via coherent correlation of the so called meanmap (i.e. the temporal average image of the stack) with the impulse response function of an ideal point scatterer. In Gernhardt [2012] the precision of such location estimates in range σ_r and azimuth σ_a, assuming uncorrelated clutter, is given as:

$$\sigma_r \approx \frac{0.55}{\sqrt{SNR \cdot NOA}} \cdot \rho_r \ , \tag{2.24}$$

$$\sigma_a \approx \frac{0.55}{\sqrt{SNR \cdot NOA}} \cdot \rho_a \ , \tag{2.25}$$

where ρ_r and ρ_a stand for the range and azimuth resolution, respectively. NOA denotes the number of acquisitions of the data stack. In contrast to equation (2.18), where the SCR is used to describe the point quality, the SNR is used here. SCR is defined as the ratio between the power reflected by relevant targets and the power reflected by irrelevant targets and can be estimated from a SAR amplitude image using a spatial estimation window. In contrast, the SNR of a PS is defined as the power of the signal divided by the power of the noise disturbing the signal of the PS. The location in elevation direction is, in contrast, estimated by analysis of the interferometric phase. The accuracy of such parameter estimates obtained for a single PS depend on the validity of the applied model, the stack configuration, and the noise level associated with the PS. An interesting key figure in this context is the Cramer-Rao Lower Bounds (CRLBs) that describes the lower bound on the estimation variance of any unbiased estimator. In the absence of modeling errors and under the assumption that the difference between signal and model is caused by an additive zero mean Gaussian process only, an expression for the CRLB of the estimated elevation position is given in [Zhu & Bamler, 2011b]

$$\sigma_s = \frac{\lambda \cdot r}{4\pi \cdot \sqrt{2} \cdot \sqrt{NOA} \cdot \sqrt{SNR} \cdot \sigma_B} \,, \tag{2.26}$$

where σ_B denotes the standard deviation of the perpendicular baselines within the data stack and, thus, measures the size of the observational basis. The CRLB of the height estimate σ_h can be obtained by multiplying σ_s with $\sin\theta$. Since the localization precision of PS is discussed referring to the range-azimuth-elevation coordinate system, the use of σ_s is more convenient than σ_h. For a given data stack, equation (2.26) just depends on the SNR of the pixel under investigation. If disturbances due to temporal decorrelation and inaccuracies in the processing chain can be neglected, the coherence is mainly governed by the thermal noise of the SAR system [Bamler & Hartl, 1998]; this condition is usually met for PS supposing proper processing. In this case the SNR can be replaced by the more intuitive coherence using the following relation [Zebker & Villasenor, 1992]

$$|\Gamma| = \frac{SNR}{1 + SNR}. \tag{2.27}$$

By solving equation (2.27) for the SNR and plugging the result into equation (2.26) one obtains:

$$\sigma_s = \frac{\lambda \cdot r}{4\pi \cdot \sqrt{2} \cdot \sqrt{NOA} \cdot \sigma_B} \cdot \sqrt{\frac{1 - |\Gamma|}{|\Gamma|}} \,. \tag{2.28}$$

A plot of the CRLB as a function of the coherence is shown in figure 2.5 as solid line for stack parameters given in table 2.1. Those are typical parameters for a TerraSAR-X image stack. As the orbital tube is quite narrow, the spread of the normal baselines is quite small (e.g. $\sigma_B =$

Parameter	NOA	λ [m]	r [m]	σ_B [m]
Value	25	0.031	673308	100

Table 2.1.: Table of acquisition parameters of hypothetical data stack used to illustrate the CRLB of the elevation estimate as a function of the coherence (cf. figure 2.5)

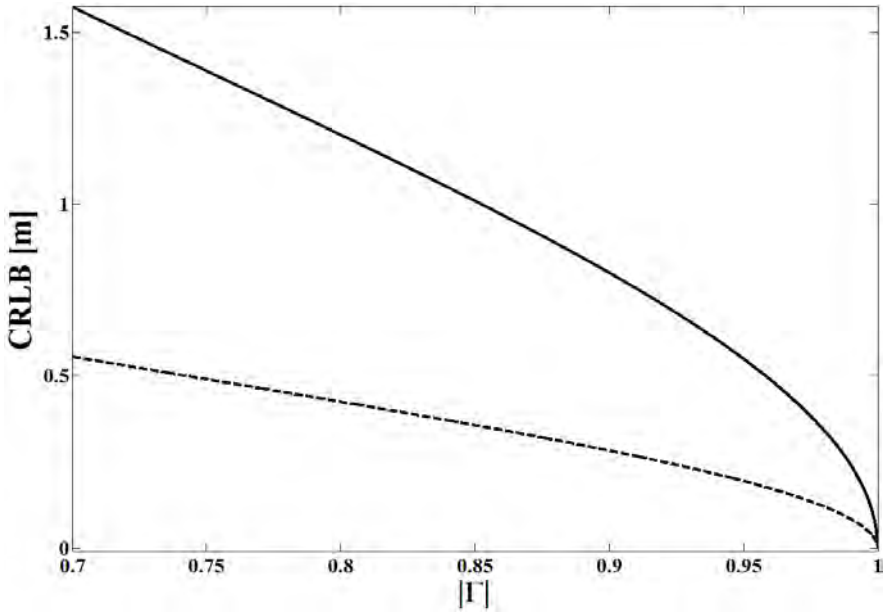

Figure 2.5.: The solid line represents the CRLB of the elevation estimate as a function of the coherence for a stack characterized in table 2.1. The dashed line shows the CRLB for the b057 stack (cf. table 4.1).

100 meter). Furthermore, a number of 25 images is realistic, especially for very high resolution data. For comparison, the dashed line represents the CRLB for the b057 ascending data stack used in section 4 for the experiments. The relevant parameters are reported in table 4.1. Most important, the number of acquisitions amounts to 79 and the baseline spread is around 150 meters. Especially the much bigger number of images of the b057 stack but also the notably larger baseline spread lead to a CRLB being approximately a factor of three smaller than the stack in table 2.1. However, for most areas that many observations are not available. The precision in range and azimuth (σ_r and σ_a) are not plotted in figure 2.5 as they are an order of magnitude smaller than the CRLB in elevation direction. For the b057 stack the ratios σ_s/σ_r and σ_s/σ_a are approximately 24 and 13 respectively. The disbalance is even larger for the data characterized by table 2.1, where σ_s/σ_r and σ_s/σ_a take on values of approximately 34 and 18. Some numeric values of the quantities σ_s, σ_r, and σ_a for both discussed stacks (i.e. b057 and the hypothetical stack with parameters as displayed in table 2.1) for different coherence values are outlined in table 2.2.

	b057			table 2.1		
$\|\Gamma\|$	σ_s[m]	σ_r[m]	σ_a[m]	σ_s[m]	σ_r[m]	σ_a[m]
0.7	0.56	0.024	0.045	1.44	0.042	0.079
0.8	0.43	0.018	0.034	1.10	0.032	0.061
0.9	0.28	0.012	0.023	0.73	0.022	0.040

Table 2.2.: Numeric Values of the quantities σ_s, σ_r, and σ_a for both discussed stacks (i.e. the b057 and the hypothetical stack with parameters as displayed in table 2.1) and different coherence values.

3. Methods

3.1. Grouping of PS at building facades

One of the main aims of this work is the identification of regular horizontal PS patterns. The obtained grouping information can be used to improve the precision of the PS height estimates by imposing constraints on the unknowns. Many grouping strategies could be applied to exploit regular PS pattern: For example, in one dimension (horizontally or vertically), sequentially in both directions to generate a lattice, or directly in two dimensions [Michaelsen et al., 2006]. A comprehensive investigation of pros and cons of such approaches is beyond the scope of this work as, as the focus lies on a grouping scheme that aims at finding horizontal patterns. This offers the opportunity to improve the height estimate, for instance, along rows of windows. The precision of the location estimate benefits from such an enhancement because the PS height is usually the largest error source in the geocoding procedure. Initially, the grouping method is outlined (section 3.1.1) followed by considerations on appropriate parameter settings. Finally, the achievable precision gain is discussed.

3.1.1. Automatic detection of linear PS patterns

Object perception by human vision is believed to be widely governed by rules of Gestalt theory [Desolneux et al., 2004], which comprise concepts such as proximity, good continuation, similarity, and symmetry. Already more than two decades ago automatic reasoning systems have been proposed for computer vision applications taking advantage of such type of rules, like SIGMA [Matsuyama & Hwang, 1990] and SCHEMA [Draper et al., 1989]. Approaches of this category were applied for the analysis of SAR data, but only for amplitude images or single interferogramms and not for PSI. For example, in previous work of our group [Michaelsen et al., 2006, 2010] 2-D grids of salient roof structures and symmetry axes of extended buildings were extracted using production systems. In such approaches the Gestalt principles are coded in terms of production rules, which are executed repeatedly in order to assemble more complex objects starting from a set of primitive objects like points. However, this reasoning was based on amplitude imagery only, which involves the danger to incorporate layover induced outliers into the groups. A rejection of those PS is impossible based on radargrammetric features only. Fortunately, in case of PSI we can use the height estimate of each PS to overcome layover problems at least to some extent.

A search for vertical groups of PS (e.g. PS induced by windows on top of one another) is simply a 1-D problem because they share the same azimuth coordinate. In contrast, horizontal rows of

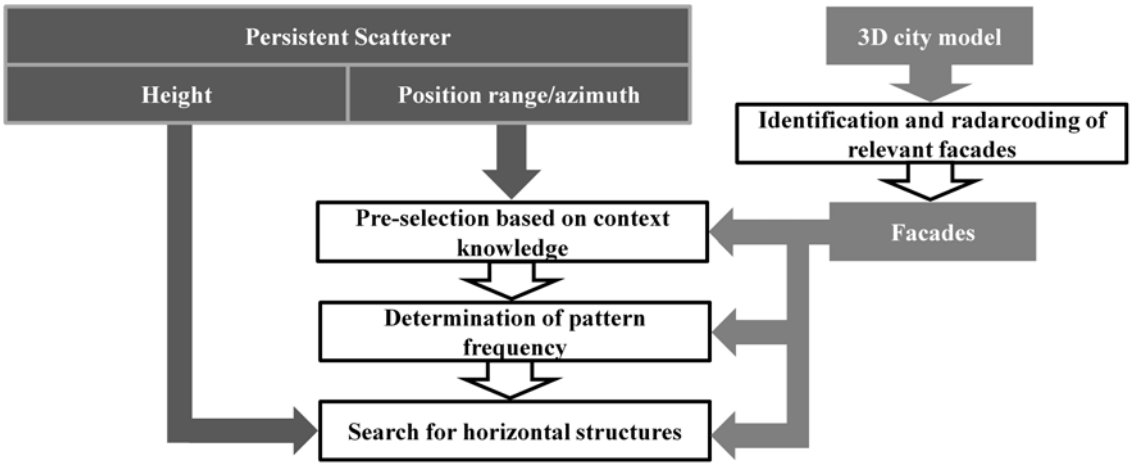

Figure 3.1.: Workflow of the grouping procedure. Image coordinates and estimated height values of the PS are determined within the PSI processing. In order to identify facades visible to the sensor in the 3D city model, the orientations of all vertical faces are compared to the sensors LoS. Facades that are oriented towards the sensor are projected to the SAR image geometry (i.e. radarcoded) and serve as prior information for the location and orientation of PS groups. The height is used to mitigate problems induced by layover.

windows may be oriented arbitrarily in a SAR image. In order to identify such patterns, several 1-D searches in different directions have to be conducted. Depending on the number of PS, this might become unfeasible. On the other hand, horizontal rows must be parallel to the direction of the related building facade.

By introducing context information about the location of the facades visible to the sensor, two advantages arise. Firstly, grouping is facilitated by searching only parallel to the orientation of facades visible to the sensor. Secondly, the search for regular patterns can be limited to the actual frontages, which reduces the computational load. Finally, model knowledge about the typical spacing of floors and windows within a floor can be incorporated.

An overview of the grouping procedure developed in this thesis is given in the flowchart depicted in figure 3.1. The PS set and a 3-D city model of the scene are input to the method. All facades visible to the sensor are extracted from the 3-D city model and transformed to the SAR coordinate system. The result is used as context information as outlined above. Such information can also be inferred from a 2-D map of the building outlines (e.g. OpenStreetMap). As no information about the vertical extension of the facades is available in this case, a maximum height has to be assumed for the whole scene. In most cases this should not pose a big problem as such parameter can be chosen to be rather large. This involves the danger to group unrelated PS, however, the chance for that to happen appears quite small because they are unlikely to match the PS pattern of the investigated facade. Obviously, the main advantage of a 2-D map is its general availability.

The grouping itself consists of three steps. Firstly, PS located at the facade under investigation are selected. Secondly, possible spatial pattern frequencies are identified. Finally, the horizontal groups are assembled. A detailed description of the single steps is given in the following sections.

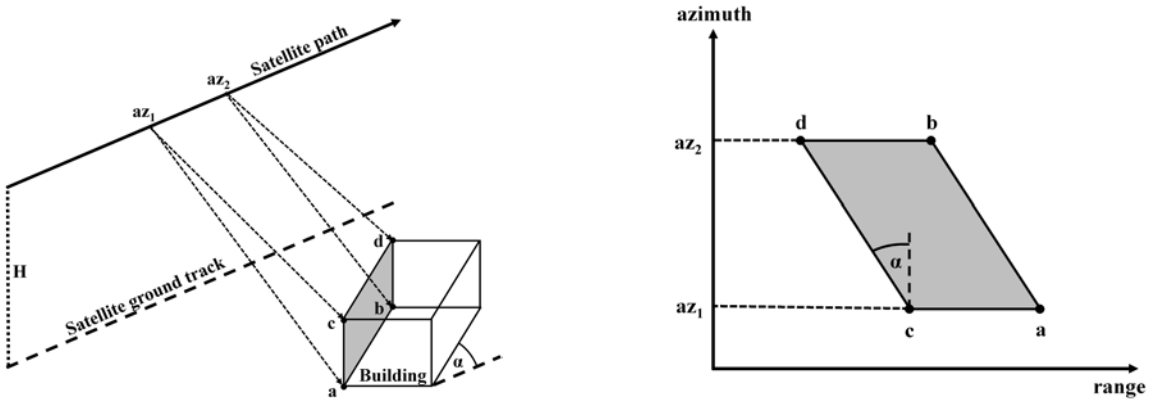

(a) (b)

Figure 3.2.: (a) Acquisition of a building by a SAR sensor. The focus of attention is on the facade shown in gray with its vertices a, b, c, and d. The angle between the facade and the flight direction of the sensor is α. (b) Schematic representation of the facade in the range-azimuth geometry. The facade has the shape of a parallelogram with a shear angle of α.

Primitive Selection

The grouping procedure is applied separately to every facade. Consequently, only the PS that are likely to be located on the facade under investigation are considered. In order to identify those points, prior knowledge about the location of the facade in the SAR image is used. The principle is depicted in figure 3.2. While the situation in the real world is shown on the left (figure 3.2 (a)), the right side (figure 3.2 (b)) illustrates the appearance of the facade in the range-azimuth plane. It is represented by its four vertices a, b, c, and d and is rotated with respect to the sub satellite track by an angle α[1]. In the SAR image the facade has the shape of a parallelogram with a shear angle of α. Only PS that are located within the area shaded in grey in figure 3.2 (b) are considered for the subsequent grouping.

Estimation of pattern frequency

In order to determine the dominant pattern frequencies appearing at a facade under investigation, the distances along the building outline between PS which are likely to be located at the same height are evaluated. An example is displayed in figure 3.3. In (a) the outline of the facade (red line) and the associated PS (blue dots) are shown in range-azimuth coordinates. As the grouping is conducted in direction of the outline, the spacing between points having similar distance to the outline along range direction has to be evaluated. In order to simplify the estimation of pattern frequencies, the setting in (a) is transformed to a coordinate system with the abscissa pointing in the direction of the outline (referred to as X' axis) and the ordinate oriented along range direction (termed Y' axis). This is advantageous because the grouping is conducted along X' direction for rows of PS having similar Y' coordinate, which reduces costly geometric operations to the computation of

[1]The angle α is defined within the Universal Transverse Mercator Coordinate System (UTM) grid

simple coordinate differences. The resulting situation is displayed in figure 3.3 (b). The coordinates $(\mathrm{X}', \mathrm{Y}')$ of a PS located at position (rg, az) in the original range-azimuth coordinate system are obtained by multiplication with transformation matrix $\mathbf{T}$:

$$\begin{bmatrix} \mathrm{X}' \\ \mathrm{Y}' \end{bmatrix} = \mathbf{T} \cdot \begin{bmatrix} rg \\ az \end{bmatrix} = \begin{bmatrix} 0 & \frac{1}{\cos(\alpha)} \\ -1 & -\tan(\alpha) \end{bmatrix} \cdot \begin{bmatrix} rg \\ az \end{bmatrix} . \tag{3.1}$$

Finally, the differences in the X' coordinates of all point pairs exhibiting sufficiently small Y' distance (i.e. smaller than $\Delta\mathrm{Y}'_{tol}$, cf. sections 3.1.2 and 4.2.1) are evaluated. For that purpose kernel density estimation (KDE) is used (cf. [Bowman & Azzalini, 1997] for a detailed treatment). The result is displayed in figure 3.3 (c). All samples (i.e. all X' differences) are illustrated as blue asterisks, while the resulting density estimate is shown as a blue line. The red asterisks mark the local maxima of the density estimate, which are used as possible spacings in the subsequent line assembly. A periodic structure featuring a certain point spacing will, thereby, result in many maxima located at integer multiples of this basic interval. It is possible to detect and erase those redundant spatial frequencies. However, single PS are often missed in the generation process. As the proposed algorithm cannot cope with such situation, some integer multiples of the detected distances have to be checked. It is worth noting that the range of accepted spatial frequencies is limited by knowledge of the typical spacing of facade details.

Assembly of Lines

The set of points selected for the facade under investigation is searched for lines parallel to the building outlines. For simplicity, the procedure is conducted in the (X',Y') coordinate system. A simple approach to enforce rows parallel to the investigated facade is presented in Schunert & Soergel [2012]. Beginning at the outline, rectangular search regions with a certain width[2] are defined and consecutively shifted in Y'-direction. All PS that are located within such a region at the same time are searched for periodic patterns of PS. This approach has two main disadvantages. Firstly, the rectangular search areas do not allow for a modeling of the orientation uncertainty of the outline. Actually, the maximum allowed Y'-difference between two PS should depend on their distance along the outline. Secondly, using a search region which is consecutively shifted in order to find horizontal rows is either computationally intense (in case the shift is small) or involves the danger to miss the actual Y'-location of the row by far (in case the shift is large). Instead, in an improved approach every PS located at the facade under investigation is taken to be the starting point of a row hypothesis. The procedure outlined in the following is conducted for each of those hypotheses. The PS starting it is called the reference PS. Points located in more than one group are dealt with in post processing.

In a first step, the Y'-differences, referred to as $\Delta\mathrm{Y}'$, between the reference PS and all other PS are determined. Two PS located at one facade at the same height have to exhibit a similar Y' (i.e. a

[2]The length of the search region is determined by the length of the used outline.

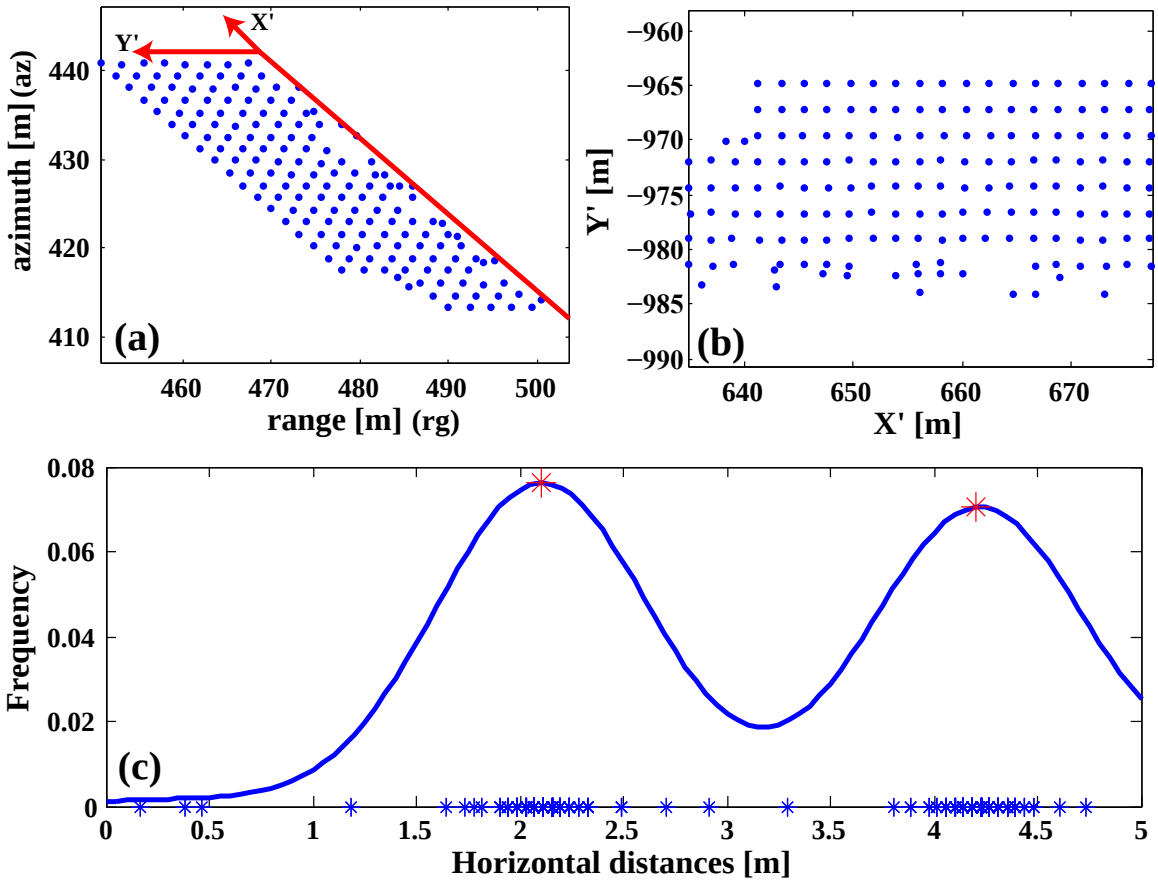

Figure 3.3.: (a) Outline of a facade (red line) and associated PS (blue dots) in range-azimuth geometry. (b) Associated PS in a coordinate system having its abscissa (X′) in the direction of the outline and its ordinate in range direction. (c) Resulting density estimate (blue line) of X′-differences of PS pairs exhibiting sufficiently small range differences (i.e. smaller than $\Delta Y'_{tol}$). The blue asterisks show the available samples. The local maxima of the density estimate are marked as red asterisks.

small $\Delta Y'$ is a necessary condition). Thus, only PS whose Y′-difference is below a threshold $\Delta Y'_{tol}$ are considered in the following search for periodic patterns. The employed threshold is not constant for all PS, but depends on the standard deviation of $\Delta Y'$ which is estimated using a statistical model. This is outlined in more detail in section 3.1.2.

The search for periodic patterns is schematically displayed in figure 3.4. Starting from the reference PS two search areas, one for each direction, for possible successors are defined (shown in green). The distance in X′-direction of the triggering PS to the search areas is determined according to the identified spatial frequencies of the window pattern. The width of the search area, denoted $\Delta X'_{tol}$, controls the tolerance to deviations from the assumed point spacing. If a successor is found, its height estimated in the PS analysis is compared with the height of the triggering PS. In case the absolute height difference is below a threshold, the successor is added to the group and a subsequent search area is defined. This is iterated until no valid successor is found anymore. The consideration of the height is necessary to eliminate PS which are not located at the facade under investigation

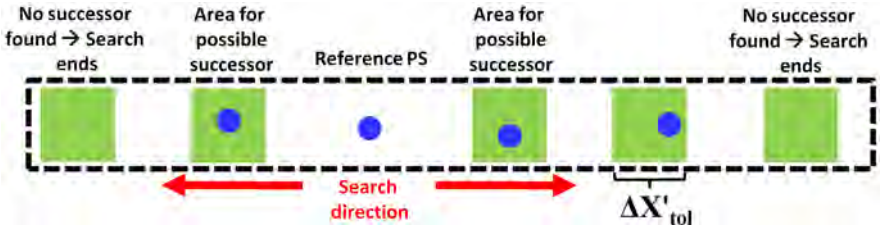

Figure 3.4.: Illustration of the search process. Starting from the reference PS, a search area is defined. If a PS is found therein, it is added to the group and a new search area is constructed. The process terminates if no successor is found. Since the reference PS may be located at an arbitrary X′ position, the outlined process is applied equivalently to both sides.

but mapped to the examined part of the image, e.g. due to layover. Using the determined height during grouping is, admittedly, problematic as we attempt to improve an estimate of the same quantity. However, the applied threshold is quite relaxed (three meters are used in the experiments) compared to the dispersion of the height estimates we seek to minimize. It is worth to note that the obtained solution is not necessarily unique. If two PS feature a very small distance in X′-direction (i.e. $\Delta X' < \Delta X'_{tol}/2$) and are close to the same set of PS in Y′-direction, the grouping algorithm returns two contradictory groups of the same lengths. However, in most cases the threshold $\Delta X'_{tol}$ (cf. section 3.1.2) is well below the smallest possible spacing between PS. Thus, such cases are unlikely to occur.

3.1.2. Parameter Settings

The outlined grouping method is very much based on hard thresholds. Finding suitable values for those thresholds is critical for the performance of the procedure. Using relaxed tolerances leads to complete results but may induce many false positives (i.e. unrelated PS are grouped). Applying strict thresholds causes many false negatives (i.e. actual groups are missed). At this point reasonable thresholds for the parameters $\Delta X'_{tol}$ and $\Delta Y'_{tol}$, which control the tolerance to distance variations between two PS in X′- and Y′-direction, respectively, are derived. Since all other parameters are less critical for the performance of the method, appropriate settings are discussed in section 4.2.1 dealing with the grouping experiments.

Useful tolerances can be determined by considering the statistical variation of the differences in X′- and Y′-direction, referred to as $\Delta X'$ and $\Delta Y'$. Their standard deviations, $\sigma_{\Delta X'}$ and $\sigma_{\Delta Y'}$, can be determined using variance propagation (a detailed treatment of this topic is given in Mikhail & Ackermann [1982]). Both, $\sigma_{\Delta X'}$ and $\sigma_{\Delta Y'}$, depend on the precision of the PS positions in the SAR image and the uncertainty of the outline orientation. The former can be estimated using formulas (2.24) and (2.25), respectively. As the precision of the outline orientation σ_α is unknown, a reasonable value is adopted.

In order to apply variance propagation, $\Delta X'$ and $\Delta Y'$ have to be expressed in terms of the PS positions in the range-azimuth coordinate system and the outline orientation. Here, two PS with coordinates (rg_1, az_1) and (rg_2, az_2) (equivalently (X'_1, Y'_1) and (X'_2, Y'_2) in the X′Y′ coordinate

system) are considered. For simplicity the SNRs of the PS are assumed to be equal. The Y′-difference $\Delta Y'$ can be expressed in terms of range- and azimuth-position and outline orientation using equation (3.1):

$$\Delta Y' = Y'_2 - Y'_1 = rg_1 - rg_2 + (az_1 - az_2) \cdot \tan\alpha \; . \tag{3.2}$$

The partial derivatives with respect to the random variables are:

$$\frac{\partial \Delta Y'}{\partial rg_1} = 1 \; , \tag{3.3}$$

$$\frac{\partial \Delta Y'}{\partial az_1} = \tan\alpha \; , \tag{3.4}$$

$$\frac{\partial \Delta Y'}{\partial rg_2} = -1 \; , \tag{3.5}$$

$$\frac{\partial \Delta Y'}{\partial az_2} = -\tan\alpha \; , \tag{3.6}$$

$$\frac{\partial \Delta Y'}{\partial \alpha} = \frac{az_1 - az_2}{\cos^2\alpha} = \frac{X_1 - X_2}{\cos\alpha} \; . \tag{3.7}$$

The equality in equation (3.7) holds due to the definition of the transformation given in (3.1). Assuming that the random variables are mutually uncorrelated, $\sigma_{\Delta Y'}$ is given by:

$$\sigma_{\Delta Y'} = \sqrt{2 \cdot \sigma_r^2 + 2 \cdot \tan^2\alpha \cdot \sigma_a^2 + \left(\frac{X_1 - X_2}{\cos\alpha}\right)^2 \cdot \sigma_\alpha^2} \; . \tag{3.8}$$

Similarly, $\Delta X'$ is related to the range-azimuth coordinates and the outline orientation by equation (3.1):

$$\Delta X' = X'_2 - X'_1 = \frac{az_2 - az_1}{\cos\alpha} \; . \tag{3.9}$$

The partial derivatives with respect to the random variables az_1, az_2, and α are:

$$\frac{\partial \Delta X'}{\partial az_1} = -\frac{1}{\cos\alpha} \; , \tag{3.10}$$

$$\frac{\partial \Delta X'}{\partial az_2} = \frac{1}{\cos\alpha} \; , \tag{3.11}$$

$$\frac{\partial \Delta X'}{\partial \alpha} = -\frac{az_2 - az_1}{\cos\alpha} \cdot \tan\alpha \; . \tag{3.12}$$

This leads to the following expression for $\sigma_{\Delta X'}$:

$$\begin{aligned} \sigma_{\Delta X'} &= \frac{\sqrt{2 \cdot \sigma_a^2 + (az_2 - az_1)^2 \cdot \tan^2\alpha \cdot \sigma_\alpha^2}}{\cos\alpha} \\ &= \frac{\sqrt{2 \cdot \sigma_a^2 + (X'_2 - X'_1)^2 \cdot \sin^2\alpha \cdot \sigma_\alpha^2}}{\cos\alpha} \; . \end{aligned} \tag{3.13}$$

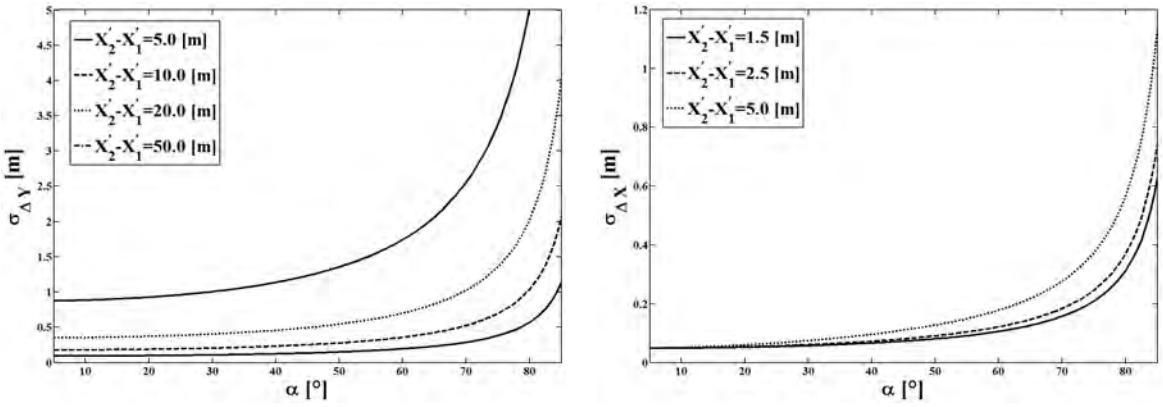

(a) (b)

Figure 3.5.: (a) Estimated $\sigma_{\Delta Y'}$ as a function of the outline orientation α. Different distances in X′-direction between the two PS are shown. The distances are chosen according to typical facade lengths. (b) Estimated $\sigma_{\Delta X'}$ as a function of the outline orientation α. Different distances between the two PS are illustrated, which are chosen relative to the typical spacing of facade elements.

By considering the uncertainty of the outline orientation, $\sigma_{\Delta Y'}$ and $\sigma_{\Delta X'}$ become dependent on the X′-difference. The effect is similar to a leverage. The further the PS are apart, the larger is the error caused by the outline uncertainty. Numerical examples for $\sigma_{\Delta Y'}$ and $\sigma_{\Delta X'}$ as a function of the outline orientation α are shown in figure 3.5 (a) and (b), respectively. The standard deviations of the range- and azimuth-position are taken from table 2.2 for the b057 stack and a coherence of $|\Gamma| = 0.8$ ($\sigma_r = 0.018\ m$ and $\sigma_a = 0.034\ m$). For σ_α, a quite optimistic value of one degree is assumed ($\sigma_\alpha = 1°$). The graphs in figure 3.5 (a) and (b) refer to different X′-differences between the two considered PS. For $\sigma_{\Delta X'}$ X′-differences matching the typical spacing between facade details are chosen (i.e. 1.5, 2.5, and 5 meter). In contrast X′-differences in the range of typical facade lengths (i.e. 5, 10, 20, 50 meter) are adopted for $\sigma_{\Delta Y'}$. This renders the $\sigma_{\Delta Y'}$ much larger than the $\sigma_{\Delta X'}$. The tolerance parameters are directly derived from the $\sigma_{\Delta Y'}$- and $\sigma_{\Delta X'}$-estimates by:

$$\Delta Y'_{tol} = 2 \cdot \kappa \cdot \sigma_{\Delta Y'} \ , \tag{3.14}$$

$$\Delta X'_{tol} = 2 \cdot \kappa \cdot \sigma_{\Delta X'} \ , \tag{3.15}$$

where κ is a scaling factor controlling the confidence level (e.g. $\kappa = 1$ corresponds to a portion of 68% of all differences located within the search area assuming Gaussian distribution). In the experiments the X′-difference is set according to the expected spatial frequency serving as an estimate of the true distance.

3.1.3. Accuracy of group height estimation

In PSI the quantities of interest, usually the linear trend of deformation, the height above a reference point, and in some cases magnitude and phase offset of a seasonal motion, are estimated independently for every PS. In this investigation only the height is considered. In section 2.3.4 an

expression for the CRLB of the elevation estimate is given in equations (2.26) and (2.28) as a function of SNR and coherence, respectively. As elevation and height are equivalent quantities, differing by a constant factor, the former is discussed for consistency. In the following, the achievable precision including grouping information is derived using the CRLB of a single PS as starting point. In order to demonstrate the benefit of the grouping numerically, the theoretical case of a homogeneous group of PS (i.e. all PS within the group exhibit the same SNR) is considered. Finally, the general case of an inhomogeneous group is discussed, which is supposed to be the standard for any real-world application.

Group of homogeneous PS

To demonstrate the benefit of the grouping numerically, the simplest case of a group consisting of N homogeneous PS is considered. Under the hypotheses that all PS share the same elevation position and the associated estimates are equally precise, the single results can be regarded as N equivalent measurements of the same quantity.

The grouping algorithm proposed in section 3.1.1 is robust to outliers since unrelated PS are unlikely to be fulfill all criteria (i.e. similar Y′, X′ close to the spacing, and similar height). Thus, the elevation of the group is estimated by simple averaging. This minimizes the residual sum of squares and is optimal in case the single elevation estimates are normally distributed. Furthermore, this enables the introduction of weights, which is important in the real data case, where the homogeneity assumption is hardly ever met. The minimum standard deviation for the group height estimate obtained by the mean value of N elevation estimates of the individual PS is simply

$$\sigma_{\hat{s}} = \frac{\sigma_s}{\sqrt{N}} = \frac{\lambda \cdot r}{4\pi \cdot \sqrt{2} \cdot \sqrt{NOA} \cdot \sigma_B} \cdot \sqrt{\frac{1-|\Gamma|}{|\Gamma|}} \cdot \frac{1}{\sqrt{N}} \,. \tag{3.16}$$

The resulting lower bounds as a function of the coherence for some values of N (1, 3, 5, and 10) are shown in figure 3.6. The geometric parameters are chosen according to table 2.1. For comparison, the CRLB for the b057 stack (cf. table 4.1) is shown in grey. Since the reduction of the CRLB with increasing group size is proportional to $\frac{1}{\sqrt{(N)}}$, significant improvement already arises by going from no grouping (N=1) to quite small groups (e.g. N=3). In this case the CRLBs for a coherence of 0.9 would be around 80 cm and 46 cm for N equal to one and three, respectively. In order to match the precision of the b057 stack, the group would need to have eight members, which is expected to be quite scarce. However, as already mentioned in section 2.3.4, the b057 shows an outstandingly low CRLB compared to standard stacks, which is due to the many images and the large baseline spread. The outlined estimation of the group height only attenuates error terms which are statistically independent among the members of a group. Such error sources comprise thermal noise and decorrelation effects. However, some errors are expected to be correlated or even identical for the members of one group. Those are either induced by spatially correlated phase disturbances or due to the way the PS network is set up.

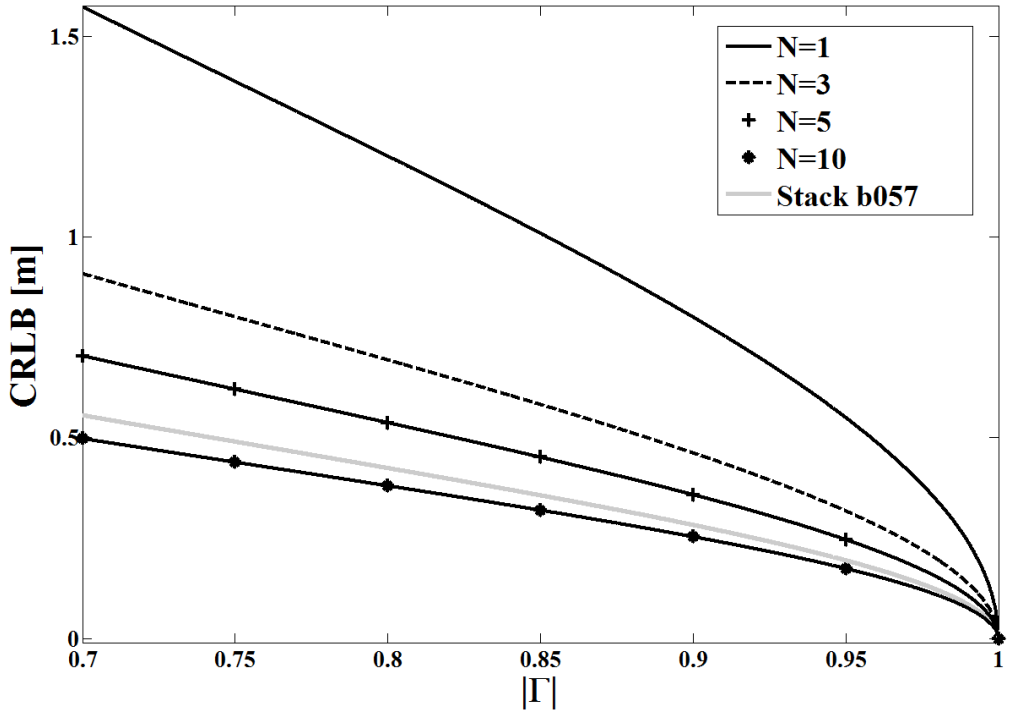

Figure 3.6.: CRLB of elevation estimate for a data stack as given by table 2.1 for coherence values ranging from 0.7 to 1.0 and different group sizes (N=1,3,5,10). For comparison the CRLB of the b057 stack (cf. table 4.1) is shown in grey.

The PSI method included in GENESIS (cf. section 2.3 or [Gernhardt, 2012]) establishes a sparse reference network. Parameter increments between the PS of this network are estimated and subsequently integrated. This leads to correlations among the parameter estimates of those PS. All PSC which are not contained in the reference network are simply appended on the basis of a single connection. Spatially correlated phase errors, such as APS, are usually dealt with by estimating parameter increments between spatially close PS on the basis of phase differences. The rationale for that is the dramatic reduction of spatially smooth phase errors. In case all PS contained in a group are connected to the same point of the reference network, the residual spatially correlated phase errors are very similar. This may, in turn, lead to spatially correlated estimation errors. Certainly, such disturbance could result in a biased estimate of the group height. In case two or more PS of the reference network are contained in one group, the obtained parameters are correlated. Thus, the outlined estimator would fail to give optimal results. However, as the reference network is sparse, this situation is unlikely to occur. If all PS of a group are linked to the same PS of the reference network, all of them share the estimation error of that one PS they are linked to. This would induce a bias similar to a spatially correlated phase error. As the distance of the PS in the reference network is large compared to the size of a typical facade, such case is anticipated to occur very frequently[3]. More complicated cases may arise. The PS of a group could, for instance, be connected to different points of the reference network. In this case the resulting bias would be the weighted

[3]Since geometry and topology of the reference network is not known to the author, the stated assumptions has not been tested.

mean of the estimation errors of the involved PS of the reference network with weights determined by the respective number of connections.

Group of inhomogeneous PS

The previously outlined case, where all elevation estimates in a group feature the same standard deviation, is hardly found in reality. To account for this inhomogeneity, the simple mean value is replaced with a weighted mean value. The generic formulation of the corresponding estimator is:

$$\hat{s} = \frac{1}{\sum_{i=1}^{N} w_i} \sum_{i=1}^{N} w_i \cdot s_i \ , \tag{3.17}$$

where s_i and w_i denote the elevation estimate and its associated weight for the i^{th} PS, respectively. In order to minimize the variance of the estimated group height, the weights have to be chosen proportional to the reciprocal of the variance of the respective observations. Advantageously, the GENESIS PSI processor returns variance estimates $\hat{\sigma}^2_{s,i}$ for the elevation positions, which can be used for weighting. Consequently, the following scheme is adopted in all real data experiments:

$$w_i = \frac{1}{\hat{\sigma}^2_{s,i}} \quad . \tag{3.18}$$

Alternatively, an estimate of the SNR, referred to as $\widehat{SNR_i}$, may be used for weighting. It can be obtained by inversion of equation (2.27), whereas the coherence is replaced by the inter-image coherence $|\hat{\gamma}_i|$. The latter, essentially, measures the fit between the model phase and the measured interferometric phase per PS across all interferograms. More information on this issue can be found in Ferretti et al. [2000], and Ferretti et al. [2001], where the $\widehat{SNR_i}$ are used to assess the PS quality. In Colesanti et al. [2003a] it is shown, that these values are very close to the actual coherence $\left|\hat{\Gamma}_i\right|$ for high SNR targets

$$w_i = \widehat{SNR_i} = \frac{|\hat{\gamma}_i|}{1 - |\hat{\gamma}_i|} \ . \tag{3.19}$$

In case $\widehat{SNR_i} \approx SNR_i$ and $\hat{\sigma}^2_{s,i} \approx \sigma^2_{s,i}$, both weighting schemes lead to the same result as the single weights are proportional. An expression for the CRLB for the the weighted mean can be inferred using the law of variance propagation [Mikhail & Ackermann, 1982]

$$\sigma^2_{\hat{s}} = \sum_{i=1}^{N} \left(\frac{\partial \hat{s}}{\partial s_i} \right)^2 \cdot \sigma^2_{s,i} = \left(\frac{1}{\sum_{j=1}^{N} w_j} \right)^2 \cdot \sum_{i=1}^{N} w_i^2 \cdot \sigma^2_{s,i} \ . \tag{3.20}$$

It is convenient to employ the weighting scheme given by equation (3.19):

$$\sigma^2_{\hat{s}} = \left(\frac{1}{\sum_{j=1}^{N} \widehat{SNR_j}} \right)^2 \cdot \sum_{i=1}^{N} \widehat{SNR_i}^2 \cdot \left(\frac{\lambda \cdot r}{4\pi \cdot \sqrt{2} \cdot \sqrt{NOA} \cdot \sigma_B} \right)^2 \cdot \frac{1}{SNR_i}. \tag{3.21}$$

In case $\widehat{SNR_i} \approx SNR_i$ equation (3.21) simplifies to:

$$\begin{aligned}\sigma_{\hat{s}}^2 &= \left(\frac{\lambda \cdot r}{4\pi \cdot \sqrt{2} \cdot \sqrt{NOA} \cdot \sigma_B}\right)^2 \cdot \frac{1}{\sum_{i=1}^{N} \widehat{SNR_i}} \\ &= \left(\frac{\lambda \cdot r}{4\pi \cdot \sqrt{2} \cdot \sqrt{NOA} \cdot \sigma_B}\right)^2 \cdot \frac{1}{N \cdot \overline{SNR}}\end{aligned} \tag{3.22}$$

where $\overline{SNR}$ denotes the mean SNR of the group. The result stated in equation (3.22) is analogous to the result for the homogeneous group, stated in equation (3.16), save that the SNR, which is assumed constant in this case, is replaced by the average SNR of the group.

3.1.4. Improvement of the group localization

For each group one height value is estimated as outlined above. In order to improve the localization accuracy of the group members, the anisotropic dispersion of the PS positions is exploited. According to section 2.3.4, the standard deviation of the estimated location in elevation is at least an order of magnitude larger than in range and azimuth direction. Thus, the true PS position is approximately situated on a line along elevation direction passing through the originally estimated spot. Each group member is shifted along that line until its z-coordinate matches the determined group height. This is equivalent to repeating the geocoding with the group height instead of the originally estimated PS height.

3.2. Alignment of Persistent Scatterers with 3D city model

In order to relate the PS with a three dimensional city model, potential misalignments between both datasets have to be removed. Although, the PS distribution is correlated with the occurrence of buildings (cf. [Gernhardt, 2012] and section 4.1.1), variable systematic offsets between building model and PS are expected. Those are caused by generalization of the city model and systematic differences between the building structures and the (true) PS locations. For that reason a manual registration, for example using a single or just few tie points, is not recommended as systematic differences may bias all later investigations. Typically, this problem is mitigated as more PS to model correspondences are used, assuming that the systematic effects throughout the scene exhibit some kind of zero mean symmetric distribution. Thus, the registration seeks to minimize the sum of the squared distances between all PS and the building model. Within the alignment, the city model is considered fixed and referred to as the target or model dataset. Contrary, the PS point cloud is termed the source dataset and is transformed in order to match the target.

In the iterative closest point (ICP) algorithm, originally published in Besl & McKay [1992], two successive steps, namely correspondence and transformation estimation, are iterated until some convergence criterion is met. Firstly, point correspondences between source and target are established. Those are used to estimate a rigid transformation in the second step. Finally, the transformation is applied to the source data, which in turn changes the point correspondences. In each iteration every source element is associated with the closest target element. The approach inherently assumes a one to one correspondence between source and target.

Of course, the latter assumption is not realistic in our case. This is mainly due to PS that are not related to any building, such as those which are induced by virtual corner reflectors (cf. section 4.1.1). This issue is addressed by requiring every PS to be located inside the buffered outline of the building it is associated with (cf. section 3.2.1). In this way the most prominent outliers are removed.

3.2.1. Correspondence Estimation

The correspondence estimation is conducted according to Besl & McKay [1992]. The target (i.e. the city model) is given as a set of polyhedrons, described by their bounding surfaces. The set of all such faces is denoted with $\mathbf{F} = \{F_q, q = 1...Q\}$, where each element $F_q = (\mathbf{n}_q, c_q, poly_q)$ is represented by the plane it is located in and a polygon $poly_q$, indicating the extension of the face within the plane. Each plane is described in Hessian normal form by a unit normal vector $\mathbf{n}_q^T = [n_{x,q}, n_{y,q}, n_{z,q}]$ and the distance to the origin in direction of the normal c_q. The source $\mathbf{P}$ (i.e. the PS) is a set of M points, $\mathbf{P} = \{\mathbf{p}_i, i = 1...M\}$ with $\mathbf{p}_i^T = [p_{x,i}, p_{y,i}, p_{z,i}]$.

A simplified case of the assignment of one generic PS $\mathbf{p}_i$ to a rectangular building is shown in figure 3.7. The vertical bounding surfaces of the building and the associated normal vectors are F_1 and $\mathbf{n}_1$, F_2 and $\mathbf{n}_2$, F_3 and $\mathbf{n}_3$, and F_4 and $\mathbf{n}_4$, respectively. In order to find the closest face,

the distance of the PS to all bounding surfaces is determined. The latter is measured along the respective normal vectors (e.g. $d_{\mathbf{p}_i,F_1}$). The PS is, finally, assigned to the closest bounding surface, which is F_3 in the depicted case. In order to limit the computational cost and to eliminate outliers, a PS is only associated with the bounding surfaces of close buildings. For that reason a buffered outline around each building is constructed (indicated by the grey rectangle in figure 3.7). Only the bounding surfaces of those buildings that contain the PS in their buffered outline are considered. The width of the buffer is referred to as W_{ol} (cf. section 3.3).

The outcome of this step is a set of $K \leq M$ correspondences $\mathbf{C} = \left\{(\mathbf{p}_k, F_{nn(\mathbf{p}_k)}), k = 1...K\right\}$, where the $\mathbf{p}_k$ are the PS that are situated in at least one buffered outline. Each of those PS is assigned to exactly one building face $F_{\mathrm{nn}(\mathbf{p}_k)}$. The function $\mathrm{nn}(\mathbf{p}_k)$ returns the index of the closest face for any given input PS $\mathbf{p}_k$, that is $\mathrm{nn}(\mathbf{p}_k) = \mathrm{argmin}_q \left\{d_{\mathbf{p}_k,F_q}\right\}$. For simplicity, the building surface $F_{\mathrm{nn}(\mathbf{p}_k)}$ is referred to as F_k in the following section. Finally, it is worth to note that the

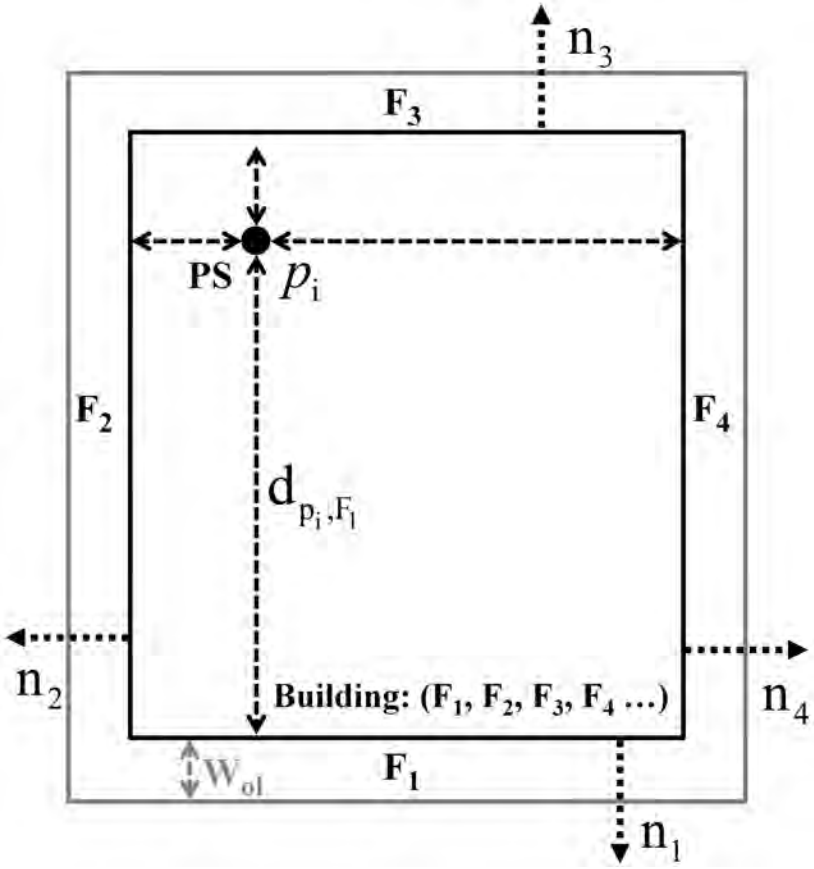

Figure 3.7.: Simplified case of the assignment of one PS to a rectangular building, shown as a topview. The building is bordered by four vertical faces F_1 to F_4 with associated normal vectors $\mathbf{n}_1$ to $\mathbf{n}_4$. In case a PS is located within the buffered outline (indicated by a grey rectangle), all distances to the bounding surfaces of this building are evaluated. The width of the buffer is referred to as W_{ol}. The PS is associated with the closest face.

correspondence estimation is very similar to the final assignment of PS to building models (cf. section 3.3). However, there are two main differences. Firstly, within the correspondence estimation it is

not checked if the perpendicular projection of a PS onto the plane associated with closest bounding surface is located inside the corresponding polygon. Since the correspondence estimation has to be performed in every iteration of the alignment procedure, this check is omitted in order to lower the computational load.

3.2.2. Transformation Estimation

The aim of this step is to determine a transformation that aligns the PS with the assigned building faces. The approach is similar to the one outlined in Low [2004]. However, there are one main difference. The transformation is modeled as a three dimensional shift only (Low [2004] models shift and rotation). Secondly, the error metric is changed to account for the specific covariance structure of the PS positions, i.e. the position is much more precise in range and azimuth compared to elevation.

The three dimensional shift is represented by vector $\mathbf{\Delta}$

$$\mathbf{\Delta}^T = \begin{bmatrix} \Delta_x & \Delta_y & \Delta_z \end{bmatrix} , \tag{3.23}$$

where Δ_x, Δ_y, and Δ_z denote the components in x-, y-, and z-direction, respectively. Similar to Low [2004], the transformation is estimated by minimization of the quadratic sum of the point to plane distances. The representation, however, differs as the target dataset is not given as a point set. The distances are found to be:

$$d_{k,\mathbf{\Delta}} = \mathbf{n}_k \left(\mathbf{p}_k + \mathbf{\Delta} \right) + c_k \, . \tag{3.24}$$

Thus, the optimization problem takes the following form:

$$\hat{\mathbf{\Delta}} = \text{argmin}_{\mathbf{\Delta}} \left\{ \sum_{k=1}^{K} \left(d_{k,\mathbf{\Delta}} \right)^2 \right\} \, . \tag{3.25}$$

In order to take the specific covariance structure of the PS into account, a weight w_k is introduced for every correspondence leading to:

$$\hat{\mathbf{\Delta}} = \text{argmin}_{\mathbf{\Delta}} \left\{ \sum_{k=1}^{K} w_k \left(d_{k,\mathbf{\Delta}} \right)^2 \right\} \, . \tag{3.26}$$

The weights are, basically, chosen to be inverse to the expected variances of the point-to-plane distances, which can be deduced by variance propagation using equation (3.24). For simplicity, the normal vectors are assumed to be error free. Thus, only the plane parameter c_k and the PS coordinates are modeled as random variables. Obviously, the PS position $\mathbf{p}_k$ and the associated c_k are independent and are, consequently, treated separately. The position $\mathbf{p}_k$ of a PS is assumed to be normally distributed with zero expectation and covariance matrix $\mathbf{\Sigma}_{\mathbf{p}_k}$. According to section 2.3.4,

the precision of the PS location is much worse in elevation-direction than in range- and azimuth-direction. In order to account for this fact, the covariance matrix is constructed to have eigenvectors parallel to the elevation-, range-, and azimuth-direction of the SAR system, referred to as $\mathbf{x}_{s,k}$, $\mathbf{x}_{r,k}$, and $\mathbf{x}_{a,k}$, respectively (cf. equations (A.9)-(A.11) in appendix A). Using the eigendecomposition of $\mathbf{\Sigma}_{\mathbf{p}_k}$ one obtains:

$$\mathbf{\Sigma}_{\mathbf{p}_k} = \begin{bmatrix} \mathbf{x}_{s,k} & \mathbf{x}_{r,k} & \mathbf{x}_{a,k} \end{bmatrix} \cdot \begin{bmatrix} \sigma_s^2 & 0 & 0 \\ 0 & \sigma_r^2 & 0 \\ 0 & 0 & \sigma_a^2 \end{bmatrix} \cdot \begin{bmatrix} \mathbf{x}_{s,k}^T \\ \mathbf{x}_{r,k}^T \\ \mathbf{x}_{a,k}^T \end{bmatrix} . \tag{3.27}$$

The plane parameter c_k is assumed to be normally distributed with zero expectation and variance $\sigma_{c_k}^2$. The joint covariance matrix $\mathbf{\Sigma}_{\mathbf{p}_k,c_k}$ in block matrix notation reads:

$$\mathbf{\Sigma}_{\mathbf{p}_k,c_k} = \begin{bmatrix} \mathbf{\Sigma}_{\mathbf{p}_k} & \mathbf{0} \\ \mathbf{0} & \sigma_{c_k}^2 \end{bmatrix} . \tag{3.28}$$

In order to apply variance propagation, the Jacobian matrix $\mathbf{J}$ containing the partial derivatives of equation (3.24) with respect to the PS position and the plane parameter c_k is required.

$$\begin{aligned} \mathbf{J}_k^T &= \begin{bmatrix} \frac{\partial d_{k,\mathbf{\Delta}}}{\partial p_{x,k}} & \frac{\partial d_{k,\mathbf{\Delta}}}{\partial p_{y,k}} & \frac{\partial d_{k,\mathbf{\Delta}}}{\partial p_{y,k}} & \frac{\partial d_{k,\mathbf{\Delta}}}{\partial c_k} \end{bmatrix} \\ &= \begin{bmatrix} n_{x,k} & n_{y,k} & n_{z,k} & 1 \end{bmatrix} \end{aligned} \tag{3.29}$$

The variance of the point-to-plane distance $\sigma_{d_k}^2$ is finally given by:

$$\begin{aligned} \sigma_{d_k}^2 &= \mathbf{J}_k^T \cdot \mathbf{\Sigma}_{\mathbf{p}_k,c_k} \cdot \mathbf{J}_k = \mathbf{n}_k^T \cdot \mathbf{\Sigma}_{\mathbf{p}_k} \cdot \mathbf{n}_k + \sigma_{c_k}^2 \\ &= \left(\mathbf{n}_k^T \cdot \mathbf{x}_{e,k}\right)^2 \sigma_e^2 + \left(\mathbf{n}_k^T \cdot \mathbf{x}_{r,k}\right)^2 \sigma_r^2 + \left(\mathbf{n}_k^T \cdot \mathbf{x}_{a,k}\right)^2 \sigma_a^2 + \sigma_{c_k}^2 \end{aligned} \tag{3.30}$$

The optimization problem stated in equation (3.26) is equivalent to the weighted least squares solution of the over-determined linear system of equations derived in appendix A. Solution strategies for such systems can be found in Mikhail & Ackermann [1982].

3.3. Assignment of Persistent Scatterers to city model

The main topic of this work is the assignment of PS to buildings. The approach for this task is similar to the correspondence estimation outlined in section 3.2.1. Furthermore, also the notation of PS locations (i.e. $\mathbf{p}_i,\ i = 1...N$) and building faces (i.e. $\mathbf{F} = \{F_q, q = 1...Q\}$) is equivalent. In particular, each bounding surface is described by a plane and a polygon located within this plane. A PS is attributed to the building face which has the smallest normalized perpendicular distance. The latter is the ratio between the geometric perpendicular distance (cf. equation (3.24) for $\mathbf{\Delta} = \vec{0}$)

and its expected variance (cf. equation (3.30)). Thus, the assignment can be stated as:

$$nn(\mathbf{p}_i) = \text{argmin}_q \left\{ \frac{d_{\mathbf{p}_i,F_q}}{\sigma_{d_{\mathbf{p}_i,F_q}}} \right\} \tag{3.31}$$

where $q \in [1, Q]$ is an index to the set of all building faces (cf. section 3.2.1). To lower the computational complexity, a PS is only related to a building model if its planimetric position lies inside the buffered outline of the model (cf. figure 3.7). In compliance with section 3.2.1 the width of the buffer is referred to as W_{ol}.

Using the normalized instead of the geometric distance is advantageous for two reasons. Firstly, the variable precision of the PS locations and the building faces (cf. section 4.3.1) can be considered. Secondly, normalizing the distances increases their comparability among each other. In case the geometric distances are zero mean Gaussian random variables and the expression for the respective standard deviations hold, all normalized distances are distributed according to a unit normal distribution (see appendix B for a discussion of the validity of this assumption). In order to exclude unreliable assignments, the normalized distance is required to be smaller than a pre-defined threshold.

By only considering the normalized distances to the planes, the actual extensions of the associated building faces are ignored. In order to avoid false correspondences, the perpendicular projection of a PS onto the plane associated with a bounding surface has to be located inside a buffered version of the polygon that is affiliated to every bounding surface. Otherwise, the potential relation is rejected. The width of the polygon buffer is referred to as W_{pl}.

4. Experiments

In this chapter experimental results for the detection of horizontal groups of PS and for the assignment of PS to buildings are presented. The aim of the evaluation regarding the former topic is twofold. First, the performance of the proposed method is assessed. Secondly, the conditions that lead to the emergence of regular patterns of PS at building facades is investigated. Regarding the assignment of PS to buildings, the main objective is to analyze the comparability of the PS point cloud with the city model. Focus lies clearly on the identification of effects hampering such assignment. Besides those two main investigations, the alignment of the PS point cloud to the city model, the assessment of the PS density at buildings, and the relation of PS to facade details are addressed. The alignment is a prerequisite for the assignment procedure. The corresponding discussion demonstrates the convergence behavior of the iterative registration scheme. A very important product derived from the established relations between the PS and the city model is the density map. In this work the latter is used to identify the driving factors influencing the PS density. Finally, the relation of grouped PS (i.e. PS that are part of a horizontal pattern) to facade details is investigated. Focus lies on the geometrical comparison of horizontal structures in LIDAR data, representing the facade details, with a subset of the identified PS groups. In all experiments, PS results obtained from TerraSAR-X high resolution spotlight data are used.

4.1. Test site and datasets

The test site is located around Potsdamer Platz in the city center of Berlin (Germany). A map of the area, overlaid with building outlines taken from OpenStreetMaps, is displayed in figure 4.1. The red rectangle marks the area which is covered by the SAR image sections displayed in figure 4.2. All experiments are conducted using two PS point clouds. One is based on SAR images acquired in ascending pass direction, while the other is obtained from descending data. Additionally, two reference datasets are available: a three dimensional city model and a point cloud acquired with LIDAR. The former is used as main geometric reference and to derive prior information (cf. section 3.1.1) about the location and orientation of building facades used in the grouping procedure. The latter is, among others, used to identify generalization effects present in the city model, which is necessary for the evaluation of the assignment procedure. In the following, the key characteristics of these datasets are introduced.

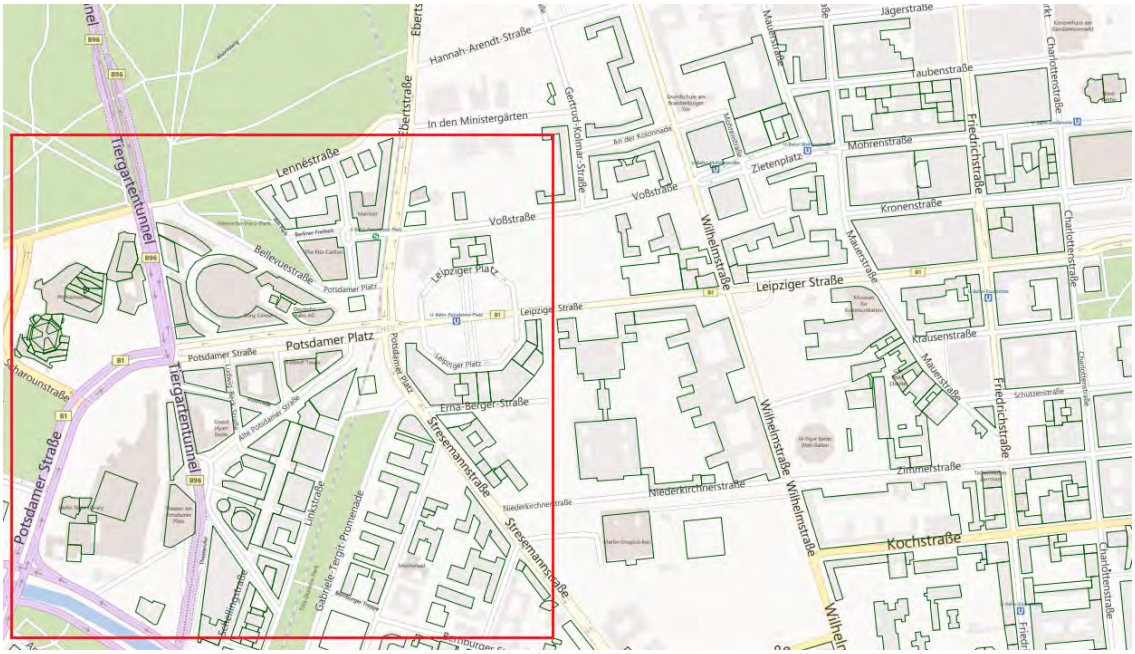

Figure 4.1.: Map of the test site (©Microsoft®Bing™Maps), overlaid with building outlines taken from OpenStreetMaps. The red rectangle marks the area which is covered by the SAR image sections displayed in figure 4.2.

4.1.1. Persistent Scatterers

Two PS point clouds, featuring different pass directions (i.e. ascending and descending), are used within this work. Both have been processed according to section 2.3 using the LAMBDA method included in the GENESIS PSI processor. The images forming either stacks have been acquired in high resolution spotlight mode (i.e. the finest available resolution). The main acquisition parameters of both stacks are summarized in table 4.1. Especially the large number of images contained in both datasets is remarkable. The data are analyzed in two different domains, in SAR image coordinates (i.e. in range-azimuth coordinates) and in real world coordinates (i.e. in the UTM referring to the World Geodetic System 84 (WGS84)). The comparative analysis with respect to the building model is conducted in real world coordinates, while the grouping is done in the SAR image coordinates. It would be conceivable to conduct the latter in real world coordinates. However, the large uncertainties of the elevation coordinates of the PS would complicate the problem tremendously.

Sections of the amplitude mean maps (i.e. the pixelwise incoherent mean value of the amplitudes over all stack acquisitions) of the ascending and the descending dataset for the test site are shown in figure 4.2 (a) and (b), respectively (the complete amplitude mean maps are displayed in figure C.1 and figure C.2 in appendix C). Two effects immediately strike the eye. Firstly, a lot of layover, induced by tall buildings, is present in the scene. Layover areas are often bright and located in front of a salient line (i.e. in negative range direction), which is referred to as the double bounce line [Dong et al., 1997]. It is induced by the summation of all echos involving a reflection on the ground and at the facade. The summation occurs because the length of the traversed paths of all comprised echos

Parameter	b057	b042
Pass direction	Ascending	Descending
θ	41.6° - 42.2°	35.7° - 36.4 °
Heading	350°	191°
NOA	79	94
r	673308 [m]	626190 [m]
σ_B	156 [m]	89 [m]
δ_{sr}	0.59 [m]	0.59 [m]
δ_a^{SAR}	1.1 [m]	1.1 [m]
λ	0.0311 [m]	0.0311 [m]
Start/End date	2008-02-12/2012-03-07	2008-02-04/2012-02-28

Table 4.1.: Table of acquisition parameters of both SAR data stacks

is equal. The respective phase centers are located at the facade ground intersection (i.e. coincident with the building outline). The tower of the German railway service, which is marked by a green rectangle in figure 4.2 (a) and (b) is a good example. As the tower's outline is curved, the double bounce line is bent. The layover effect is stronger for the descending dataset due to the smaller incidence angle. Secondly, a lot of dominant point scatterers are visible, which are very likely to induce PS as their signal is very strong making the phase measurement robust to noise.

The areas marked by the red rectangles are shown as close-ups, including the identified PS, in figure 4.3 (a) and figure 4.4 (a) for ascending and descending dataset, respectively (the data for the complete test area are displayed in figure C.3 and figure C.4 in appendix C). The colors (blue - low altitude to red - high altitude) indicate the estimated height values. A lot of PS are arranged in lattice-like structures, which are aligned with the building outlines visible to the sensor. A typical example is framed by the red rectangle in figure 4.3 (a). The height of the PS that are contained in such patterns mostly increases when going in negative range direction which suggests the patterns to be located at facades. In order to illustrate the connection between the distribution of PS and the facade structures, oblique view aerial images showing roughly the same building parts are presented in figure 4.3 (b) and figure 4.4 (b), respectively. The correspondence is best visible from the building complex covering the complete right half of figure 4.3 (a) and (b). The characteristic lattice-like arrangement of PS transfers almost directly to the PS distribution. The other side of this building complex is visible in the left and lower left part of figure 4.4 (a) and (b), respectively. The PS pattern is present, but not as distinct as in the ascending dataset. A more detailed discussion about this fact is given in section 4.2.2.

In figure 4.5 the area marked by the red rectangle in figure 4.3 (a) is shown on the right. On the left, a terrestrial image of the building facade is shown. The SAR data are rotated in order to roughly match the optical data. As the facade is not perpendicular to the LoS of the sensor, it is skewed in the SAR data. Except for one missing point in the lower left, the number and arrangement of PS matches with the windows at the facade. However, a spot which is slightly in contrast to the dark background (marked by the red circle) is visible, implying that the PS has been missed due to noncompliance with the assumed phase model.

(a)

(b)

Figure 4.2.: Mean amplitude maps of ascending (a) and descending (b) data stack. The green rectangles encompass the tower of the German railway service, which induces massive layover due to its height. The red rectangles enclose an area which is shown as a close up in figure 4.3 and figure 4.4, respectively, including the identified PS.

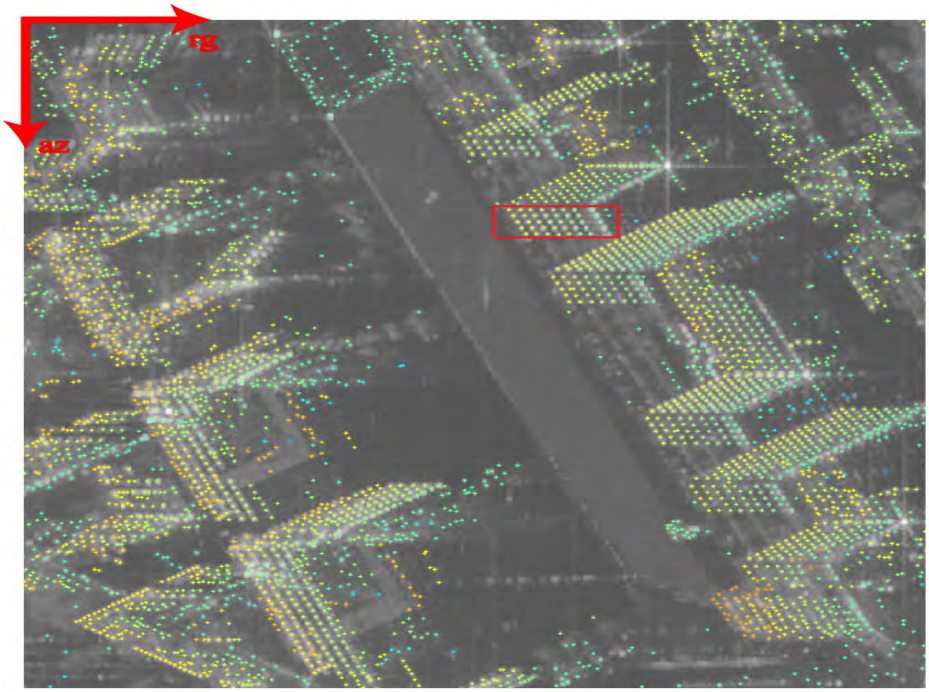

(a)

(b)

Figure 4.3.: Close-up of the area framed by the red rectangles in figure 4.2 (a). (a) The PS identified in the ascending data stack overlaid with the respective section of the mean map. The colors indicate the estimated PS heights (green - low to yellow - high). The facade framed by the red rectangle is discussed in detail in figure 4.5. (b) Oblique view aerial image having approximately the same viewing direction as the SAR data in (a).

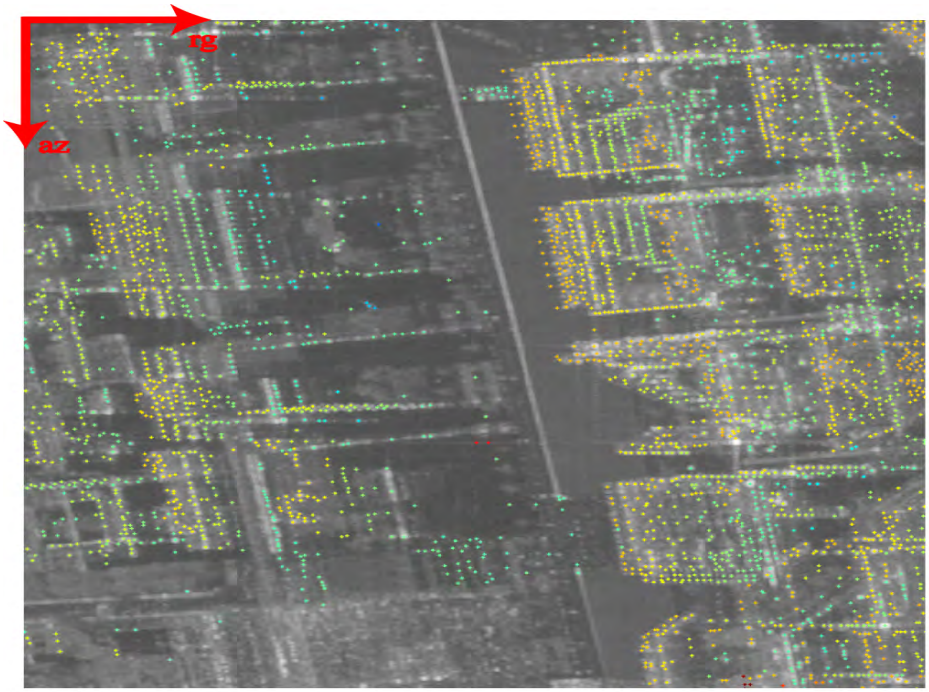

(a)

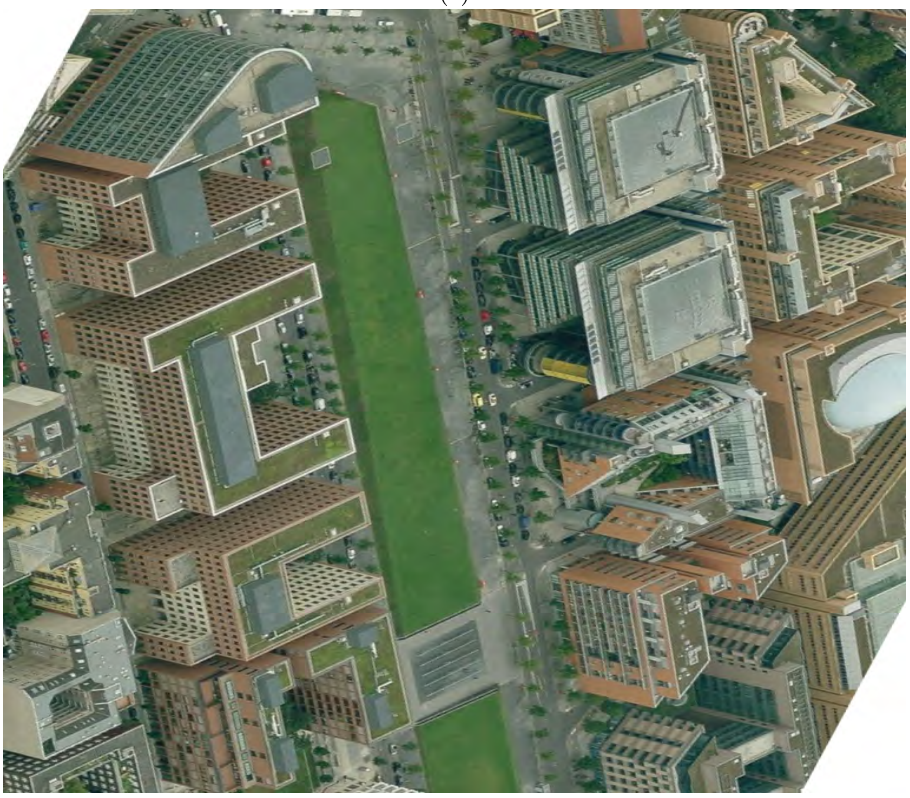

(b)

Figure 4.4.: Close-up of the area framed by the red rectangle in figure 4.2 (b). (a) The PS identified in the descending data stack overlaid with the respective section of the mean map. The colors indicate the estimated PS heights (green - low to yellow - high). (b) Oblique view aerial image having approximately the same viewing direction as the SAR data in (a).

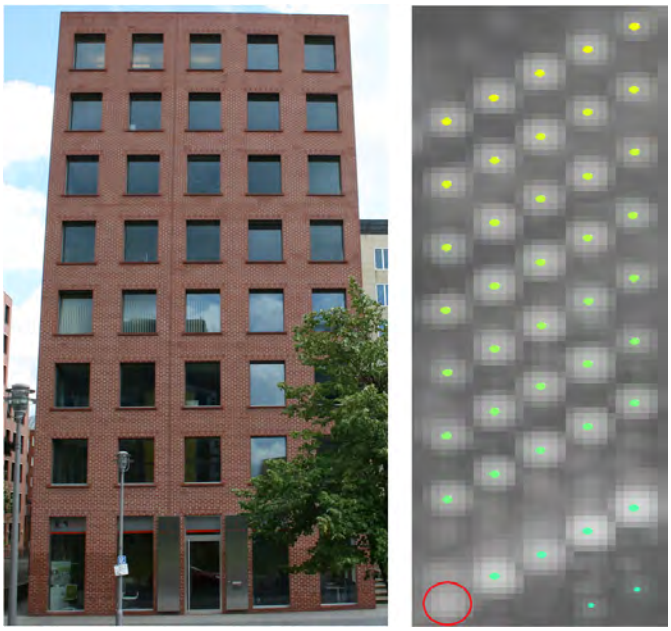

Figure 4.5.: Terrestrial photograph of the facade marked by the red rectange in figure 4.3 (a) on the left and the corresponding SAR data on the right. The SAR data are rotated to approximately match the photograph. The identified PS are shown as colored points. The color indicates the height(green - low to yellow - high). The correspondence between the arrangement of windows and the lattice-like structure of the PS is clearly visible.

The UTM coordinates of the PS are obtained by geocoding. Due to unknown or imperfect knowledge of the height of the reference PS, both point clouds may be shifted from their true position in the respective elevation directions. Since the fusion approach outlined in [Gernhardt et al., 2012] has been applied to the data, this effect is largely eliminated. In this approach two PS point clouds are aligned based on pairs of corresponding PS. As the directions of the residual shifts of both point clouds is known (i.e. elevation), their absolute position can be estimated. The accuracy of such correction is demonstrated in Gernhardt [2012], where differences of the shifts estimated for one PS set in two different configurations (i.e. Ascending/Ascending opposed to Ascending/Descending configuration) around one to two meters are reported. It is worth to note that the PS height, despite the remaining shift, refers to the purely geometric reference surface used to calculate the geometric phase term (cf. section 2.2). In most cases the WGS84 is used for this purpose.

In figure 4.6 both PS sets are displayed as topview. The ascending data are displayed in green, while the descending data are shown in red. Image bottom-top corresponds to map north. In comparison with the map displayed in figure 4.1, it is apparent that most PS are located at building structures. In total, roughly 75000 points are available, 35000 for the descending and 40000 for the ascending dataset. As already assumed on the basis of the range-azimuth data, the majority of the building PS is situated at facades. Since the LoS directions of both datasets are roughly opposed to each other[1], they are complementary. The ascending datasets contains facades facing to the west, while the descending dataset covers frontages oriented to the east. Finally, the alignment

[1]The sensor is always looking to the right with LoS perpendicular to the flight direction.

Figure 4.6.: Ascending (green) and descending (red) PS displayed as topview. Most PS correspond to building structures. Facades, in particular, contain the majority of the PS. The descending data consist of approximately 35000 points, while the ascending dataset is composed of roughly 40000 points. Due to the fusion, both PS solutions are well aligned.

between ascending and descending PS result is clearly visible from the match between the respective facade PS. As outlined above, the majority of the PS are located close to buildings. Experiments based on ray-tracing simulations show that many of those are induced by a threefold reflection at building details that happen to form a trihedral reflector [Auer, 2011]. Usually, the surfaces involved in this reflection are located close to each other or are even adjacent. Of course, PS attributable to buildings may also be induced by other mechanisms. One example is the strong double bounce reflection involving parts of the ground surface and the building facade. Those PS are situated at the intersection between facade and ground (i.e. at the building outline). However, in some cases PS are caused by interaction with buildings, but are located away from all involved structures. Two scenarios are described in the literature to explain such findings: virtual corner reflectors[2], and ghost PS. The former are constituted by unrelated planar surfaces that form a section of a trihedral reflector. For example, two completely unrelated facades that are perpendicularly oriented with respect to each other and the (plane) ground surface may constitute a corner reflector provided there is some clear space between them. Obviously, the phase center of such corner has no real world

[2]The term ghost corner is used synonymously. In this work the term virtual corner is utilized to avoid confusions with ghost PS.

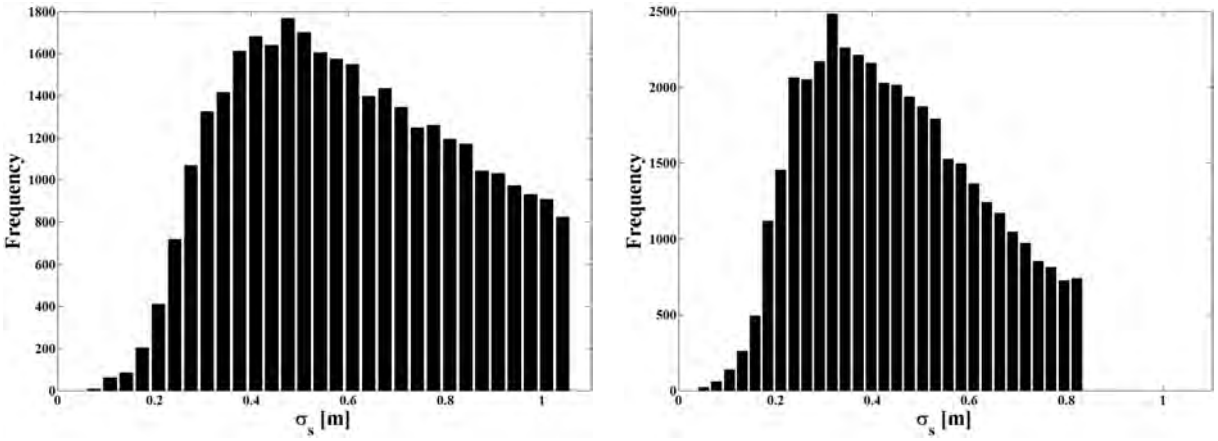

(a) (b)

Figure 4.7.: Histogram of the a-posteriori standard deviations of the elevation estimates for the descending (a) and the ascending (b) dataset. The estimates using the ascending data are more accurate due to the larger baseline span (cf. table 4.1).

correspondence [Auer & Bamler, 2010]. The location of a potentially induced PS depends on the spatial arrangement of the three planes and may be far away from any of the involved buildings. Moreover, the estimated deformation is a mixture of the movement of all three surfaces. Such PS appear to be distributed arbitrarily throughout the scene. Ghost PS, on the other hand, involve two reflections at the ground in addition to the interaction with the building (mostly a threefold reflection) [Auer et al., 2011a]. Due to the longer path length, the PS are seemingly located below ground level. This is similar to the mirror effect observed for bridges over water reported by Soergel et al. [2008]. Both, virtual corner reflectors and ghost PS, disturb the following investigation. Whereas the former are very difficult to identify, ghost PS can be easily recognized and removed using a digital terrain model (DTM), which is done to facilitate the subsequent studies.

One of the main advantages of the LAMBDA estimator (cf. section 2.3) is the inclusion of measurement and parameter uncertainties. Histograms of the a-posteriori standard deviations of the elevation estimates are shown in figure 4.7 (a) and (b) for the descending and ascending dataset, respectively. Although the descending stack contains slightly more images, the results obtained for the ascending dataset are more accurate due to the larger baseline span (cf. table 4.1).

4.1.2. Reference data

Three dimensional city model

The city model available for our investigation has been mostly generated from airborne LIDAR data by automatic building reconstruction and features LOD 2. It has been produced by virtualcitySYSTEMS using an automatic reconstruction algorithm based on [Kada, 2009]. Each building is represented as a triangulated three-dimensional mesh containing a few dozen triangles. In total, all building models comprise approximately 13000 triangles. Two buildings, namely the Kollhoff Tower

and the Sony Center, are modeled in LOD3. The former model contains roughly 12000, while the latter incorporates around 30000 triangles.

According to the Open Geospatial Consortium (OGC) standard CityGML (cf. [Kolbe, 2007]), LOD2 models have to exhibit an absolute accuracy of at least two meters. Furthermore, structures having a footprint larger than 4x4 m^2 have to be included. Similarly, for LOD3 models the maximum allowable error is 0.5 meters and the maximum size of an uncharted object is 2x2 m^2.

Each building is given in its own local coordinate system and is transformed to UTM coordinates using a tie point. In order to position the single buildings at the correct height, a DTM, which is referenced to the official German height reference system (i.e. Deutsches Haupthöhennetz (DHHN)), is used. The altitudes are given as normal heights, referring to the quasi-geoid (cf. Torge [2001]). The planimetric reference of the DTM is the Bessel ellipsoid. Thus, a change of datum is necessary to transform the DTM to WGS84.

LIDAR data

The LIDAR data have been acquired using an airborne sensor. Most of the points are located on horizontal surfaces (i.e. on the ground and on building roofs). In order to better match the city model, the ground points are removed by simple height thresholding, assuming a horizontal ground surface. The point density of these data (after thresholding) is around three to four points per square meter on standard buildings. Approximately 90% of the points are located on the roof, which makes a comparison with the PS point clouds difficult as those feature a much denser sampling at the facades. Height as well as position refer to the WGS84. Due to the different datums of LIDAR and the building models, a shift is observable between both datasets, which is strongest in z-direction. Both datasets are aligned using the registration algorithm described in section 3.2. The dispersion of the LIDAR points is assumed to be isotropic, implying equal weights (i.e. $w_k = 1$ in equation (3.26)). This is a simplification as the precision of the point locations may be non isotropic depending on the acquisition geometry and the system parameters of the LIDAR sensor (cf. [May & Toth, 2007]).

After alignment the signed distances of the LIDAR data to the city model are calculated. In figure 4.8 (a) and (b) histograms of those distances to the vertical and horizontal faces, respectively, are shown. The red lines indicate Gaussians fitted to the histograms. The estimated standard deviations of the bell curves are 0.8 meters and 1.2 meters for (a) and (b), respectively. The mean values are close to zero (10 cm for the facades and -20 cm for the roofs). Especially the distances to the horizontal structures (i.e. to the roofs) show the effects of generalization. Roofs are often quite complicated due to many small superstructures. Fitting simple models (e.g. flat or gable roofs) in a least squares sense, results in systematic underestimation of the superstructures and overestimation of the actual roof. Since facades are typically simpler, the effect is not as strong. This fact is clearly visible in figure 4.8. While the horizontal distances (a) are not strictly distributed according to a gaussian curve, the vertical distances are far from being normally distributed.

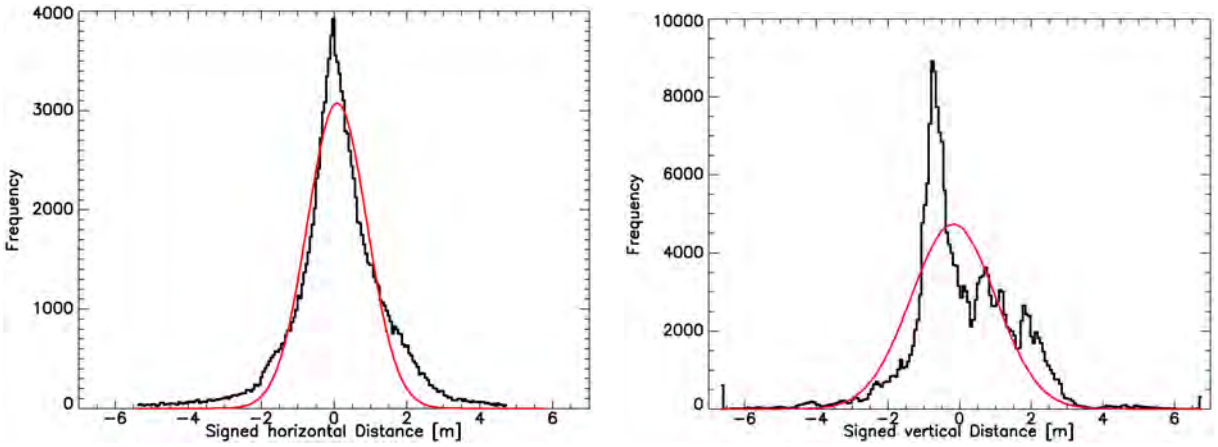

(a) (b)

Figure 4.8.: (a): Histogram of signed distances between vertical faces (i.e. horizontal distances) and LIDAR data, (b): Histogram of signed distances between horizontal faces (i.e. vertical distances) and LIDAR data. Gaussians fitted to the histograms are shown in red. The standard deviations are 0.8 and 1.2 meters, respectively. The estimated shift has been applied before calculation of the distances.

4.2. Grouping of PS at building facades

The grouping method outlined in section 3.1 is applied separately to the ascending and the descending dataset. The performance of the procedure is assessed for one test area. In figure 4.5 an instance of a lattice-like PS distribution is illustrated. The considered facade is a textbook example for a regular arrangement of PS. This may convey the impression that grouping the PS is simple and completely solved using basic methods. As a matter of fact, such clean patterns are quite rare. Considering the other facades in figure 4.3 (a) and figure 4.4 (a), horizontal rows of PS are discernible. However, often the patterns seems to be interrupted or impaired by other PS. In some cases the PS distribution even seems to be completely random. Possible explanations for this behaviour are discussed along with the evaluation of the grouping results. Finally, the grouping information is used to improve the geocoding of the identified horizontal patterns. Although an evaluation of more test areas would be preferable to infer the transferability of the grouping procedure and to identify the critical parameters, results for only one site are presented here. This is due to the fact that no real ground truth is available to automatically assess the algorithms performance. Instead the plausibility of the results has to be determined for every facade using terrestrial photographs or oblique view aerial images.

4.2.1. Parameter Settings

The grouping procedure is mainly influenced by the two tolerance parameters $\Delta X'_{tol}$ and $\Delta Y'_{tol}$. In section 3.1.2 theoretical considerations on appropriate settings are given and numerical examples are illustrated. As $\Delta X'_{tol}$ and $\Delta Y'_{tol}$ depend on the precision of the outline orientation and the PS localization, suitable values for the latter quantities have to be determined. The standard deviation

of the PS positions in range and azimuth are given by equations (2.24) and (2.25), respectively. Both depend on the SNR of the PS at hand. Since no direct information about the PS quality is supplied[3], a mean SNR corresponding to a coherence of $|\Gamma| = 0.8$ (cf. equation (2.27)) is assumed for all PS. It is worth to note, that σ_r as well as σ_a are different for the two PS results as the number of SAR images in the stacks differs (i.e. the precision of stack b042 is slightly better). Analogous to the numerical experiments conducted in 3.1.2, the standard deviation of the outline orientation is set to $\sigma_\alpha = 1°$. The outlines projected to the ascending and the descending mean amplitude images are illustrated in figure 4.9 (a) and (b). Each facade takes the shape of a parallelogram. The vertical boundaries are always oriented along range-direction, while the direction of the horizontal boundaries depends on the alignment between facade and flight path of the sensor (cf. figure 3.2). A comparison of such horizontal borders with the bright double bounce lines, which are quite pronounced in some cases, shows good alignment. In view of that, the assumed σ_α appears to be appropriate. In order to numerically evaluate the uncertainty of the line orientation, the double bounce signatures could be identified and contrasted with the map data. Automatic methods for the detection of double bounce lines exist [Tupin et al., 1998; Touzi et al., 1988]. However, such investigation is beyond the scope of this work as it would require intensive study of such line detectors to separate errors in the map data from shortcomings in the detection process.

Finally, two different scaling factors κ, namely 2 and 3, are considered. Provided that the quantities $\Delta X'$ and $\Delta Y'$ are normally distributed with zero mean and standard deviation as given in equations (3.13) and (3.8), $\kappa = 2$ and $\kappa = 3$ imply that roughly 95% and 99.5% of all realizations are within the tolerances. If $\Delta X'$ and $\Delta Y'$ follow a Gaussian distribution is difficult to investigate analytically. Alternatively, numerical simulations can be used to generate empirical distribution functions for $\Delta X'$ and $\Delta Y'$. However, as the number of parameters that potentially influence the shape of the probability density functions (PDFs) of $\Delta X'$ and $\Delta Y'$ is large, many simulations have to be conducted to cover all possible configurations. Therefore, no further investigation on the probability distributions of $\Delta X'$ and $\Delta Y'$ is conducted within the framework of this thesis. Thus, the confidence intervals stated above, remain hypothetical.

The reason for adopting such high confidence level is that in the developed approach one missed PS already stops the line assembly. If a pattern is composed of N PS, the probability of finding it completely, decreases exponentially with the number of elements in the group. This is due to the fact that the number of necessary comparisons is proportional to N^4.

Besides $\Delta X'_{tol}$ and $\Delta Y'_{tol}$, the bandwidth of the KDE has to be adjusted. It is set to a quite small value of 10 centimeters in order not to miss any actual pattern frequency. The impact of this parameter on the accuracy of the frequency estimation is not evaluated experimentally as it is not considered to be critical. Of course, X′-differences of unrelated PS fulfilling the $\Delta Y'$-constraint

[3] Only indirectly via the height standard deviation.

[4] Of course, heuristics can be found to mitigate such behavior. For instance, if one PS slightly exceeds a threshold, it could be accepted under the condition that it allows the detection of a longer pattern. For simplicity, such heuristics have not been considered.

	σ_r [m]	σ_a [m]	σ_α [°]	κ	BW_{KDE} [m]
b057	0.018	0.034	1.0	2/3	0.1
b042	0.017	0.031	1.0	2/3	0.1

Table 4.2.: Table of settings used for the grouping experiments

(i.e. which are close in Y′ direction) may be contained in the data used to estimate the pattern spacing. Given a small kernel bandwidth, two cases are conceivable. Firstly, one or more erroneous X′-differences are located close to an actual pattern spacing. This may bias the estimate. However, as the kernel function decreases quickly, the effect is unlikely to distort the results dramatically. Secondly, virtual spacings may arise due to wrong X′-differences. Those spurious frequencies are, fortunately, not likely to produce groups in the line assembly step. An overview of all applied settings is given in table 4.2.

4.2.2. Results

The grouping results obtained with the parameter settings outlined in the preceding section are discussed for the test areas depicted in figure 4.3 and figure 4.4. In order to guide the grouping, the facades visible to the sensor are projected to the SAR geometry. This is illustrated in figure 4.9 (a) and (b) for the ascending and the descending dataset, respectively. The facades are depicted as colored parallelograms. In the background the mean amplitude maps are shown. The identified PS are illustrated as blue dots. In most areas the reflections of several facades mix. One exception is the building complex visible in the right half of figure 4.9 (a), where most facades are isolated from each other.

Ascending data

The grouping results for the ascending dataset using κ equal to 2 and 3 are presented in figure 4.10 (a) and (b), respectively. The outlines of facades that triggered the detection of at least one pattern are shown as colored line segments. The corresponding groups are indicated by large connected dots of the same color. In the background the mean amplitude image is depicted. Only PS that are located within at least one facade footprint are considered in the grouping. Those are illustrated as small blue dots. In either result the majority of groups are identified at the building complex in the right half. There are two reasons for the plethora of groups identified there. Firstly, the very regular distribution of windows at the facades leads to remarkably regular patterns (cf. figure 4.3). Certainly, the design of the windows itself is also of importance, since many other facades exhibit a very regular distribution of windows but do not accommodate many useful PS patterns. Secondly, as outlined above, the facades of this building complex are quite isolated (cf. figure 4.9 (a)). In this way the regular patterns are not disturbed by layover. Regarding the influence of the window setup, it is interesting to consider the facades in figure 4.10 (a) marked by the dashed red rectangles (1)-(3). Close-ups of the corresponding windows are displayed in figure 4.11. All setups lead to

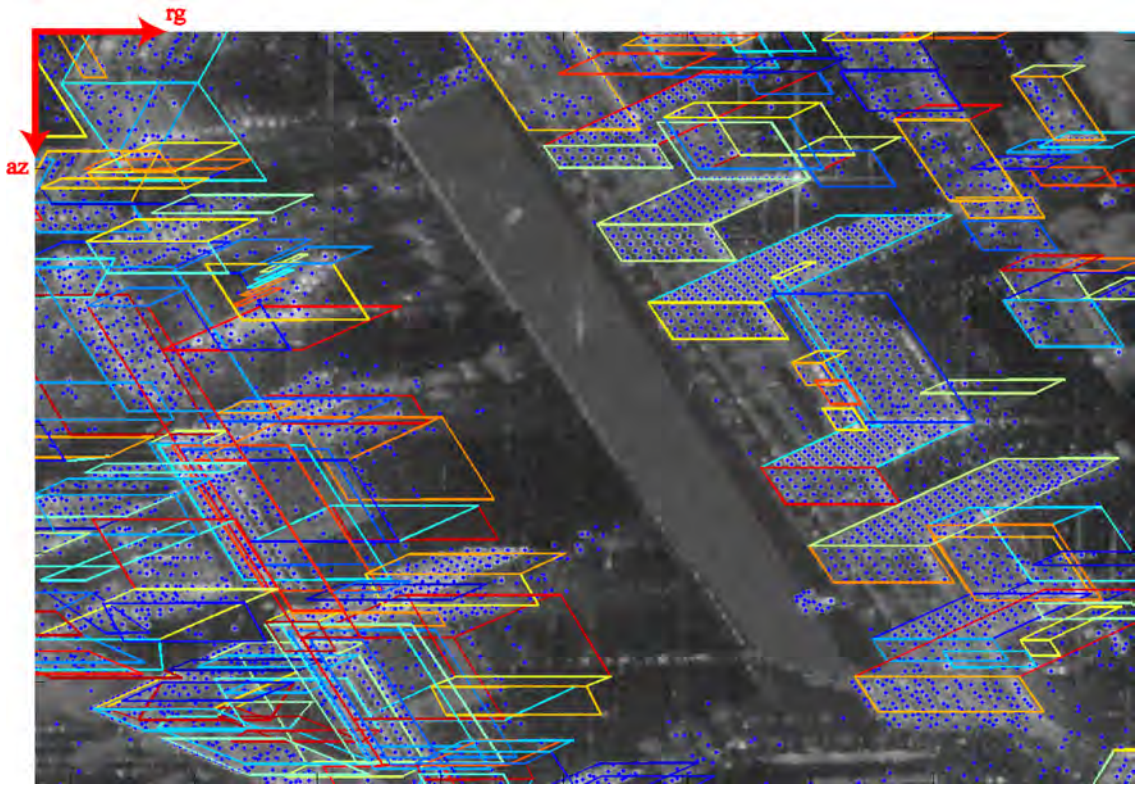

(a)

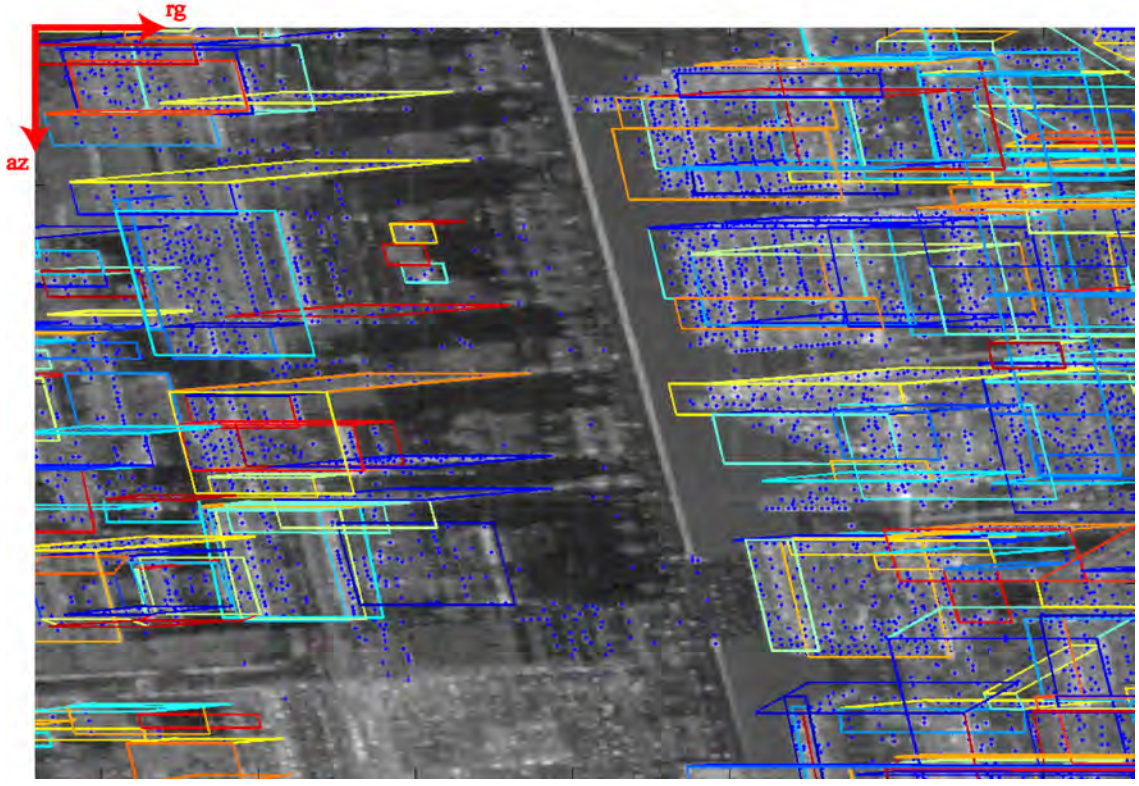

(b)

Figure 4.9.: Facades visible to the sensor for ascending (a) and the descending (b) dataset in the respective range-azimuth plane. The facades are depicted as colored parallelograms. In the background, the mean amplitude maps are shown. The blue dots represent the identified PS.

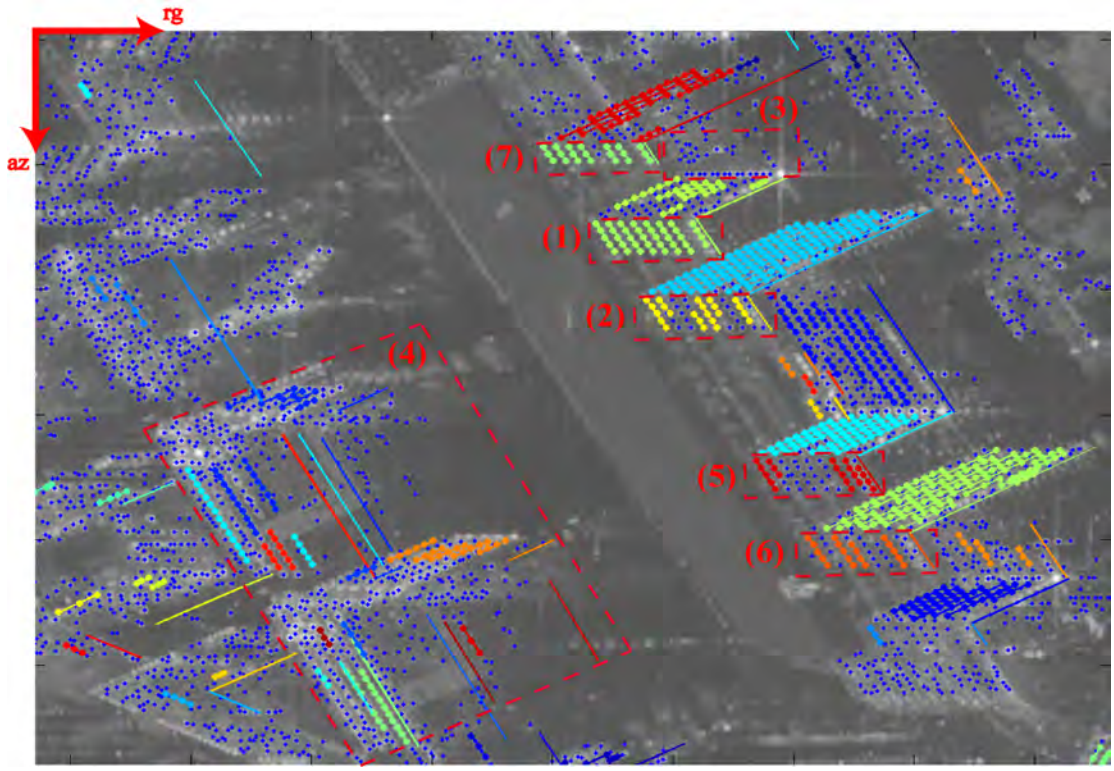

(a)

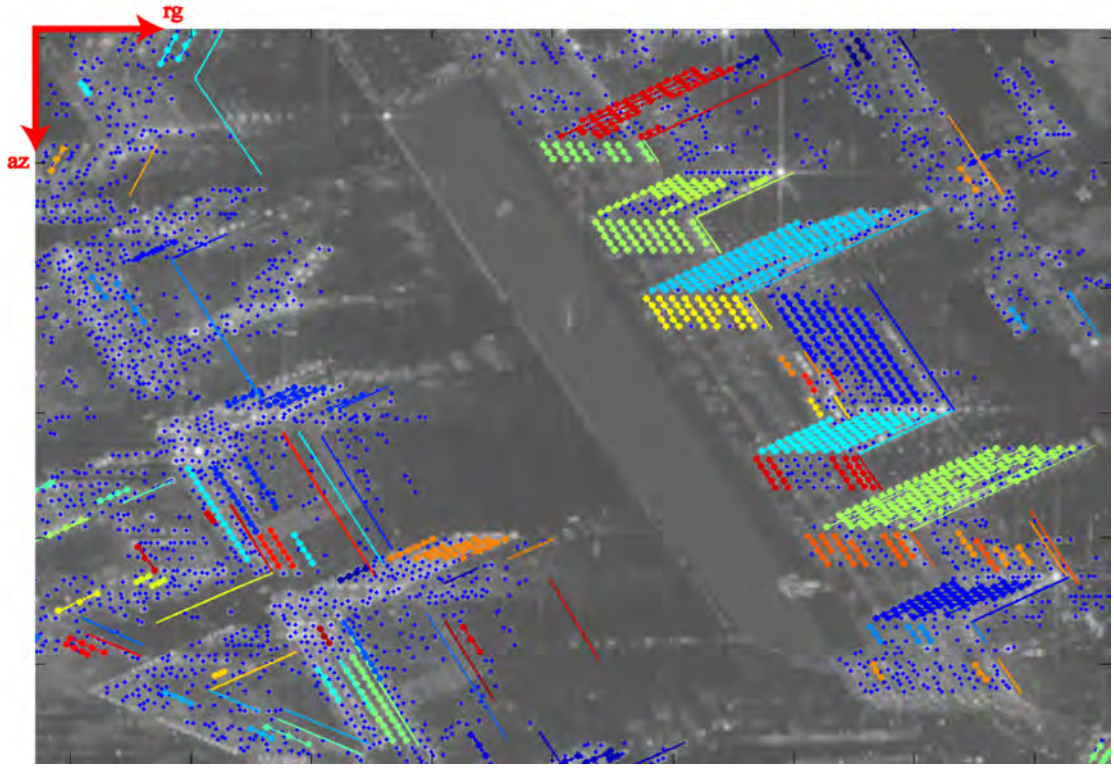

(b)

Figure 4.10.: Grouping results for the ascending dataset using $\kappa = 2$ (a) and $\kappa = 3$ (b). The outlines are shown as colored line segments. The affiliated groups are indicated by connected dots of the same color. The mean amplitude image is depicted in the background. All PS located in at least one facade footprint are illustrated as blue dots.

(1) (2) (3)

Figure 4.11.: Close-ups of the windows present at the facades marked by the frames in figure 4.10 (a). The numbers (1)-(3) correspond to the rectangles (1)-(3).

characteristic signals and PS patterns. Windows of type (1) produce a sharp point-like response, which is most likely due to a trihedral reflection mechanism, having its center in the lower left or right corner depending on the facade orientation. The dominance of such scattering mechanisms in urban areas and its importance for the PS technique has already been reported elsewhere [Auer et al., 2011b; Auer, 2011]. The resulting PS pattern is outstandingly regular. In contrast, windows of type (2) are not as dominant regarding their manifestation in the amplitude data as those of type (1). Furthermore, the scattering mechanism is not as straight-forward as for window type (1) since considerable reflection may occur at the vertical structure dividing the window or the horizontal bar close to the window sill. The patterns formed by windows of type (2) are not as regular as those formed by type (1), which is discernible from the considerable number of missed line parts (especially for $\kappa = 2$). Finally, at facade (3) which accommodates windows of type (3) no regular patterns are observable at all. From the geopositions of the PS it becomes obvious that none of them are located at the facade. Figure 4.11 reveals the reason for that: The window plane is almost aligned with the facade and the offset of the two planes is too small to serve as corner reflector. It is worth to note that the behavior of window type (3) seems to depend strongly on the aspect. The facade that is located between facades (1) and (2) (with groups colored in light green) also accommodates such windows but contains several PS that form regular patterns.

On the left side of figures 4.10 (a) and (b), considerably less groups are identified. Except for some very short lines, those groups are located at two structurally identical buildings marked by rectangle (4) (cf. lower part of figure 4.3 (b) for an oblique view optical image of those buildings). It is obvious that the PS distribution is not nearly as regular as it is at the just considered building complex. To a large extent this is, presumably, due to layover effects. In most areas the signals of two or more facades mix up, leading to incomplete or disturbed patterns. However, also the distribution of facade structures itself is more complicated (cf. figure 4.3 (b)) than the simple lattice-like arrangement of windows at the building complex on the right side. In many instances the very same arrangement of facade structures appears periodically along a facade. Each facade element can induce several PS which results in a distinct pattern of points that repeatedly appears at the facade. Obviously,

the model used in the outlined procedure (i.e. periodically appearing points) is too simple for such cases. A possible extension are shape or facade grammars, which have been applied for facade reconstruction from terrestrial photographs [Ripperda & Brenner, 2006; Riemenschneider et al., 2012].

The difference between the two grouping results ($\kappa = 2$ and $\kappa = 3$) is relatively small within the test area. Quite different results arise only at the facade marked by rectangle (2). For $\kappa = 3$, the outcome is relatively complete except for one PS missing in the third row (counting from left to right). In contrast, the result using $\kappa = 2$ shows considerably less groups.

The results obtained at facade (2) for $\kappa = 2$ as well as at facades (5) and (6) for $\kappa = 2$ and $\kappa = 3$, are surprisingly incomplete. All those facades accommodate windows of type (2). In case the stochastic model of the coordinate differences is valid and the PS are arranged in a perfectly regular lattice, the probability for finding the complete pattern should be quite high. On the other hand, the facades (1) and (7), which both accommodate windows of type (1), show complete results for $\kappa = 2$ and $\kappa = 3$. Furthermore, the three facades oriented almost along range direction and located above the facades (2), (5), and (6), respectively, contain windows of type (2). They, nevertheless, show quite complete and in particular long patterns. Obviously, the deviation from a lattice-like point distribution is stronger at facades (2), (5), and (6) than elsewhere at the building complex. Whether the point positions are less precise or their true locations deviate stronger from a perfectly regular arrangement is difficult to assess. However, the fact that the PS at those facades which show poor results are somehow related is obvious. By missing those correlations, a lot of usable information is lost. Finally, it is worth to mention in this context that the presumption of σ_α being a sensible estimate seems reasonable, as several long groups are found. Otherwise those groups would have been split into shorter segments.

Descending data

The grouping results for the descending dataset are illustrated in figure 4.12 (a) and (b) for $\kappa = 2$ and $\kappa = 3$, respectively. Similar to the left half of figure 4.10, not many groups are identified in either results. A major reason for that is layover, which becomes obvious from figure 4.9 (b). In most areas the signals from two or more facades mix. Consequently, the PS distribution appears to be mostly irregular. The areas marked by the rectangles (1)-(3) in figure 4.12 (a) are particularly interesting since they show the back side of the building complex containing many regular patterns in the ascending dataset. An oblique view aerial image of the area is depicted in the lower left half of figure 4.4 (b). The lattice-like arrangement of windows is clearly recognizable. The facades (2) and (3) in figure 4.12 contain windows of type (2), while facade (1) accommodates windows of type (1). In contrast to the results in the ascending data, the PS distribution is hardly regular, except for some small groups at facade (1) and two longer lines at facade (2) close to the outline (depicted in cyan). The irregularity in the upper part of facade (2) is surprising as no other facades interfere in this area. Most likely, the disturbance of the regular pattern is due to signals from the building

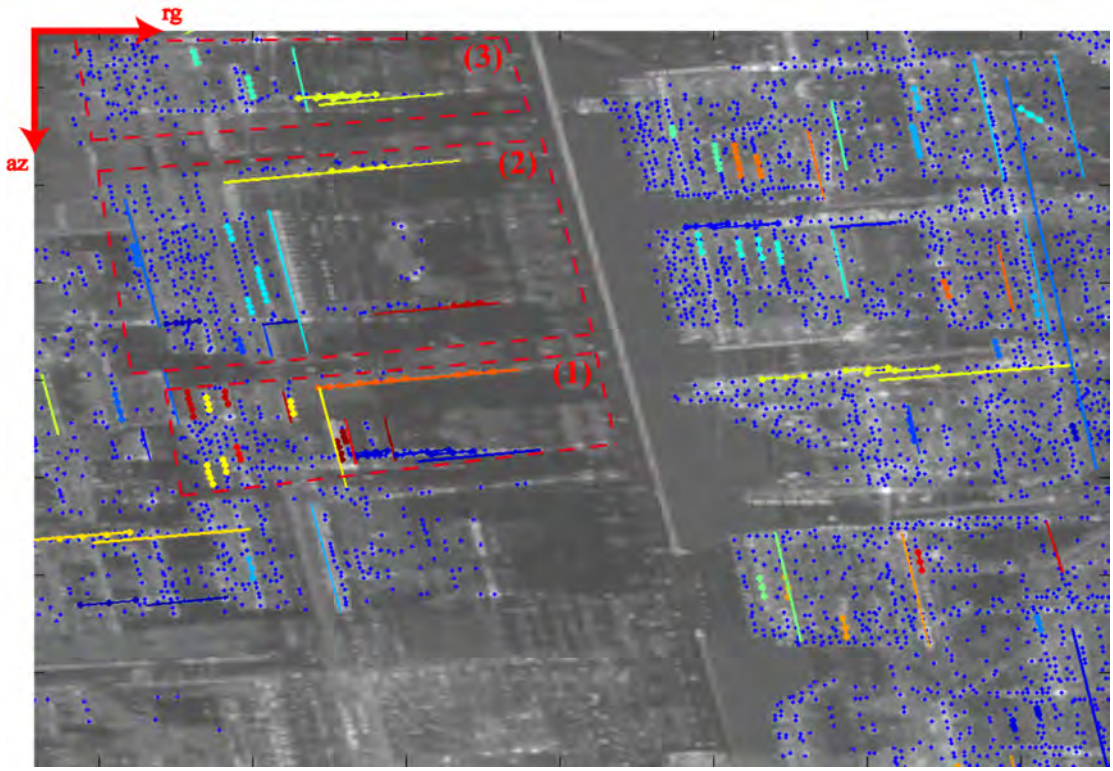

(a)

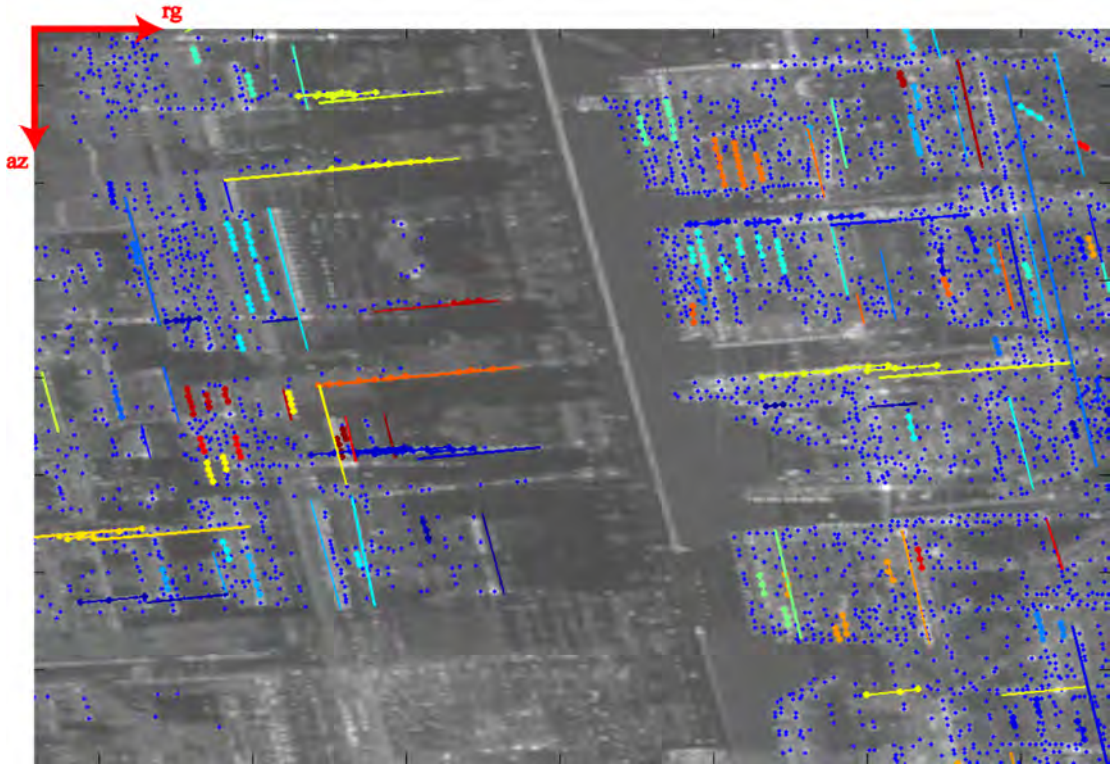

(b)

Figure 4.12.: Grouping results for the descending dataset using $\kappa = 2$ (a) and $\kappa = 3$ (b). The outlines are shown as colored line segments. The affiliated groups are indicated by connected dots in the same color. The mean amplitude image is depicted in the background. All PS located in at least one facade are illustrated as blue dots.

roof mixing with reflections from the facade. This assumption is supported by the fact that many of the PS affiliated to facade (2) are situated on the roof of this building as visible from the height indicated by the color in figure 4.4 (a). For such facades exhibiting a regular PS arrangement in some parts and an irregular distribution everywhere else, the estimation of the pattern frequencies may become a problem, because the KDE is applied to a dataset containing comparatively many random differences. That may impair the accuracy of the estimated pattern spacings giving rise to an additional error term which is not considered in the stochastic model (cf. section 3.1.2). As a result patterns are lost or only detected in parts. This may be one reason for the poor performance of the grouping procedure on the two long lines close to the outline of facade (2). Those are only partly detected (in particular for $\kappa = 2$), although both patterns appear to be fairly regular.

4.3. Alignment of PS to city model

As outlined in section 4.1, a misalignment between the two PS point clouds and the city model is expected. The main influence is presumed to be induced by the different vertical datums. Consequently, the shift in z-direction is anticipated to be much larger than in x- or y-direction. Certainly, residual errors in the fusion process lead to errors in all three dimensions, which are expected to have a maximum of about one meter. In order to work with one consistent dataset, the two PS point clouds are aggregated for the alignment. A separate alignment of the the two point clouds would only make sense if the shift between them is significant with respect to the precision of the alignment procedure. This is unrealistic due to the strong differences between the PS point clouds and the building models.

4.3.1. Parameter Settings

In order to achieve optimal results, the parameters controlling the stochastic model have to be chosen reasonably. The latter mainly consists in finding sensible values for $\sigma^2_{c_k}$ (denoting the variance of the plane parameter c of the face involved in the kth point to face correspondence) as precision estimates for the PS positions are available. Since $\sigma^2_{c_k}$ is believed to to be mostly influenced by generalization effects, it is inferred from the differences between the building models and the LIDAR data shown by the histograms in figure 4.8 (a) and (b) for roofs and facades, respectively. As facades and roofs show quite distinct behavior, different $\sigma^2_{c_k}$ are assumed. The most reasonable choice is to use the variances of the bell curves shown in figure 4.8 in red as estimates of the $\sigma^2_{c_k}$.

$$\sigma^2_{c_k,Roof} = 1.5\ m^2$$
$$\sigma^2_{c_k,Facade} = 0.6\ m^2\ .$$

The uncertainty of the PS locations in elevation is described by the a-posteriori standard deviations of the elevation estimate, obtained from the LAMBDA estimator. Histograms for both stacks are

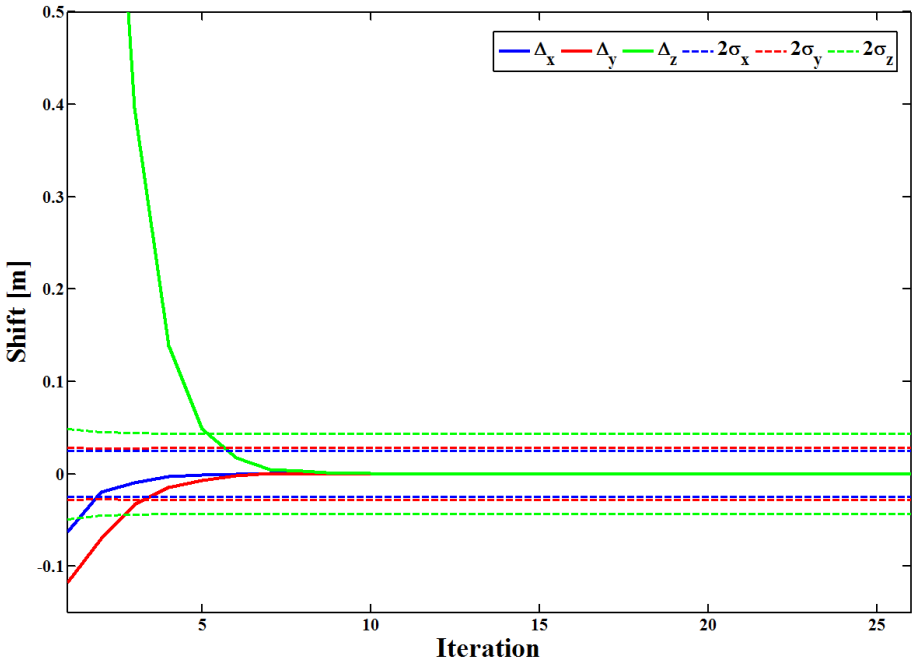

Figure 4.13.: The solid lines indicate the shifts estimated in the single iterations. The dashed lines represent the $\pm 2 \cdot \sigma$ intervals. The vertical axis is cut at 0.5 meters for presentation purposes. The iteration is converged after iteration 7.

shown in figure 4.7. In range and azimuth direction, no information per PS is available. However, since σ_r as well as σ_a are at least an order of magnitude smaller than σ_s, their influence on σ_{d_l} is negligible. Thus, the terms containing σ_r^2 and σ_a^2 in equation (3.30) are ignored. Finally, the width W_{ol} of the buffer constructed around every outline is set to two meters.

4.3.2. Results

The convergence behavior of the ICP procedure is illustrated in figure 4.13. Overall, 26 iterations are performed. The vertical axis of figure 4.13 is cut at 0.5 meters for presentation purposes. The shifts are shown as solid lines, while the dashed lines indicate the $\pm 2 \cdot \sigma_x$, $\pm 2 \cdot \sigma_y$, and $\pm 2 \cdot \sigma_z$ intervals, respectively. The error estimates are derived by variance propagation conducted in each iteration on the basis of the problem formulation given in appendix A. It is apparent that the procedure has converged after iteration seven. The final transformation can be derived by integration of the shifts displayed in figure 4.13.

$$\sum \hat{\boldsymbol{\Delta}}^T = \begin{bmatrix} -0.1 & -0.2 & 3.6 \end{bmatrix} \; [m]$$

As expected the main misalignment is present in vertical direction due to different height references. The determined horizontal shifts are relatively small. The accuracy of the alignment is assessed in the following section dealing with the assignment of PS to buildings. The estimates of the standard deviation do not change much from iteration to iteration. Only σ_z decreases slightly after the first iteration due to the alignment in z-direction. The precision of the shift in vertical direction is

roughly a factor of two worse than in horizontal direction. The reason for that may be the smaller number of PS corresponding to horizontal building faces. Compared to the order of magnitude of generalization effects or the dispersion of the PS positions in elevation direction, the imprecision of the shift seems to be negligible.

4.4. Assignment of Persistent Scatterers to buildings

In this section experiments dealing with the assignment of PS to buildings are treated. The discussion is subdivided into two main parts. Firstly, the affiliation of PS to building models is considered. Secondly, relations between facade structures discernible in the LIDAR data and horizontal groups of PS (cf. section 4.2) are addressed. Since the location of a PS in the range-azimuth grid is ambiguous with respect to the real world (due to layover), all investigations are conducted using the geocoded point clouds. Finally, the established relations between PS and building faces are used to compile a density map which reveals the number of PS per unit area building surface. Such map is of major practical importance as it shows if the sampling is sufficient for monitoring applications. Besides this practical importance, such map is useful to identify some of the driving factors influencing the PS density which constitutes the main part of this final section.

4.4.1. Matching of Persistent Scatterers to building model faces

The affiliation of PS to building models is conducted according to section 3.3. For this investigation the buffer widths W_{ol} and w_{pl} are set to two and one meter, respectively. Since the former threshold only controls the exclusion of PS that are far from buildings, it is set to a rather big value compared to the PS positioning accuracy. The second threshold is chosen to be on the order of the maximum elevation standard deviation occurring in the PS sets (cf. figure 4.7), to remove the majority of the assignments where the perpendicular projection of the PS onto the building face is located too far away from the polygon associated with the building face. The threshold on the normalized distance is chosen to be three which corresponds to a confidence level of 99.5% given that the distribution assumption (i.e. standard normal distribution) holds. The study focuses on one main question: How reliable is such an assignment using the available datasets and the outlined assignment procedure? As mentioned in section 4.1.1 (cf. figure 4.1 and figure 4.6) a correlation between the PS point clouds and building outlines is recognizable. However, several issues have to be considered when PS are assigned pointwise (i.e. the single assignments are independent of each other) to building faces of a generalized city model based on a purely geometric criterion. Two problems are of major importance. Firstly, a PS may be related to some structure at a building, but this structure is not properly represented in the building model. Such cases may occur due to generalization or deviations of the phase center of a PS from the actual (i.e. not generalized) building surface. Secondly, closeness of PS to a building does not necessarily imply a relation. In section 4.1.1 virtual corners are discussed. Those are constituted by unrelated surfaces forming a section of a trihedral

reflector. The phase centers of the resulting PS have no real world correspondence but may happen to be located close to buildings.

The area considered for the following study coincides with the test site addressed in section 4.2.2 (cf. figure 4.9). In figure 4.14 the resulting assignment of PS to buildings for this test site is illustrated. The building models are indicated by the thin black lines. The point colors represent the affiliation to buildings. All points shown in brown color, are unassigned[5]. At first glance, the many PS which are located almost exactly at the facades strike the eye. This suggests that both datasets are in good alignment in x- and y-direction. Since the precision of the PS position estimates is high compared to the typical spacing between buildings, an assignment as shown in figure 4.14 is unproblematic in most cases.

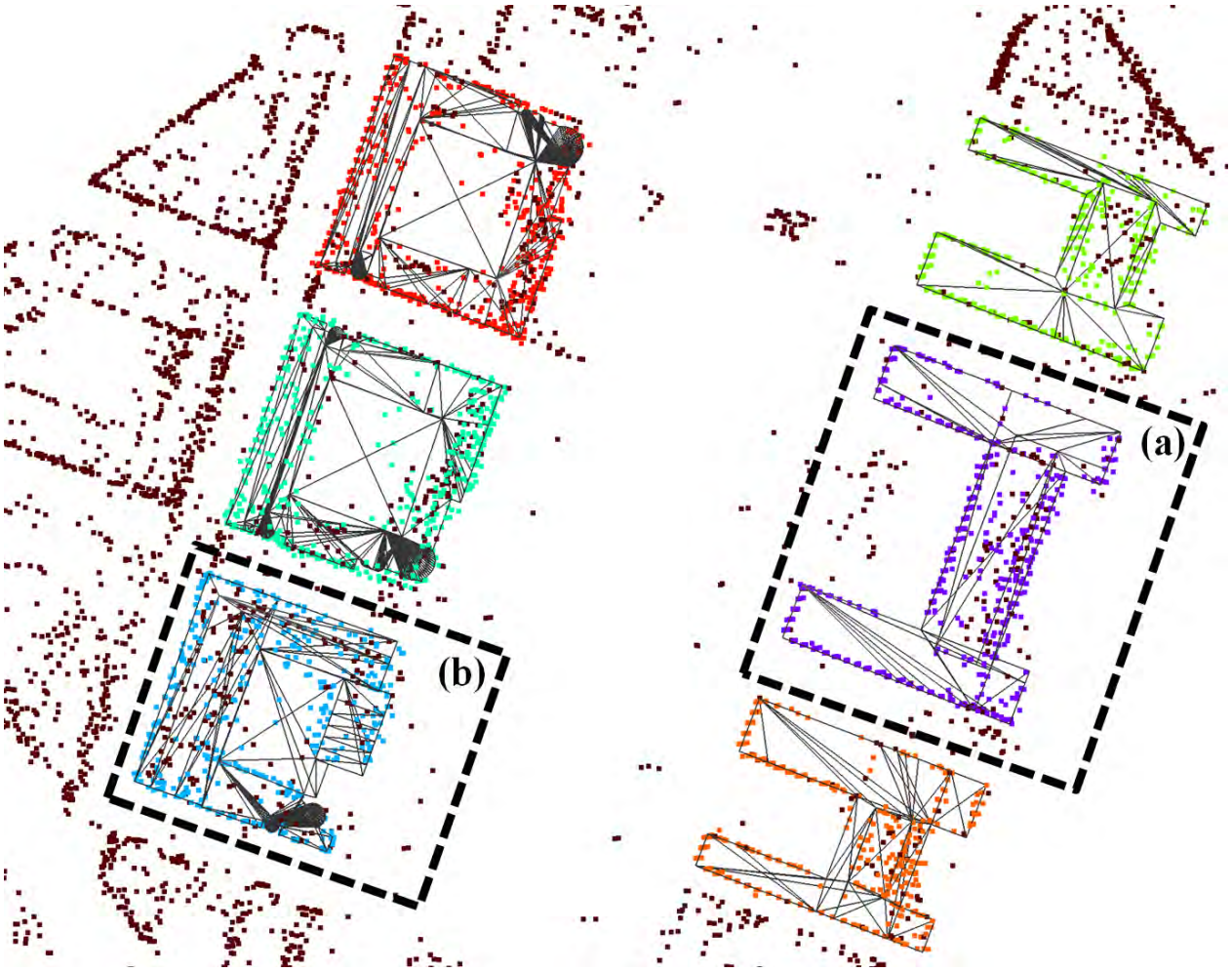

Figure 4.14.: Assignment of PS to buildings. The colors indicate the determined relations. Dark brown PS are unassigned. The used building models are shown as thin black lines.

However, inside the outlines of each of the six shown building models a couple of PS remain unassigned. This is due to the fact that their normalized distances to any bounding surface are

[5]For this study only the shown building models are used. The PS in the left half relate to building models which are not considered here

above the threshold. Such points are actually located in the inside of the respective building models which hints to one of the two issues outlined above (unrelated PS close to a building or PS that are not properly represented by the building model). Some of those PS are examined in more detail in the following case studies.

For further investigation, the two buildings framed by the rectangles (a) and (b) are inspected in detail. The assignment of PS to building faces is demonstrated for (a). Furthermore, the problem with PS which are close to a building model but are potentially unrelated is discussed. Generalization issues are addressed by means of building (b).

Case study (a)

The PS assigned to the vertical and the horizontal faces of building (a) are shown separately in figure 4.15 (a) and (b), respectively. The red arrow in (a) displays the viewing direction in (b). Black lines connecting the points to the building faces indicate the affiliation. An oblique view aerial image (© Microsoft Bing™Maps) of the building is depicted in figure 4.16. Some of the facades have already been discussed in section 4.2. The building exhibits a lattice-like distribution of windows which are likely to induce a large portion of the facade PS. Along the facades the PS compare well with the map data. Small systematic effects are only visible at the facades (f1) and (f2) (the PS are slightly left of the model face). The reason for this behavior is most likely generalization. However, also deviations of the PS phase centers from the actual building surfaces are a possibility. The dispersion around the building faces (f3) to (f6) is much stronger than at the other facades. This is surprising since all facades feature a similar setup. It is noticeable that most PS located at facades oriented horizontally in figure 4.15 (a) show a larger deviation than the facades oriented vertically. However, the PS at the two horizontally aligned facades at the bottom of figure 4.15 (a) exhibit a low dispersion. Furthermore, it is important to stress that the PS at the facades (f4) to (f6) result from the descending b042 datastack while the PS at the facades (f1) to (f3) result from the ascending b057 datastack. Thus, the orientations of the horizontally oriented facades (f4) to (f6) on the one hand and (f3) on the other hand with respect to the LoS of the sensor are different. Given those observations, it is hard to assess if the dispersion of those PS is related to different facade orientations. In general, the investigation of PS behavior as a function of acquisition parameters (e.g. the relative orientation between building face and LoS of the sensor) is difficult because the reflection mechanisms inducing the PS are unknown in the majority of the cases. This makes the formation of groups of comparable PS very difficult.

In contrast, PS and building model do not compare well at the horizontal faces (see figure 4.15). At first glance, the deviation of the points from the modeled surface is much larger than at the facades. Furthermore, the points tend to be located rather underneath the modeled surface. The opposite (i.e. points above the surface) could be explained by superstructures not contained in the reference data, such as antennas. For comparison and to exclude generalization effects, the centerline of the LIDAR data is depicted as dashed red line. Surprisingly, a considerable number of LIDAR

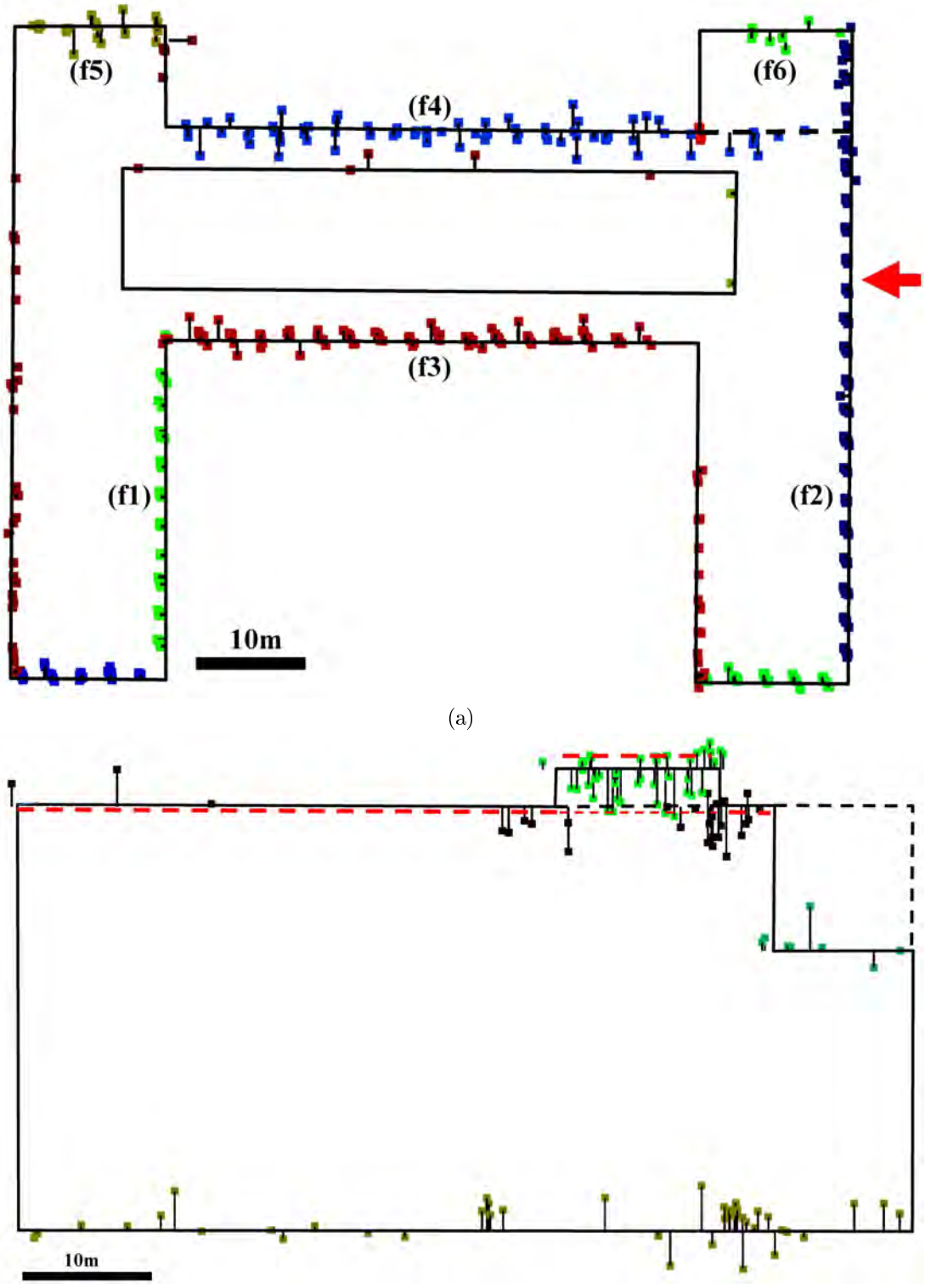

Figure 4.15.: (a) PS assigned to the facades. (b) PS assigned to the horizontal bounding surfaces. The red arrow in (a) indicates the viewing direction in (b). The point colors and the black lines connecting the PS to the building faces show the affiliation. The red dashed line in (b) depicts the building surface as discernible in the LIDAR data. Note that a considerable number of LIDAR points are located underneath the roof superstructure, which is indicated by the thin red line.

Figure 4.16.: Oblique view aerial image of the building addressed in figure 4.15 (© Microsoft Bing™ Maps).

points are situated underneath the roof superstructure (indicated by the thin red line). The reason for this effect and the reliability of the corresponding data are unknown. However, it fairly well explains the distribution of the PS shown in light green. Still, also the PS attributed to the main roof plane (indicated by the black points) are, except for a few PS, located underneath the modeled surface. It is very questionable if such points are related to the building roof. Similarly, some PS are attributed to the bottom surface of the building (beige points). Although many of them are located close to one of the facades and may, thus, be mismatches, some are located right in the inside of the building. Such PS may, of course, be induced by structures within the building. However, a corresponding signal path that persists over a longer time span is hard to imagine.

In figure 4.17 the unassigned PS located inside building (a) and those PS with large normalized distance (i.e. 2.5 to 3) are displayed as red and green points, respectively. Figure 4.17 (a) and (b) show the building as top- and side-view (analogue to figure 4.15 (a) and (b)), respectively. Surprisingly, few PS exhibit a normalized standard deviation between 2.5 and 3. The most noticeable feature of figure 4.17 is the large number of unassigned PS located inside the building. In contrast to the already addressed cases where such points are allocated to one of the faces, many of the PS are situated far from any bounding surface. Furthermore, those points do not seem to be distributed completely arbitrarily. As visible from figure 4.17 (a) the points are concentrated in the central part of the building. Figure 4.17 (b) proofs that the majority of them is situated in the upper half of the building.

Considering the large number of PS inside the addressed building, the question if there is any relation between the two arises. As argued above points in the inside would require a signal path within the building or some of the bounding surfaces to be transparent to the RADAR wave. While

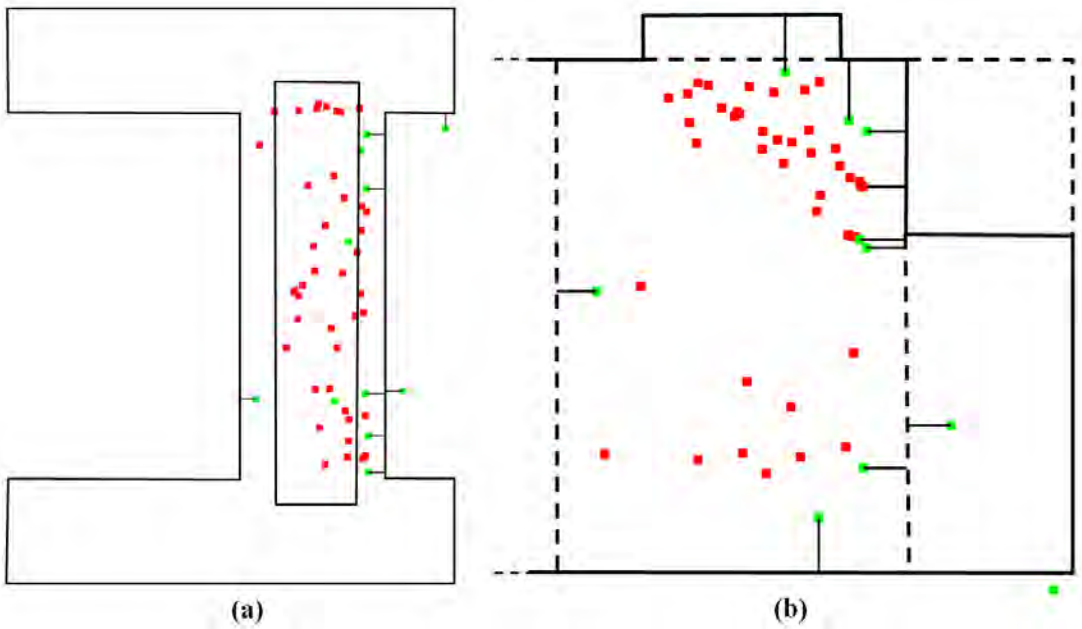

Figure 4.17.: Unassigned PS and PS with large normalized distance (i.e. 2.5 to 3) shown as green and red points, respectively. (a) depicts a topview, while (b) shows the scene as side view.

the former is conceivable in a few isolated cases, the latter appears to be completely unrealistic. Alternatively, the PS could be induced by virtual corner reflectors or similar mechanisms. In this case, the proximity is basically random. However, the large number and distribution of those PS would suggest those reflectors to be related. A closer examination of this issue is subject to future work.

Case study (b)

The situation for case study (b) is displayed in figure 4.18. An oblique view aerial image is displayed in figure 4.18 (c). The following study focuses on the building part marked by the red polygon. The side view shown in figure 4.18 (a) illustrates the scene from the perspective indicated by the red arrow in (c). In (a) all PS that are attributed to the building with large normalized distance (i.e. between 2.5 and 3) and unrelated PS are shown. The former are displayed in green, while the latter are displayed in red. The established assignments are shown as black lines connecting the PS with the building model. Finally, the surface visible from the LIDAR point cloud is depicted as blue dashed line. In between there is a gap where no LIDAR points are available. This part coincides with the image section marked by the green polygon in (c). In the optical data, four indentations are visible. The rest of the area seems to contain windows. However, this is not clearly recognizable due to the relatively low resolution of the aerial image. The kink in the lower left of the LIDAR surface is caused by the roof of a shopping mall in front of the considered building.

The region framed by rectangle r1 perfectly illustrates the effects of generalization. By comparing the LIDAR surface with the building model, it becomes obvious that the modeled roof is several

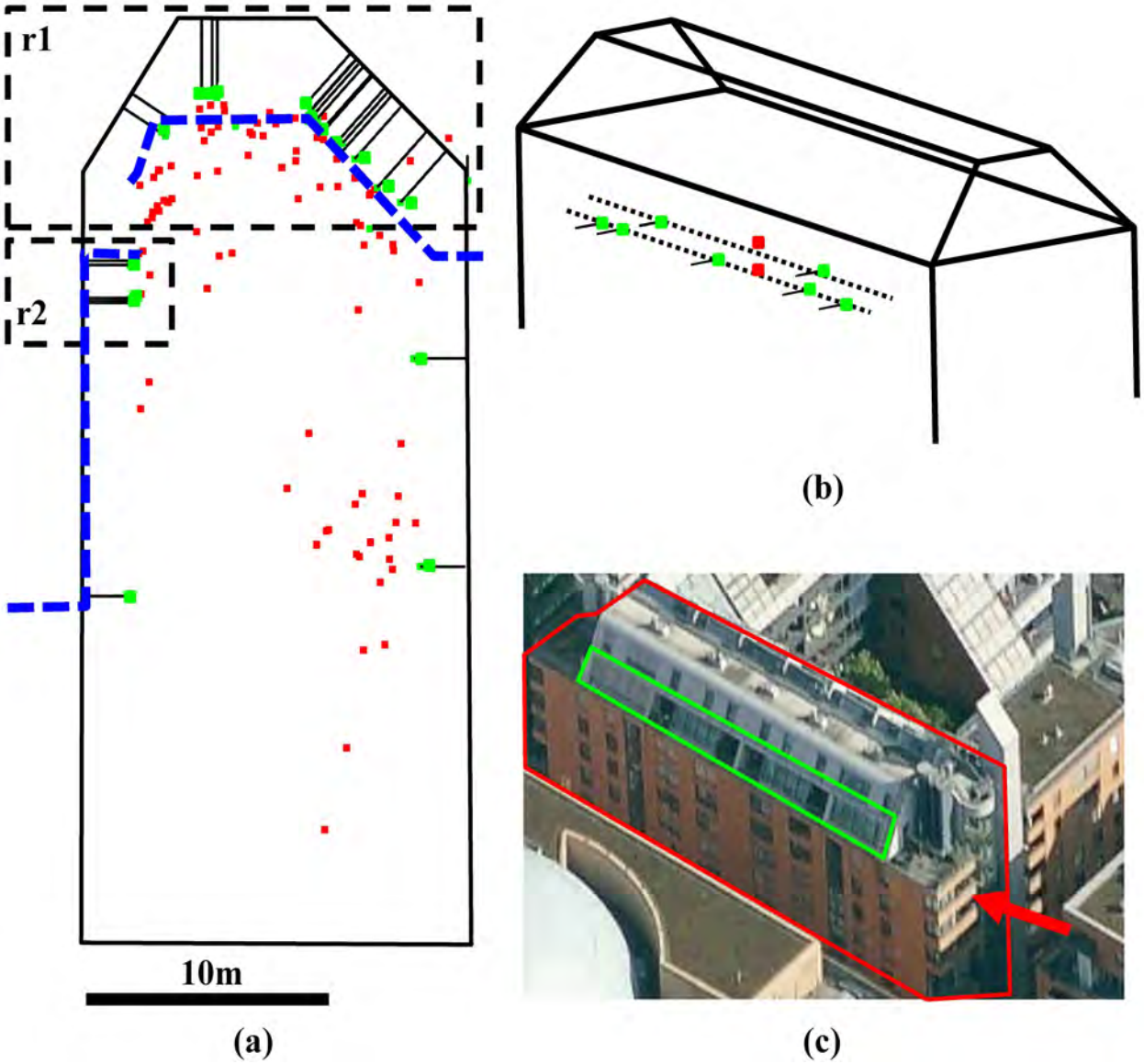

Figure 4.18.: (a) Side view of the building part marked in (c) by the red rectangle. The red arrow in (c) marks the viewing direction in (a). Green and red points depict the attributed and unassigned PS, respectively. The black lines show the affiliation of the PS to the faces of the building model. The building surface as discernible in the LIDAR data is displayed by the dashed blue line. The rectangles r1 and r2 distinguish the areas discussed in more detail. (b) The facade of the investigated building together with the PS relevant for area r2 are shown. The dashed lines signify PS located approximately at the same height. (c) Oblique view aerial image of the investigated building (© Microsoft Bing™ Maps).

meters above the actual one. The PS compare much better with the LIDAR data. However, similar to the assignment to the roofs presented in figure 4.15 (b), the dispersion of the PS around the reference is quite large. This makes a definite statement on the validity of the alignment in z-direction difficult. Those PS whose estimated positions are above the blue line, happen to be related to one of the building faces. All other PS remain unassigned. Such strong generalization effects are mainly encountered for building roofs since they generally exhibit more complex shapes than frontages. However, large facade structures such as balconies may also lead to strong generalization effects.

Contrary to r1 rectangle r2 marks a section of the building facade. Two rows of PS with almost equal distance (approximately two meters) to the building facade are visible. The situation is shown from a different perspective in figure 4.18 (b). The dashed lines indicate the vertical locations of the two rows consisting of three (the uppermost row) and six PS, respectively, including the two unassigned PS. From figure 4.18 (a) it is obvious that the uppermost row coincides with the edge of the LIDAR surface. Those PS may be related to the four indentations present in the area encircled by the green polygon in figure 4.18 (c). This would imply that the PS at the second indentation from the left is missing. The deviation of the bottom row from the facade is, however, peculiar. At this location, the modeled facade and the LIDAR data are in good correspondence suggesting generalization effects to be negligible. Two explanations are possible. Firstly, the phase centers of the PS are located inside the building. In case the area indicated by the green rectangle in (c) contains windows, the radar signal could enter the building and be reflected at some structure in the inside. Alternatively, the PS are not related to the building at all. However, this would raise the question why those PS are arranged so regularly.

4.4.2. Assignment to facade details

In this section horizontal facade structures discernible in the LIDAR point cloud are related to groups of PS. The aim of this study is to investigate the physical nature of PS by geometric comparison with the horizontal LIDAR patterns, which are in turn related to real world structures. Approaching the assignment of PS to facade details in this indirect way is easier since it is much more intuitive to assign LIDAR data to real world structures than PS.

The LIDAR points forming those horizontal structures are extracted manually. In order to estimate the vertical location of each LIDAR pattern, the mean height of the correponding LIDAR points is calculated. To remove the PS that are not relevant for this study and to enhance the location precision of the remaining points, the grouping information is used. Only the results obtained for the ascending dataset using $\kappa = 3$ are employed (cf. figure 4.10 (a)). The investigation focuses on two buildings, referred to as (b1) and (b2), respectively. Those buildings are chosen because of their simple facade design. Both are depicted in the oblique view aerial image shown in figure 4.19. Building (b1) has already been discussed in section 4.4.1 (cf. Case study (a)). Since the windows are the only salient features at the facades of both buildings and one horizontal row is visible per floor (the vertical distance between consecutive rows is constant), a relation of the LIDAR patterns to

the windows is very likely. Closeups of the occurring window designs are presented in figure 4.11 in section 4.2.2. At building (b1), only windows of type (2) appear, while building (b2) accommodates windows of type (1) and (3). Sort (1) appears at the red brick stone facades, type (2) occurs at the light sand stone frontages (i.e. all facades facing the inner yard). The window designs (1) and (2) feature broad window sills, which are presumed to be the cause for the horizontal LIDAR patterns at the corresponding facades. This presumption is reasonable as the patterns have a very small extent in vertical direction implying the reflection at a horizontal structure.

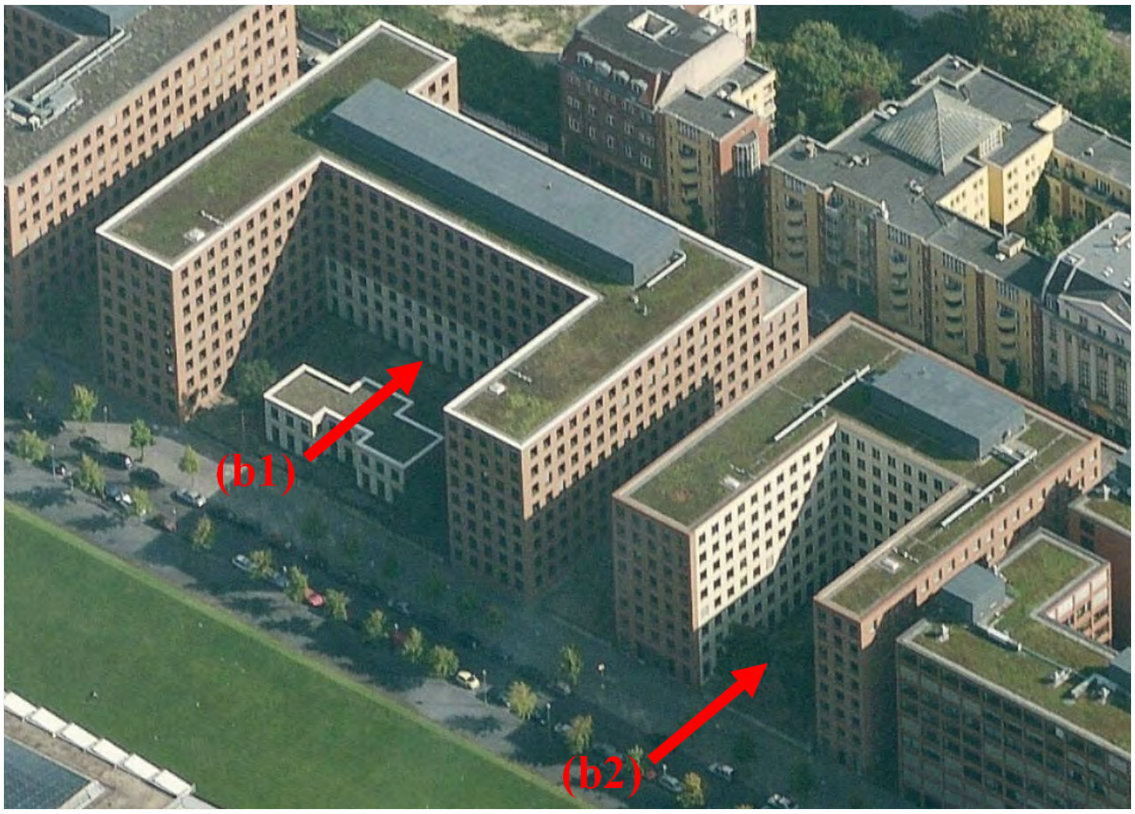

Figure 4.19.: Oblique view aerial image (© Microsoft Bing™Maps) of the two buildings analyzed in figure 4.20. The red arrows indicate the viewing direction used in the latter depiction.

The comparison of the grouped PS with the facade structures present in the LIDAR data are shown in figure 4.20 (a) and (b) for the buildings (b1) and (b2), respectively. Both images exhibit the same scale. The viewing direction is represented by the red arrows in figure 4.19. The relevant bounding surfaces of the 3D models are depicted as bold and dashed black lines. Along the facades of either building, the LIDAR data are arranged along horizontal rows. Those are indicated by the dotted lines and the black rectangles. The latter mark the location and extension of the LIDAR patterns at facades extending into the image plane. Finally, the grouped PS are illustrated as red squares. Potential relations between the PS and the windows have already been discussed in section 4.2.2. At both buildings the correlation between PS and LIDAR is clearly visible. However, at building (b1) the PS are located systematically above the LIDAR data. In contrast, both datsets seem to match quite well at (b2). In order to quantify potential systematic effects, the vertical

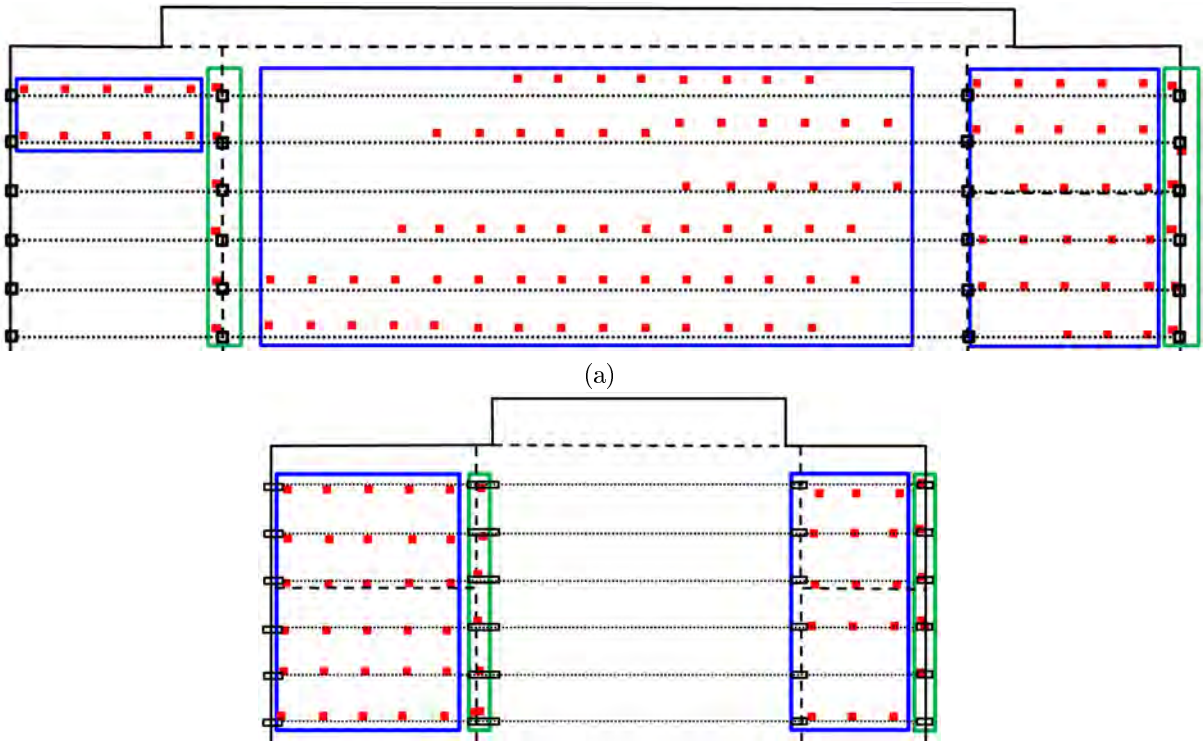

(a)

(b)

Figure 4.20.: Comparison of the grouped PS with the facade structures present in the LIDAR data for the buildings (b1) in (a) and (b2) in (b). Either image exhibits the same scale. The viewing direction is represented by the red arrows in figure 4.19. Bold and dashed black lines depict the relevant faces of the building models. The LIDAR patterns are indicated as dotted lines and black rectangles. The latter mark location and extension of the LIDAR structures extending into the image plane. The grouped PS are depicted as red points. The colored rectangles illustrate the affiliation of the encircled PS to front or side facades (cf. table 4.3).

distance between both datasets is evaluated. Since the location of the PS phase centers may depend on the orientation of the target with respect to the sensors viewing direction, only groups at facades of equal orientation are evaluated jointly. At either building, two different orientations occur: fronto-parallel and perpendicular to the image plane. The corresponding groups are encompassed by blue and green rectangles, respectively. As the left and right facade perpendicular to the image plane at building (b2) accommodate different window types, they are also assessed separately. For the investigation, the mean vertical offsets between the PS patterns and the LIDAR data are determined. Each group height is weighted by the number of comprised PS. The results are reported together with the corresponding standard deviations $\sigma_{\overline{\Delta}}$ in table 4.3. The latter are estimated on the basis of the expected dispersion of the group height (cf. equation (3.21)) using the law of variance propagation. The standard deviation of the vertical locations of the LIDAR patterns is fixed to four centimeters. This figure is inferred from the standard deviation of the vertical row spacing (i.e. from the standard deviation of the z-differences). The two occurring orientations are referred to as Front and Side corresponding to the fronto-parallel facades (blue rectangles) and the frontages perpendicular to the image plane (green rectangles). At building (b1) a clear offset between the

	(b1)		(b2)		
	Front	Side	Front	Side left	Side right
$\overline{\Delta}$	71 cm	48 cm	-7 cm	25 cm	22 cm
$\sigma_{\overline{\Delta}}$	5.3 cm	4.9 cm	6.6 cm	7.1 cm	6.3 cm

Table 4.3.: Mean vertical distances and corresponding error estimates for PS groups located at fronto-parallel facades (Front) and frontages perpendicular to the image plane (Side). Those are marked by blue and green rectangles in figure 4.20, respectively.

LIDAR and the PS patterns is measurable. This is expected since PS related to windows of type (2) are unlikely to be located directly at the window sill. The latter is due to possible reflections at the vertical structure dividing the window and the horizontal bar close to the window sill. It is worth to mention that the reflection mechanism inducing the PS seems to be slightly aspect dependent leading to different $\overline{\Delta}$ for front and side. This is plausible due to the complex design of windows of sort (2). At building (b2) the facades front and side right contain windows of type (1). They are anticipated to act as a trihedral reflector, having its phase center in the lower left or right corner depending on the facade orientation. This implies that $\overline{\Delta}$ for the facades front and side right should be close to zero. This can be verified for the front facade, where, a small $\overline{\Delta}$ is observed. However, the facade side right exhibits a significant $\overline{\Delta}$, which is not expected given the assumed reflection mechanism. Furthermore, the estimated offsets for the facades side left and side right are very similar although the corresponding window designs ((3) and (1) respectively) are quite different. Assumptions about the reflection mechanism leading to PS at windows of type (3) remain very speculative, as the the windows structure in the inside of the building is unknown. However, the fact that horizontal LIDAR patterns occur suggests the presence of a horizontal plane in the inside of the building (e.g. a window sill). In case such horizontal structure in the inside exists, the case is similar to the facade side right. The estimated $\overline{\Delta}$ does not support a relation between the PS and this structure.

Of course, some issues have to be kept in mind when interpreting the results presented in figure 4.20 and table 4.3. Firstly, the comparison is conducted under the assumption that the misalignment in vertical direction has been completely removed (cf. section 4.3). The estimate of the shift in the vertical is expected to be less reliable than in x- and y-direction. This is due to generalization effects, which are much stronger for the roofs than for the facades. As already outlined the quality of the registration in z-direction is hard to verify. Thus, a remaining misregistration in the vertical in the order of a few decimeter cannot be excluded. This has to be considered when interpreting the results for building (b2) Side left and right.

Furthermore, it is assumed that the accuracy of the determined group height is well below one decimeter. For this assumption to hold two requirements have to be fulfilled. Firstly, all PS contained in a group have to exhibit the same height and, secondly, the weights utilized in the estimation process (cf. equations (3.17) and (3.18)) have to be reliable. The former condition may be violated in case false positives are included in the groups or if the PS along a floor feature different heights. The latter is elusive as only the readily processed point clouds are available within this study. It is

worth to note that, if the precision measures of the PS are incorrect, not only the estimated offsets $\overline{\Delta}$ but also the respective standard deviations $\sigma_{\overline{\Delta}}$ become inaccurate (equation (3.21) involves the PS accuracy estimates). The latter are very important for the discussion outlined above as they allow to assess the significance of the estimated offsets.

An example for an erroneous group height estimation is recognizable at the very right facade of building (b1). The second row from the top is located underneath the corresponding LIDAR row and is approximately aligned with the face of the building model. In contrast, all other comparable groups (i.e. those groups framed by the green rectangles) are situated slightly left of the models bounding surface and above the LIDAR patterns. It is worth to note that an erroneously estimated group height also impairs the quality of the planimetric position since the group height is used to improve the PS positions (cf. section 3.1.4). The reason for the strong deviation of this group is not known. Certainly, it is too large to be explained by random errors (the group contains 16 PS). A closer inspection of the result suggests that the determined grouping information is correct. In case this pattern is left out of the determination of $\overline{\Delta}$ ((b1) Side), the figure changes from 48 to 59 centimeters. This would, in turn, render the difference between Front and Side hardly significant.

4.4.3. Density Map

From the assignment of the PS to the faces of the building models a density map is compiled (cf. section 4.4.1). It is shown for the ascending and the descending PS results in figure 4.21 (a) and (b), respectively. The viewing directions roughly correspond to the LoS of the respective data stacks. The colors of the bounding surfaces illustrate the density. For both results the same colorscale is used which is depicted in figure 4.21 (b) in the upper right corner. For displaying purposes values above 0.1 PS per square meter are clipped. It is apparent that hardly any building contains no PS at all. One of such few cases is discussed below (case study (5)). However, there are lots of sparsely populated faces. This is especially true for building roofs. Most exhibit densities below 0.05 PS per square meter (i.e. colors ranging from black to light blue). The majority of the facades exhibits a medium density ranging from 0.04 to 0.06 (light blue to green). However, there is also a noticeable number of frontages which feature quite low values (i.e. below 0.02 PS per square meter). The results for the ascending and the descending datasets do not show a significantly different behavior. Mean value (μ) and standard deviation (σ) of the determined PS densities are reported separately for roofs and facades in table 4.4. The low mean values for facades may be surprising at first glance. The reason for that is the considerable number of facades which exhibit PS densities below 0.02 PS per square meter. The other figures support the already outlined observations. Cumulative histograms for the ascending and the descending dataset are shown in figure D.1 and figure D.2, respectively. In the following, the main factors driving the PS density are discussed using case studies (1)-(5), marked by the white dashed rectangles in figure 4.21. Those factors comprise: surface structure (1)-(2), shadowing (3), aspect dependency (4), and quasi-random influences (5).

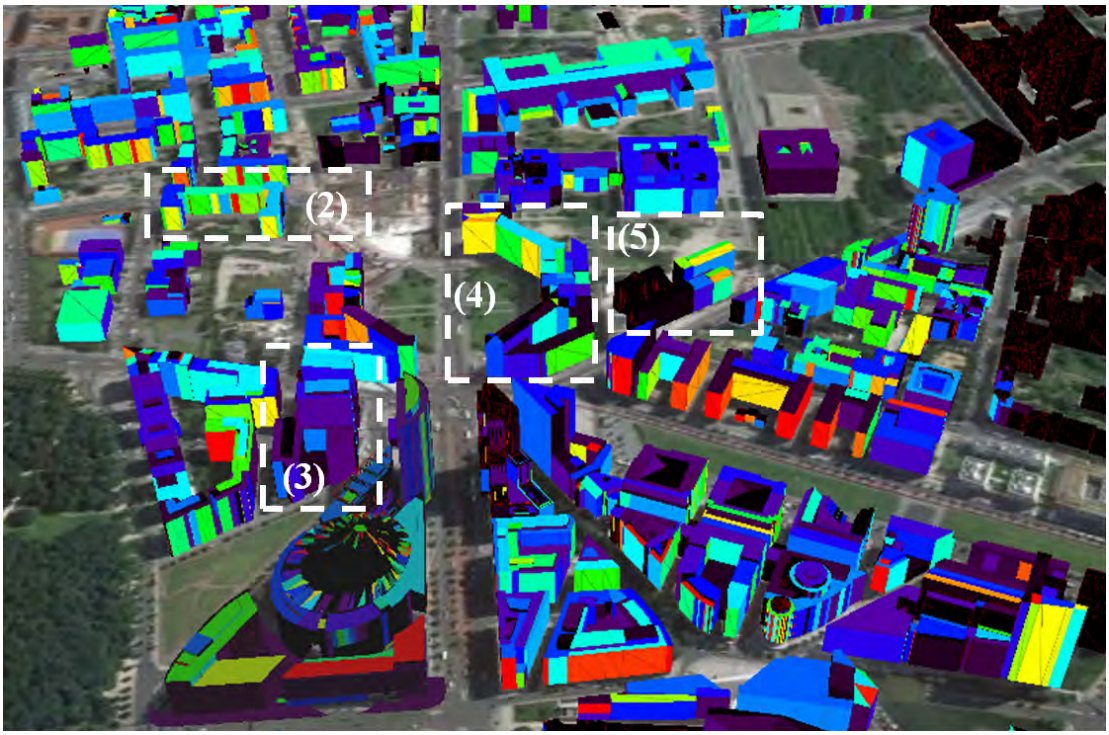

(a)

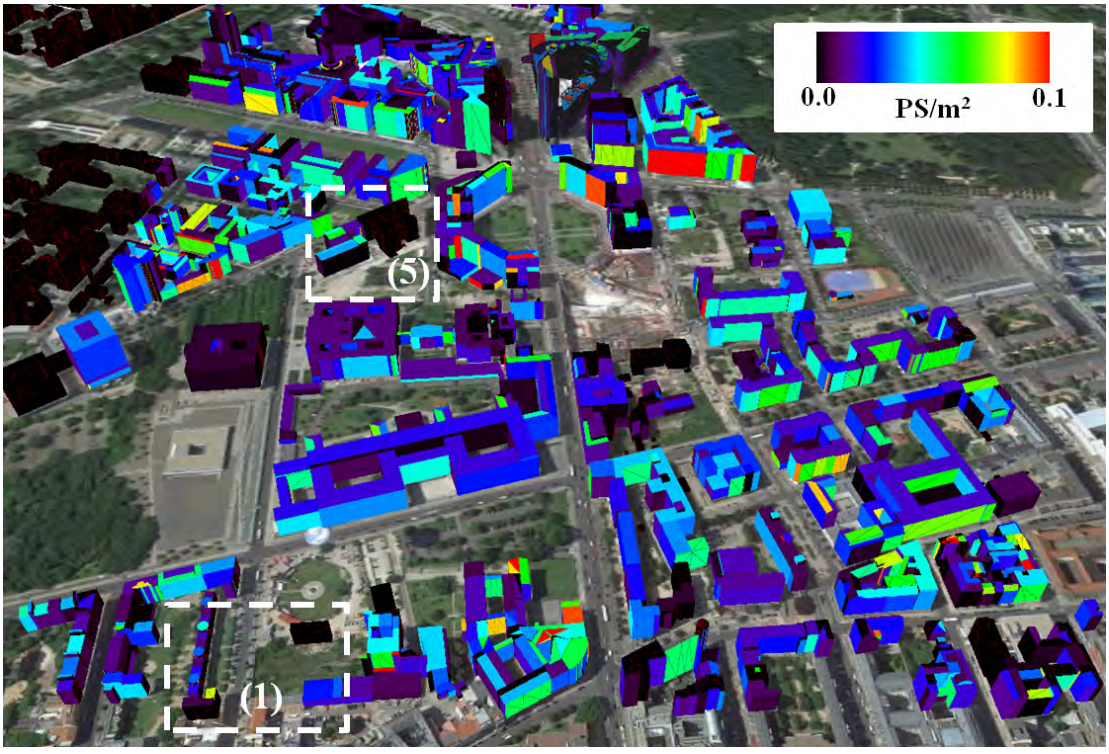

(b)

Figure 4.21.: Map of PS density for the ascending (a) and the descending (b) dataset. The viewing direction roughly correspond to the LoS of the respective data stacks. The colorscales used in (a) and (b) are equal. For displaying purposes values above 0.1 PS per square meter are clipped. The numbered rectangles mark the case studies presented in the following.

	Facade		Roof	
Stack	μ	σ	μ	σ
b057	0.033	0.020	0.021	0.021
b042	0.030	0.021	0.022	0.022

Table 4.4.: Mean values and standard deviations of the PS densities for both data stacks separately for facades and roofs.

Surface structure

PS are often induced by small structures located at facades or roofs. In the preceding sections, examples that show the connection of PS to windows have been presented. Of course, any structure that induces a strong reflection which is stable over time is likely to cause a PS. As shown in Auer [2011] many point targets can be attributed to three- and five-fold reflection mechanisms. In comparison, direct and double-bounce reflections are quite weak. Thus, a large number of facade or roof details is required for high point densities. Whether a structure, finally, induces a PS depends, of course, on its shape.

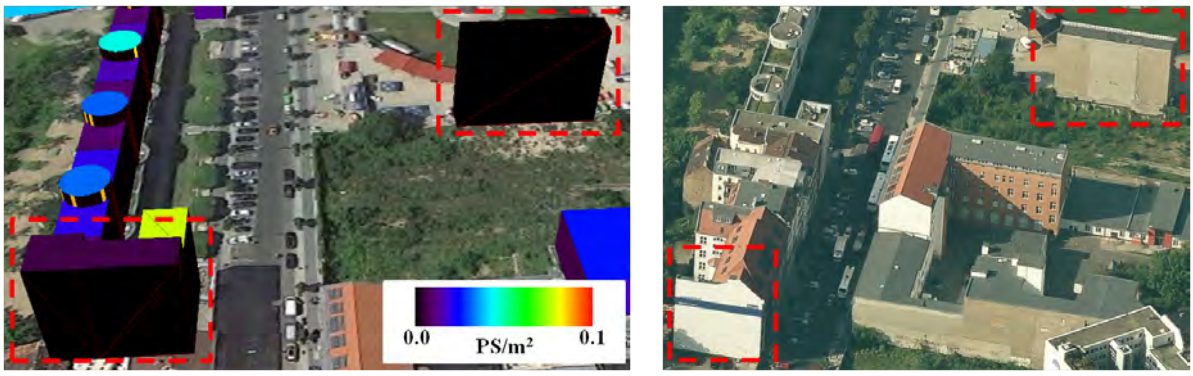

(a) (b)

Figure 4.22.: Dependence of the PS density on the surface structure. (a) Density map of the descending PS result. (b) Corresponding oblique view aerial image (© Microsoft Bing™ Maps). The two facades marked by the dashed red rectangles are completely plain which leads to a very low PS density.

In figure 4.22 two completely plain facades are examined. The PS density is displayed in figure 4.22 (a), while an oblique view aerial image of the area is presented in (b). Both investigated frontages are marked by dashed red rectangles. From (b) it becomes obvious that both facades are flat (the blue horizontal strip at the facade on the lower left in figure 4.22 (b) is due to a billboard). Obviously, only single- or double-bounce reflections can originate from such surfaces which are quite unlikely to induce PS. The resulting densities are very close to zero as clearly visible in figure 4.22 (a).

The dependence of the PS density on the shape of the surface structures is illustrated in figure 4.23. Some of the facades recognizable in the oblique view aerial image presented in (b) are highlighted by colored polygons. The colors indicate different setups. Frontages enclosed by green and blue

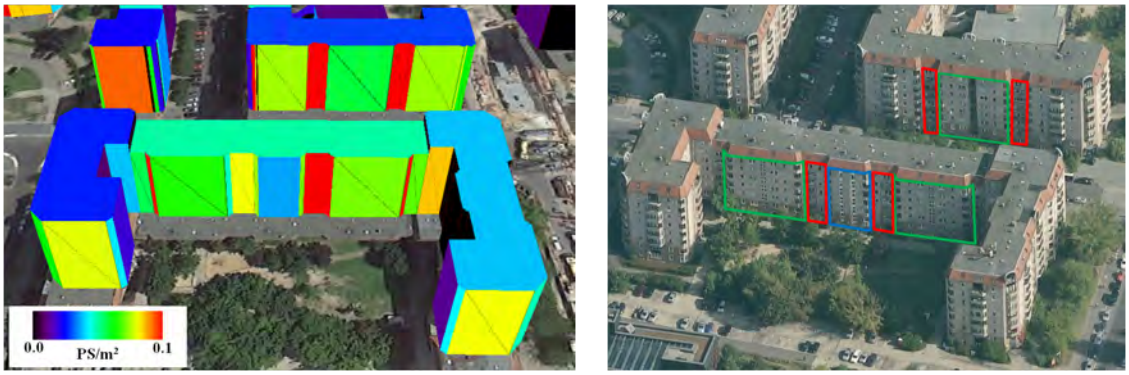

(a) (b)

Figure 4.23.: Dependence of the PS density on the surface structure. (a) Density map of the ascending PS result. (b) Corresponding oblique view aerial image (© Microsoft Bing™ Maps). The colors of the polygons in (b) indicate facades of similar structures. In (a) the correlation in density between similar facades is recognizable.

polygons exhibit medium densities. They are made of flat concrete slabs interrupted by windows. In contrast, facades marked in red show exceptionally high densities. They accommodate balconies. Certainly, also other factors are involved which becomes obvious from the deviation in density among apparently equal facades. For instance, one of the facades framed in red differs in density from the others. While all show values around 0.9 PS per square meter, the one on the lower left features a density around 0.8.

Shadowing

The impact of shadowing is illustrated using the two buildings marked by rectangle (2) in figure 4.21 (a). In figure 4.24 (a) the corresponding density map for the ascending dataset is presented. The arrow indicates the sensors LoS. The building on the right causes shadowing of the bottom part of the left building leading to a quite low point density at the facade marked by the dashed red rectangle. The few identified PS are all located at its left edge, which is not occluded. The upper part which is marked by the bold red rectangle is visible to the sensor and shows a higher density. It is worth to note that the structures of the upper and the lower frontages differ. In figure 4.24 (b) the descending density map of the same buildings is shown. The frontage indicated by the dashed red rectangle features the same setup as the one marked accordingly in (a) and shows a high density of around 0.7 PS per square meter. This suggests that also the sparsely populated frontage visible in (a) would accommodate a plethora of points if it was not occluded.

Aspect dependency

The number of identified PS at facades depends on their orientation with respect to the sensor LoS. This is demonstrated in figure 4.25. An oblique view aerial image of the considered building complex is displayed in (b). The projection of the LoS of the sensor onto the ground roughly coincides with the direction of the street (traversed from right to left) visible at the bottom of the image. The frontages

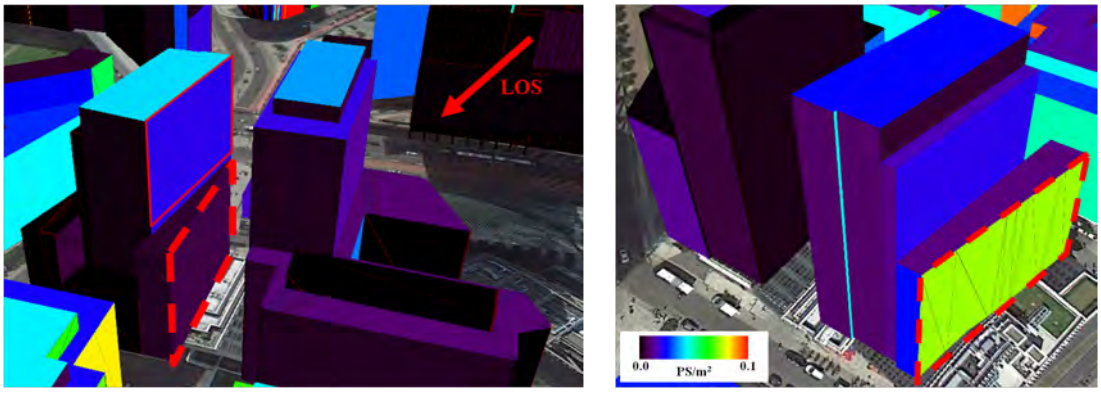

(a) (b)

Figure 4.24.: Impact of shadowing on the PS density. (a) Density map of the ascending PS result. The bottom part of the left building is occluded by the building on the right. Only the upper part is visible to the sensor (red rectangle), which results in a very low density (dashed red rectangle). (b) Density map of the descending result showing the other side of the building. The facade marked by the dashed red rectangle exhibits a quite high density and accommodates the same structures as the facade indicated accordingly in (a).

of the building complex accommodate structures that are quite likely to induce PS. Figure 4.25 (a) depicts the corresponding section of the ascending density map. Clearly, the number of identified PS is much higher at facades oriented almost perpendicular to the viewing direction of the sensor. This is due to the dependence of the size of the facade in the SAR image on the surface orientation with respect to the sensor's LoS. Of course, the frontages located on the right side of figure 4.25 do not contain any PS at all since they are not visible to the SAR system. Those facades at the central part are seen at an acute angle, which leads to low densities. It is worth to mention that particular reflection mechanisms exhibit a more complicated angle dependency. If one plane of a corner reflector is, for instance, aligned with the LoS of the SAR, the reflection mechanism is dihedral instead of trihedral which potentially leads to a much weaker signal. Obviously, an investigation of such issues would require building models of higher LOD and is, thus, out of the scope of this work.

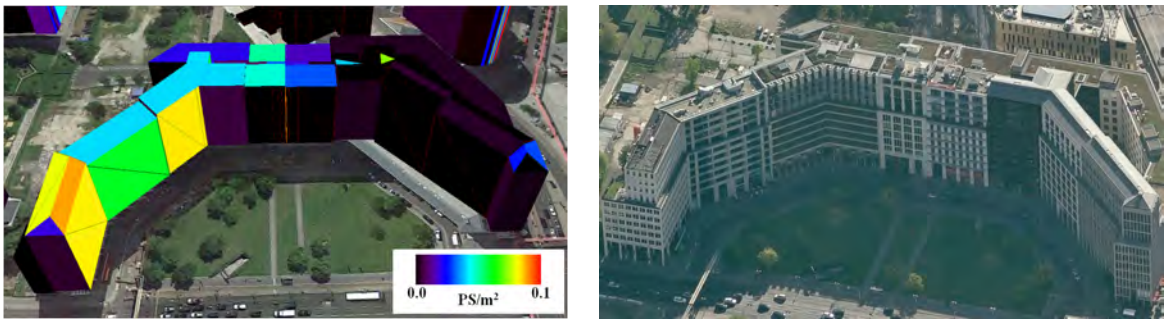

(a) (b)

Figure 4.25.: Dependence of the PS density on the aspect. (a) Density map of the ascending PS result. (b) Corresponding oblique view aerial image (© Microsoft Bing™ Maps). The PS density depends on the orientation of the facade with respect to the sensor's LoS. This is nicely illustrated by the increase in point density at the facades going from right to left.

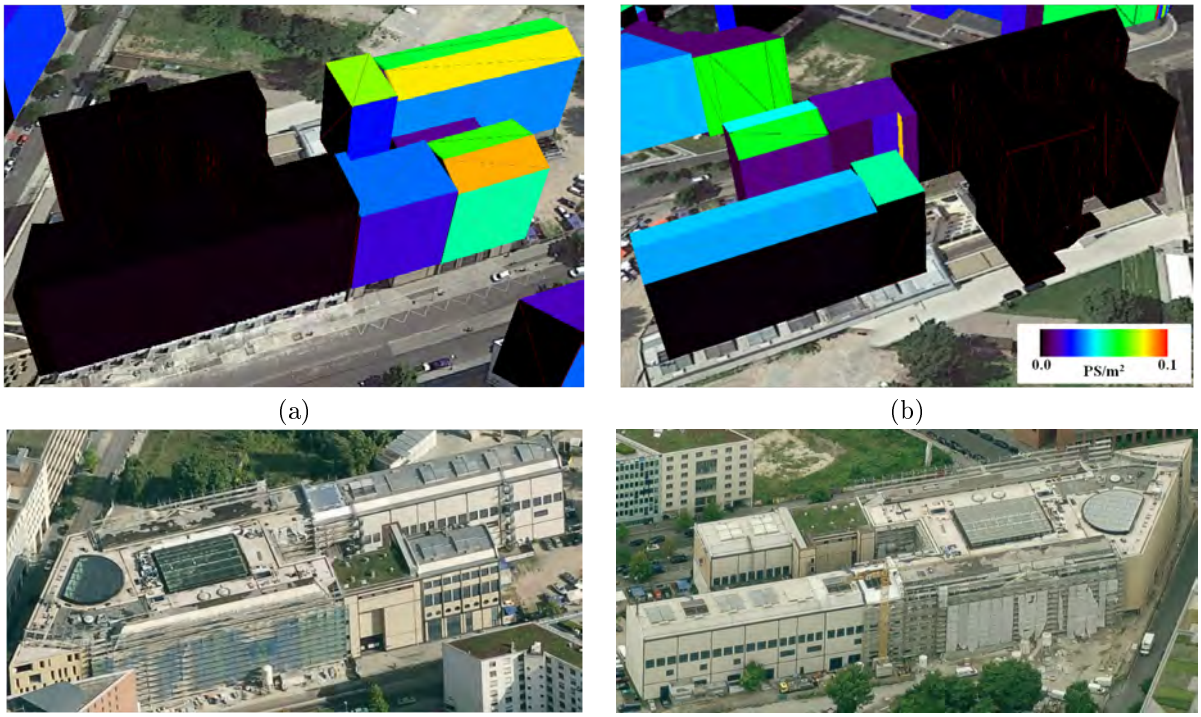

Figure 4.26.: Influence of quasi-random processes on the PS density. (a) and (b) Density map of the ascending and the descending PS result. (c) and (d) Corresponding oblique view aerial images (© Microsoft Bing™ Maps). One half of the building complex shows medium densities, while the other hardly accommodates any PS. The reason is ongoing construction during the acquisition of the data stacks. This becomes apparent from the scaffolds visible in the oblique view aerial images.

Quasi-random influences

Finally, it is important to stress the variety of factors influencing the PS density. A good example for that is a trihedral reflection mechanism at a facade formed by the window sill, a part of the wall, and the frame of the window. If the window is always closed during the acquisition of the data stack, a PS is likely to be induced. However, if the window is opened once during an acquisition, the PS may be lost. In essence, a lot of "random" factors influence the persistence of a reflection mechanism over time. A nice example for this fact is shown in figure 4.26. One half of the shown building complex exhibits an average density, while virtually no PS are found at the other half (except for a few located on the roof). This becomes obvious from the ascending and descending density maps presented in figure 4.26 (a) and (b), respectively. The reason for such low density becomes apparent from the corresponding oblique view aerial images displayed in figure 4.26 (c) and (d). At both sides of the building scaffolds are discernible. That implies that the building has been under construction while the stack was acquired, which led to the loss of all facade PS. Since both stacks cover a time-frame of four years, the construction, most likely, only disturbed a subset of the interferograms. The resulting phase fluctuations are interpreted as noise and the PS are rejected.

5. Summary

In this chapter the major finding of this thesis are summarized and conclusions are drawn. Finally, directions for future work are discussed. Four main topics are addressed separately: Grouping of the PS set, assignment of PS to building models, relations of identified PS patterns to facade structures, and the determination of the point density at building faces.

5.1. Findings

Grouping

The most noticeable feature of the grouping results is the heterogeneous outcome at different facades. In the ascending dataset, one building complex contains a large number of groups. This density of patterns is unique within the obtained results. At some of the related facades, the majority of points is affiliated to one of the groups (i.e. above 60% of the PS). The point distribution at most other buildings is considerably less regular resulting in a small number of identified groups (i.e. 0 to 30% of the PS are grouped). Cases where around 30% to 60% of the PS at a facade are contained in a group are rare (e.g. two of the facades marked by rectangle (4) in figure 4.10). However, some degree of alignment with the related building facades is observable in most cases. Only few buildings exhibit a point arrangement that seems completely random. A major factor is layover. The facades that show the highest pattern densities are those with the least intersection with other frontages in the range-azimuth plane. The effect of layover is two-fold. Firstly, PS may be lost due to interference. Secondly, patterns may be superimposed on each other. In general, both effects mix, which leads to a seemingly random point distribution in the worst case. Another factor are the real world structures that induce the PS. Some lead to more regular patterns than others, although their distribution along the facades is very similar. Furthermore, different behavior of facades accommodating the same structures but seen under a different angle by the sensor has been observed. In essence, the PS distribution is very often correlated with the setup of the facade (e.g. horizontal lines are recognizable) but does not constitute a perfectly regular lattice. The latter is required in order to obtain good results with the proposed grouping method. A very good example for that are the facades (2), (5), and (6) in figure 4.10. The PS are clearly arranged regularly. However, the algorithm fails to detect those patterns.

The main problem is the restrictive requirement imposed on the points distribution in the utilized algorithm. Firstly, the definition of regular patterns is too narrow. Demanding single PS to be

equally spaced is especially critical since it inherently assumes the arrangement of facade details to be lattice-like. However, most frontages show a more complicated setup which often consists in a periodic appearance of groups of structures (e.g. two windows of probably different setup and a balcony appear periodically along one floor). Secondly, the utilized method is based on thresholds. Although the latter are derived using statistical considerations, the involved hard decisions render the algorithm inflexible. PS are either related or unrelated. Patterns that do not perfectly match the assumed regularity are completely lost with all the information comprised in them.

In conclusion, the proposed grouping algorithm is designed to find patterns at facades that exhibit a very regular point distribution. Since most facades do not fulfill this condition, the number of identified patterns is too small in the majority of areas to really support the parameter estimation. Certainly, the improvement in the geolocation of some PS is a step forward. However, more flexible pattern recognition methods could obtain much more information comprised in the arrangement of the PS and help to exploit the full potential of high resolution SAR data stacks.

Assignment of PS to building models

The assignment of PS to building faces is conducted point by point using a purely geometric criterion. It has been shown that the affiliation of PS to facades is quite unproblematic. This is due to the fact that the utilized building models compare quite well with the actual building surfaces at frontages and the locational accuracy of the PS is sufficient. Furthermore, the planimetric alignment of both datasets is relatively reliable. The situation for building roofs is quite different. In the shown case studies, the PS do not compare well at the relevant faces. This is primarily due to generalization of the building models. The main effect are missed correspondences caused by large distances between the PS and the modeled roofs. However, in some cases roof PS are assigned to those faces. Such relations are not wrong. However, their use in view of the motivated exploitation of the assignment for improved deformation modeling is questionable as the building is not represented properly with respect to the real word. Furthermore, the validity of the registration in vertical direction remains questionable. A residual misalignment in the decimeter range, may lead to some misallocations or missed correspondences.

In case study (a) (cf. figures 4.15 and 4.17) surprisingly many PS are located within the considered building model. Most of them are not assigned to any of the building faces. Thus, those points do not constitute a big problem for the assignment result. It appears implausible that such PS are induced by reflection mechanisms located inside the building as the required signal path would be unlikely to be persistent over time. This raises the question concerning their physical nature. Virtual corners are a possibility. However, the large number of such points does not support this explanation since virtual corners are expected to be rather rare. It is very important to note that such PS may lead to major problems in deformation monitoring if they are, actually, induced by virtual corner reflectors or similar mechanisms. In case those points exhibit deformation, the corresponding building (i.e. the closest building) is assumed to be somehow unstable. In fact, the estimated motion is due to

the movement of different scene structures, which may be located far away. This would pose a big problem for the assessment of small scale deformation with PSI.

The obtained assignment results are definitely sufficient for the compilation of a meaningful density map. It has to be kept in mind that the results may be less reliable at building roofs if strong generalization effects are present. Even the utilization of the determined correspondences for the extension of the applied deformation model appears possible (cf. [Gernhardt & Hinz, 2008]). However, as outliers and insufficient building representations may appear in some instances, robust estimation procedures should be applied.

Assignment of PS to facade structures

The comparison of horizontal facade structures present in LIDAR data with groups of PS shows a clear correlation between them. Two building are investigated that exhibit a lattice-like arrangement of windows which becomes obvious from oblique view aerial images. Both, PS and LIDAR points, are very likely to originate from those windows. The assessment of the vertical distances between both datasets revealed a significant systematic difference at one of the investigated buildings. This difference seems to be dependent on the relative orientation between sensor and facade which implies an aspect dependency of the scattering mechanism. Both finding are not surprising since the windows at this building feature a complex design. At the other building, two of the investigated facades contain very plain windows. The corresponding PS are assumed to be induced by trihedral reflection mechanisms involving the window sills. At those facades, the PS groups are expected to exhibit very small (i.e. not significant) vertical distances to the LIDAR patterns, which are also anticipated to be induced by reflections at the sills of the windows. While the mean distance is not significant for one of those facades, it turns out to be significant at the other facade. This implies an aspect dependency of the respective reflection mechanisms which is unexpected. One of the main questions concerns the significance of the determined offsets. For instance, at one of the facades at building (a) (cf. figure 4.20), one of the group shows implausible results. By removing it from the evaluation, the difference at building surfaces of distinct orientation becomes hardly significant. As an uncertainty of the registration of the PS in z-direction or even a systematic offset of the LIDAR point cloud cannot be excluded, a clear assessment of systematic vertical distances between PS and LIDAR is difficult.

Point density

The estimation of the point density shows that most buildings accommodate at least a few PS. However, many building faces are only sparsely sampled, which is especially true at roofs. Among the four addressed driving factors determining the PS density, the structure of the bounding surface as well as quasi-random influences are the most interesting. Two completely plain facades are illustrated. From those, only single and double reflections can originate. Both are not very likely to

induce PS. Consequently, those surfaces show very low densities. Furthermore, faces of alike structure feature similar point densities. If roofs or facades accommodate a large number of small details and only few areas that are completely plain, they are likely to exhibit high PS densities. However, quasi-random influences may accompany all sudden scene changes during the acquisition of the data stack. The corresponding example shows a building whose facade was under construction while the data was collected. Consequently, all corresponding PS are lost. This may be a major problem as PSI is especially interesting for rapidly evolving cities to monitor the effects of construction or increased ground water removal.

In some instances facades of identical setup show a significantly different density (cf. figure 4.23). Whether this is due to the assignment procedure or an actual difference in density has not been investigated. However, in case the latter applies, a closer investigation may be interesting. Finally, the list of factors that influence the PS density is, of course, not complete. For instance, the impact of layover between building facade, roof, and the ground surface in front is not assessed due to the highly complicated inter-dependencies.

5.2. Future Work

As outlined, the proposed grouping method has some limitations. Because of that a lot of useful information comprised in the spatial arrangement of the PS is lost. A simple way to improve the performance of the grouping is to add a search for regular patterns in range direction. Contrary to the grouping parallel to the building outlines, this approach aims to identify periodic arrangements of structures with the same planimetric positions but located on top of one another. Finally, the results of the two 1-D searches could be fused. As both grouping approaches share similar limitations, a significant improvement of the results cannot be expected. Thus, the application of more flexible methods is necessary. In order to address complex patterns, shape or facade grammars are a possibility. Those have already been used for facade reconstruction from terrestrial photographs [Ripperda & Brenner, 2006; Riemenschneider et al., 2012]. Furthermore, several methods dealing with the identification of lattices in photographs, which are quite robust, are available. For instance, the method proposed by Park et al. [2009] uses a MRF framework, which allows for a natural incorporation of uncertainty. Moreover, by considering several point pairs at a time, the method is very robust. As this procedure uses extended image patches as primitive objects, it has to be adapted to fit the problem at hand. Finally, for the incorporation of model knowledge in the parameter estimation process of PSI an approach similar to [Shabou et al., 2012] may be beneficial. The chance that PS aligned parallel to a building outline feature a similar vertical position is quite high. This knowledge could, for instance, be represented in the smoothness term of a MRF. As in [Shabou et al., 2012] this may lead to a regularization of the obtained parameter estimates.

The main problem in the assignment procedure is the generalization of the building models. Of course, this could be tackled by using more detailed models. However, such data are very expensive

and rarely available. In order to avoid false correspondences, spatially related PS could be assigned jointly to the building surfaces. This would additionally give some information about systematic differences between PS and city model. Such spatial relation between the PS could be inferred from their distribution in the range-azimuth plane or by segmenting the geocoded point clouds.

In order to understand the physical nature of the PS that are located inside the building shown in figures 4.15 and 4.17, SAR simulation could be used (cf. Auer [2011]). However, to include all possible reflection mechanisms, a large number of highly detailed building models around the investigated location have to be available.

To enhance the assignment of PS to facade details, the use of more detailed reference data appears beneficial. One possibility is the exploitation of mobile mapping data which features a much higher point density at facades. This would facilitate the assessment of potential relations between PS and real world structures.

5.3. Conclusion

Within this work, four topics were addressed: The assignment of PS to buildings, the detection of horizontal patterns of PS at building facades, the compilation of a PS density map, and the assignment of PS to facade details. The focus of this thesis lay on the first two topics.

The main objectives concerning the first topic were the development of an algorithm assigning the PS to the building model and the assessment of the comparability of both datasets. In summary those objectives have been met. It was shown that such assignment is relatively straightforward (i.e. using a nearest neighbor criterion) in the majority of the cases. Within the investigation, a significant number of PS located inside of buildings was detected. This is a very important finding as it shows the necessity of an assignment of the PS to the objects under investigation to avoid misinterpretation of the obtained deformation results.

Regarding the detection of horizontal PS patterns, the targets were the development of a grouping method and the investigation of the conditions that are required for the emergence of such patterns. The latter objective has been clearly met. The strong influence of layover as well as the importance of the reflection mechanism inducing the PS were shown. However, the first objective has been met only partially. The proposed grouping method is only suited for very simple settings which includes only a subset of the facades encountered in a typical scene.

A density map has been compiled using the assignment of PS to buildings with the aim to study the main factors influencing the PS density. Although those factors were not investigated comprehensively (e.g. the influence of the surface in front of facades could not be assessed), this study provides a major improvement in the understanding of the PS distribution in urban settings.

Finally, an investigation with the target to relate PS to facade details, represented by LIDAR data, was conducted. Within this study the mean vertical distances between groups of PS and horizontal

LIDAR patterns for facades at two different buildings were estimated. The obtained vertical offsets remain very uncertain which renders definite conclusions difficult. As it is challenging to reduce those uncertainties (especially the one due to inaccuracies of the alignment), other strategies, such as SAR simulation, seem to be better suited to investigate the relation of PS to real world structures.

Bibliography

Adam N, Kampes BM, Eineder M (2004) Development of a scientific Persistent Scatterer System: Modifications for mixed ERS/ENVISAT time series. In: *ENVISAT & ERS Symposium, Salzburg, Austria*: 9.

Adam N, Kampes BM, Eineder M, Worawattanamateekul J, Kircher M (2003) The development of a scientific permanent scatterer system. In: *ISPRS Workshop High Resolution Mapping from Space, Hannover, Germany, 2003*: 6 pp.

Adam N, Parizzi A, Eineder M, Crosetto M (2009) Practical persistent scatterer processing validation in the course of the Terrafirma project. *Journal of Applied Geophysics*, 69 (1): 59 – 65.

Auer S (2011) *3D Synthetic Aperture Radar Simulation for Interpreting Complex Urban Reflection Scenarios.* PhD thesis, Fakultät fär Bauingenieur- und Vermessungswesen der Technischen Universität München.

Auer S, Bamler R (2010) 3D Analysis of Trihedral Reflection Based on SAR Simulation Methods. In: *8th European Conference on Synthetic Aperture Radar (EUSAR), 2010*: 1–4.

Auer S, Gernhardt S, Bamler R (2011a) Ghost Persistent Scatterers Related to Multiple Signal Reflections. *Geoscience and Remote Sensing Letters, IEEE*, 8 (5): 919–923.

Auer S, Gernhardt S, Bamler R (2011b) Investigations on the nature of Persistent Scatterers based on simulation methods. In: *Proc. Joint Urban Remote Sensing Event (JURSE)*: 61–64.

Bamler R, Eineder M, Adam N, Zhu X, Gernhardt S (2009) Interferometric Potential of High Resolution Spaceborne SAR. *Photogrammetrie - Fernerkundung - Geoinformation*, (5): 407–419.

Bamler R, Hartl P (1998) Synthetic aperture radar interferometry. *Inverse Problems*, 14 (4): R1.

Bamler R, Schättler B (1993) *SAR Data Acquisition and Image Formation.* In: G. Schreier: *SAR Geocoding: Data and Systems.* Wichmann, Karlsruhe, Germany.

Besl PJ, McKay ND (1992) A Method for Registration of 3-D Shapes. *Transactions on Pattern Analysis and Machine Intelligence*, 14 (2): 239–256.

Bowman AW, Azzalini A (1997) *Applied Smoothing Techniques for Data Analysis: The Kernel Approach with S-Plus Illustrations (Oxford Statistical Science Series).* Oxford University Press, USA.

Breit H, Fritz T, Balss U, Lachaise M, Niedermeier A, Vonavka M (2010) TerraSAR-X SAR Processing and Products. *IEEE Transactions on Geoscience and Remote Sensing*, 48 (2): 727 –740.

Chen CW (2001) *Statistical-cost network-flow approaches to two-dimensional phase unwrapping for radar interferometry.* PhD thesis, Stanford University.

Chen CW, Zebker HA (2000) Network approaches to two-dimensional phase unwrapping: intractability and two new algorithms. *J. Opt. Soc. Am. A*, 17 (3): 401–414.

Colesanti C, Ferretti A, Novali F, Prati C, Rocca F (2003a) SAR monitoring of progressive and seasonal ground deformation using the permanent scatterers technique. *IEEE Transactions on Geoscience and Remote Sensing*, 41 (7): 1685–1701.

Colesanti C, Ferretti A, Prati C, Rocca F (2003b) Monitoring landslides and tectonic motions with the Permanent Scatterers Technique. *Engineering Geology*, 68 (1-2): 3 – 14.

Cumming IG, Wong FH (2005) *Digital Processing of Synthetic Aperture Radar Data: Algorithms and Implementation.* Boston, London: Artech House Inc.

Desolneux A, Moisan L, Morel JM (2004) *Seeing, Thinking and Knowing*, chapter Gestalt Theory and Computer Vision, (pp. 71–101). A. Carsetti ed., Kluwer Academic Publishers.

Dong Y, Forster B, Ticehurst C (1997) Radar backscatter analysis for urban environments. *International Journal of Remote Sensing*, 18 (6): 1351–1364.

DORIS User Manual (1998) *Delft Object-oriented Radar Interferometric Software (DORIS), User's manual and technical documentation.* Delft Institute of Earth Observation and Space Systems (DEOS), Delft University of Technology, Delft, The Netherlands.

Draper BA, Collins RT, Brolio J, Hanson AR, Riseman EM (1989) The schema system. *International Journal of Computer Vision*, 2 (3): 209–250.

Eineder M, Adam N, Brcic R, Yague-Martinez N, Fritz T (2008) High Bandwidth Spotlight SAR Interferometry with TerraSAR-X. In: *Geoscience and Remote Sensing Symposium, 2008. IGARSS 2008. IEEE International.* 2: II–113 –II–116.

Ferretti A, Prati C, Rocca F (1999) Non-Uniform Motion Monitoring Using the Permanent Scatterers Technique. In: *Second International Workshop on ERS SAR Interferometry 'FRINGE99'*: 1–6.

Ferretti A, Prati C, Rocca F (2000) Nonlinear subsidence rate estimation using permanent scatterers in differential SAR interferometry. *IEEE Transactions on Geoscience and Remote Sensing*, 38 (5): 2202–2212.

Ferretti A, Prati C, Rocca F (2001) Permanent scatterers in SAR interferometry. *IEEE Transactions on Geoscience and Remote Sensing*, 39 (1): 8 –20.

Fornaro G, Reale D, Serafino F (2009) Four-Dimensional SAR Imaging for Height Estimation and Monitoring of Single and Double Scatterers. *IEEE Transactions on Geoscience and Remote Sensing*, 47 (1): 224–237.

Fornaro G, Serafino F, Soldovieri F (2003) Three-dimensional focusing with multipass SAR data. *IEEE Transactions on Geoscience and Remote Sensing*, 41 (3): 507 – 517.

Gernhardt S (2012) *High Precision 3D Localization and Motion Analysis of Persistent Scatterers using Meter-Resolution Radar Satellite Data*. PhD thesis, Fakultät fär Bauingenieur- und Vermessungswesen der Technischen Universität München.

Gernhardt S, Cong X, Eineder M, Hinz S, Bamler R (2012) Geometrical Fusion of Multitrack PS Point Clouds. *Geoscience and Remote Sensing Letters, IEEE*, 9 (1): 38 –42.

Gernhardt S, Hinz S (2008) Advanced Displacement Estimation for PSI using High Resolution SAR Data. In: *Geoscience and Remote Sensing Symposium, 2008. IGARSS 2008. IEEE International*. 3: III –1276 –III –1279.

Ghiglia DC, Romero LA (1996) Minimum Lp-norm two-dimensional phase unwrapping. *Journal of the Optical Society of America A*, 13 (10): 1999–2013.

Goel K, Adam N (2012) Three-Dimensional Positioning of Point Scatterers Based on Radargrammetry. *IEEE Transactions on Geoscience and Remote Sensing*, 50 (6): 2355–2363.

Goldstein RM, Zebker H, Werner CL (1988) Satellite Radar Interferometry: Two-Dimensional Phase Unwrapping. *Radio Science*, 23: 713–720.

Hanssen R (2001) *Radar interferometry: data interpretation and error analysis*, volume 2 of *Remote Sensing and Image Processing*. Dordrecht, The Netherlands: Kluwer Academic Publishers.

Hays JH, Leordeanu M, Efros AA, Liu Y (2006) Discovering Texture Regularity as a Higher-Order Correspondence Problem. In: *9th European Conference on Computer Vision*

Hooper A (2006) *Persistent Scatterer Radar Interferometry for Crustal Deformation Studies and Modeling of Volcanic Deformation*. PhD thesis, Stanford University.

Kada M (2009) The 3D Berlin Project. In: Fritsch D (ed) *Photogrammetric week*. Wichmann, Heidelberg, 9: 331–340.

Kampes BM (2006) *Radar Interferometry: Persistent Scatterer Technique*, volume 12 of *Remote Sensing and Digital Image Processing*. Springer.

Ketelaar V (2010) *Satellite Radar Interferometry: Subsidence Monitoring Techniques*. Remote Sensing and Digital Image Processing. Springer.

Kolbe TH (2007) *Candidate OpenGIS® CityGML Implementation Specification: City Geography Markup Language (Version 0.4.0)*. Wayland (MA), USA: OGC, 07-062 edition.

Liebhart W, Adam N, Parizzi A (2010) Least Squares Estimation of PSI Networks for Large Scenes with Multithreaded Singular Value Decomposition. *8th European Conference on Synthetic Aperture Radar (EUSAR), 2010*, : 1 –4.

Liu G, Buckley SM, Ding X, Chen Q, Luo X (2009) Estimating Spatiotemporal Ground Deformation With Improved Permanent-Scatterer Radar Interferometry. *IEEE Transactions on Geoscience and Remote Sensing*, 47 (8): 2762–2772.

Liu Y, Collins R, Tsin Y (2004) A Computational Model for Periodic Pattern Perception Based on Frieze and Wallpaper Groups. *IEEE Transactions on Pattern Analysis and Machine Intelligence*, 26 (3): 354 – 371.

Lombardini F (2003) Differential tomography: a new framework for SAR interferometry. In: *Proceeding IEEE International Geoscience and Remote Sensing Symposium, 2003*. 2: 1206–1208.

Low KL (2004) *Linear Least-Squares Optimization for Point-to-Plane ICP Surface Registration*. University of North Carolina at Chapel Hill, Technical report.

Massonnet D, Feigl KL (1998) Radar interferometry and its application to changes in the Earth's surface. *Reviews of Geophysics*, 36 (4): 441–500.

Matsuyama T, Hwang VS (1990) *SIGMA: A Knowledge-Based Aerial Image Understanding System*. Perseus Publishing.

May NC, Toth CK (2007) Point positioning accuracy of airborne LiDAR systems: A rigorous analysis. In: *International Archives of Photogrammetry and Remote Sensing*. Photogrammetric Image Analysis Munich 2007, 36: 107–111.

Meier E, Frei U, Nüesch D (1993) *Precise Terrain Corrected Geocoded Images*. In: G. Schreier: *SAR Geocoding: Data and Systems*. Wichmann, Karlsruhe, Germany.

Michaelsen E, Arens M, Doktorski L (2009) Interaction of Control and Knowledge in a Structural Recognition System. In: Mertsching B, Hund M, Aziz Z (eds) *KI 2009: Advances in Artificial Intelligence*, volume 5803 of *Lecture Notes in Computer Science* (pp. 73–80). Springer Berlin Heidelberg.

Michaelsen E, Soergel U, Stilla U (2002) Grouping salient scatterers in InSAR data for recognition of industrial buildings. In: *Proceedings 16th International Conference on Pattern Recognition, 2002*. 2: 613–616 vol.2.

Michaelsen E, Soergel U, Thoennessen U (2006) Perceptual grouping for automatic detection of man-made structures in high-resolution SAR data. *Pattern Recognition Letters*, 27 (4): 218 – 225.

Michaelsen E, Stilla U, Soergel U, Doktorski L (2010) Extraction of building polygons from SAR images: Grouping and decision-level in the GESTALT system. *Pattern Recognition Letters*, 31 (10): 1071 – 1076.

Mikhail EM, Ackermann FE (1982) *Observations and least squares*. University Press of America.

Park M, Brocklehurst K, Collins R, Liu Y (2009) Deformed Lattice Detection in Real-World Images using Mean-Shift Belief Propagation. *IEEE Transactions on Pattern Analysis and Machine Intelligence (PAMI), Special Issue on Probabilistic Graphical Models*, 31 (10).

Perissin D, Ferretti A (2007) Urban-Target Recognition by Means of Repeated Spaceborne SAR Images. *IEEE Transactions on Geoscience and Remote Sensing*, 45 (12): 4043–4058.

Raggam J, Strobl D, Hummelbrunner W (1993) *Product Quality Enhancement and Quality Evaluation*. In: G. Schreier: *SAR Geocoding: Data and Systems*. Wichmann, Karlsruhe, Germany.

Reigber A, Moreira A (2000) First demonstration of airborne SAR tomography using multibaseline L-band data. *IEEE Transactions on Geoscience and Remote Sensing*, 38 (5): 2142–2152.

Riemenschneider H, Krispel U, Thaller W, Donoser M, Havemann S, Fellner D, Bischof H (2012) Irregular lattices for complex shape grammar facade parsing. In: *IEEE Conference on Computer Vision and Pattern Recognition (CVPR) 2012*: 1640–1647.

Rife D, Boorstyn R (1974) Single tone parameter estimation from discrete-time observations. *IEEE Transactions on Information Theory*, 20 (5): 591 – 598.

Ripperda N, Brenner C (2006) Reconstruction of façade structures using a formal grammar and RjMCMC. In: *Pattern Recognition* (pp. 750–759). Springer.

Schunert A, Soergel U (2012) Grouping of Persistent Scatterers in high-resolution SAR data of urban scenes. *ISPRS Journal of Photogrammetry and Remote Sensing*, 73: 80–88.

Shabou A, Baselice F, Ferraioli G (2012) Urban Digital Elevation Model Reconstruction Using Very High Resolution Multichannel InSAR Data. *IEEE Transactions on Geoscience and Remote Sensing*, 50 (11): 4748–4758.

Soergel U (2003) *Iterative Verfahren zur Detektion und Rekonstruktion von Gebäuden in SAR- und InSAR-Daten*. PhD thesis, Fachbereich Elektrotechnik und Informationstechnik der Universität Hannover.

Soergel U, Cadario E, Thiele A, Thoennessen U (2008) Feature extraction and visualization of bridges over water from high-resolution InSAR data and one orthophoto. *IEEE Journal of Selected Topics in Applied Earth Observations and Remote Sensing*, 1 (2): 147–153.

Teunissen P (1995) The least-squares ambiguity decorrelation adjustment: a method for fast GPS integer ambiguity estimation. *Journal of Geodesy*, 70: 65–82.

Torge W (2001) *Geodesy*. Walter de Gruyter.

Touzi R, Lopes A, Bousquet P (1988) A statistical and geometrical edge detector for SAR images. *IEEE Transactions on Geoscience and Remote Sensing*, 26 (6): 764–773.

Tupin F, Maitre H, Mangin JF, Nicolas JM, Pechersky E (1998) Detection of linear features in SAR images: application to road network extraction. *IEEE Transactions on Geoscience and Remote Sensing*, 36 (2): 434–453.

Wertheimer M (1923) Untersuchungen zur Lehre von der Gestalt. II. *Psychological Research*, 4 (1): 301–350.

Wilkinson AJ (1997) *Techniques for 3-D Surface Reconstruction using Synthetic Aperture Radar Interferometry*. PhD thesis, University College London, London.

Zebker HA, Rosen PA, Hensley S (1997) Atmospheric effects in interferometric synthetic aperture radar surface deformation and topographic maps. *Journal of Geophysical Research: Solid Earth*, 102 (B4): 7547–7563.

Zebker HA, Villasenor J (1992) Decorrelation in interferometric radar echoes. *IEEE Transactions on Geoscience and Remote Sensing*, 30 (5): 950 –959.

Zhu X, Bamler R (2010) Very High Resolution Spaceborne SAR Tomography in Urban Environment. *IEEE Transactions on Geoscience and Remote Sensing*, 48 (12): 4296 –4308.

Zhu X, Bamler R (2011a) Let's Do the Time Warp: Multicomponent Nonlinear Motion Estimation in Differential SAR Tomography. *Geoscience and Remote Sensing Letters, IEEE*, 8 (4): 735–739.

Zhu X, Bamler R (2011b) Super-Resolution Power and Robustness of Compressive Sensing for Spectral Estimation With Application to Spaceborne Tomographic SAR. *IEEE Transactions on Geoscience and Remote Sensing*, (99): 1–12.

A. Appendix A

Estimating the shift

In section 3.2.2 a transformation is to be estimated from the determined correspondences. The derivation given in the following is based on Low [2004]. The solution $\hat{\mathbf{\Delta}}$ is determined as the shift that minimizes the objective function given in equation (3.26) and restated here for convenience.

$$\hat{\mathbf{\Delta}} = \text{argmin}_{\mathbf{\Delta}} \left\{ \sum_{k=1}^{K} w_k \left(d_{k,\mathbf{\Delta}} \right)^2 \right\} . \tag{A.1}$$

Each distance $d_{k,\mathbf{\Delta}}$ can be expanded into:

$$\begin{aligned} d_{k,\mathbf{\Delta}} &= \mathbf{n}_k \left(\mathbf{p}_k + \mathbf{\Delta} \right) + c_k \\ &= n_{x,k} \cdot \Delta_x + n_{y,k} \cdot \Delta_y + n_{z,k} \cdot \Delta_z + n_{x,k} \cdot p_{x,k} + n_{y,k} \cdot p_{y,k} + n_{z,k} \cdot p_{z,k} + c_k \end{aligned} \tag{A.2}$$

All K distances can be arranged in a matrix expression:

$$\mathbf{d} = \mathbf{A} \cdot \mathbf{x} - \mathbf{b} \tag{A.3}$$

where the $K \times 1$-vector $\mathbf{d}$ contains the weighted misregistrations along the elevation direction for all point correspondences. The design matrix $\mathbf{A}$ is of size $K \times 3$ and set up as follows:

$$\mathbf{A} = \begin{bmatrix} n_{x,1} & n_{y,1} & n_{z,1} \\ n_{x,2} & n_{y,2} & n_{z,2} \\ \vdots & \vdots & \vdots \\ n_{x,K} & n_{y,K} & n_{z,K} \end{bmatrix} . \tag{A.4}$$

The unknowns Δ_x, Δ_y, and Δ_z are contained in the 3×1-vector $\mathbf{x}$.

$$\mathbf{x} = \begin{bmatrix} \Delta_x \\ \Delta_y \\ \Delta_z \end{bmatrix} \tag{A.5}$$

Finally, $\mathbf{b}$ is a vector of size $K \times 1$ containing the measurements.

$$\mathbf{b} = \begin{bmatrix} -n_{x,1} \cdot p_{x,1} - n_{y,1} \cdot p_{y,1} - n_{z,1} \cdot p_{z,1} - c_1 \\ -n_{x,2} \cdot p_{x,2} - n_{y,2} \cdot p_{y,2} - n_{z,2} \cdot p_{z,2} - c_2 \\ \vdots \\ -n_{x,K} \cdot s_{x,K} - n_{y,K} \cdot s_{y,K} - n_{z,K} \cdot s_{z,K} - c_K \end{bmatrix} \tag{A.6}$$

The weights w_k are comprised in a $K \times K$ weight matrix $\mathbf{P}$:

$$P = \mathrm{diag}\,(w_k) \tag{A.7}$$

The shifts can be finally estimated by minimizing the weighted sum of residuals (i.e. the a-posteriori point to plane distances):

$$\hat{\mathbf{x}} = \mathrm{argmin}_{\mathbf{x}} \left\{ (\mathbf{A} \cdot \mathbf{x} - \mathbf{b})^T \cdot \mathbf{P} \cdot (\mathbf{A} \cdot \mathbf{x} - \mathbf{b})^T \right\} \tag{A.8}$$

which can be easily achieved using standard algorithms. A comprehensive treatment of this topic can be found in Mikhail & Ackermann [1982].

The SAR coordinate system

The parametrization of the SAR coordinate system with respect to a geographic system with x-axis oriented eastwards and y-axis pointing to the north is defined in the following. It is determined by the heading- and the look-angle of the sensor. The latter, referred to as θ, is defined in figure 2.1. The heading-angle H of the satellite is measured from the x-axis counter-clockwise[1] (i.e. from east to north). The situation is illustrated in figure A.1. The elevation-, azimuth-, and range-direction

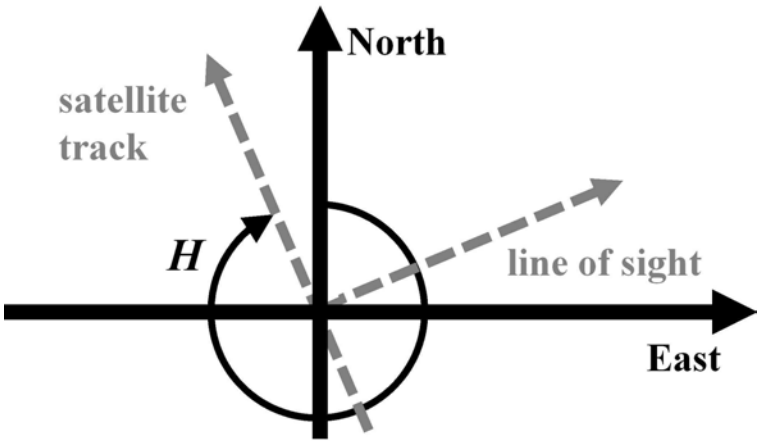

Figure A.1.: Definition of Heading Angle H

[1] In contrast to common practice, a right handed system is used.

are defined as:

$$\mathbf{x}_{s,k}^T = \begin{bmatrix} \sin(H+90)\cdot\cos(\theta) & \cos(H+90)\cdot\cos(\theta) & \sin(\theta) \end{bmatrix} \tag{A.9}$$

$$\mathbf{x}_{a,k}^T = \begin{bmatrix} \sin(H) & \cos(H) & 0 \end{bmatrix} \tag{A.10}$$

$$\mathbf{x}_{r,k}^T = \begin{bmatrix} \sin(H+90)\cdot\sin(\theta) & \cos(H+90)\cdot\sin(\theta) & -\cos(\theta) \end{bmatrix} . \tag{A.11}$$

B. Appendix B

For single PS it is not possible to verify the distribution assumption stated in section 3.3. However, in case it holds for most of the PS, the histogram of the normalized distances resembles a zero mean standard Gaussian distribution. Such histograms for the ascending and the descending datastack (cf. section 4.1.1) are shown in figure B.1 and figure B.2, respectively. Due to the different behavior, facade and roof PS are treated separately ((a) facades and (b) roofs in both figures). The assignments corresponding to those distances are determined as described in section 3.3. In contrast, to section 4.4.1 a relaxed threshold of 10 is chosen for the normalized distances to give a better impression of the data statistics. Values above 10 are excluded due to displaying purposes.

The normalized distances at facades show a symmetric distribution around zero for both datastacks. Neither the ascending nor the descending data are strictly normally distributed. In table B.1 the portion of PS contained within the bounds ± 1, ± 2, and ± 3, respectively, are presented. For comparison, the corresponding values for a standard normal distribution are given. It is apparent that the histograms feature a heavy tail, i.e. the spread of the data are larger compared to a Gaussian. Although not all of the considered assignments are valid, the results imply that the approximation of the actual distributions of the normalized distances by a standard Gaussian leads to inaccurate results for the determination of confidence intervals (cf. section 4.4.1).

The histograms of the normalized distances to roofs are strongly asymmetric. This is most likely due to generalization effects which are particularly pronounced at roofs. Thus, the distribution assumption for the corresponding normalized distances is far from being valid. It is worth to note that the obtained results are similar to the results obtained for LIDAR data (cf. section 4.1.2).

Normalized Distance	Standard Normal	Ascending	Descending
± 1.0	68.2	69.7	62.7
± 2.0	95.4	88.2	85.0
± 3.0	99.6	95.1	93.3

Table B.1.: Probability that the normalized distances are within the bounds ± 1.0, ± 2.0, or ± 3.0 for facade PS from both datastacks (cf. figure B.1 (a) and figure B.2 (a)). For comparison the corresponding values of a standard normal distribution are given.

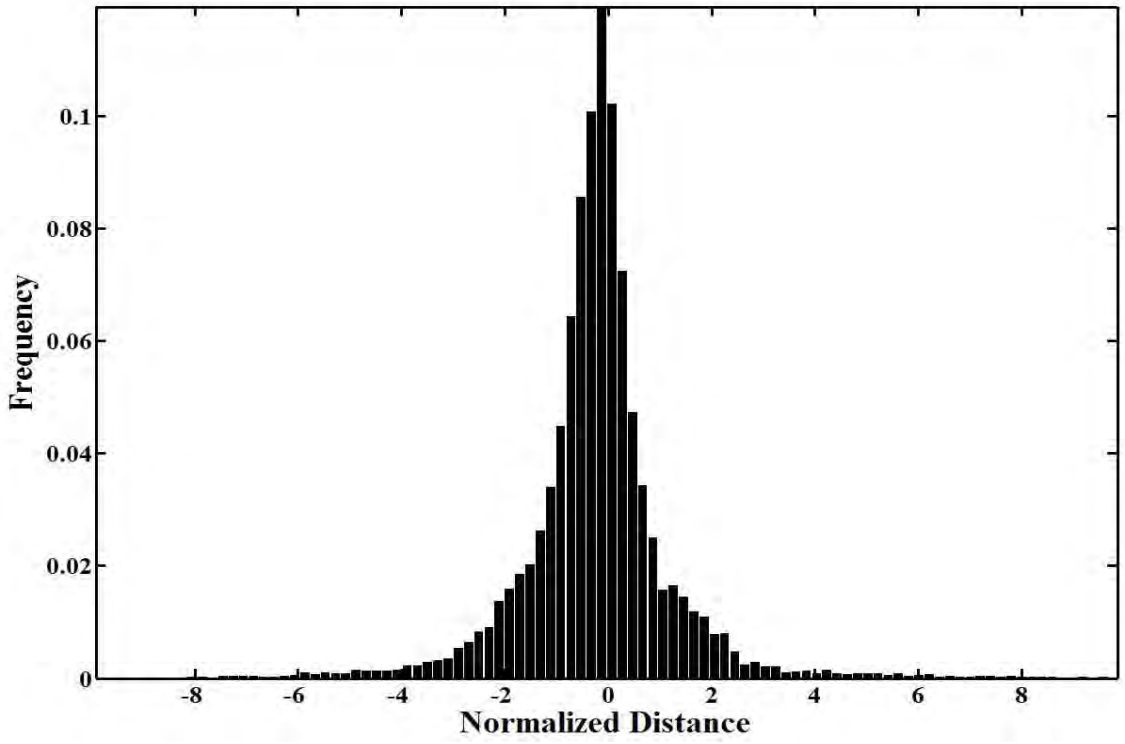

(a)

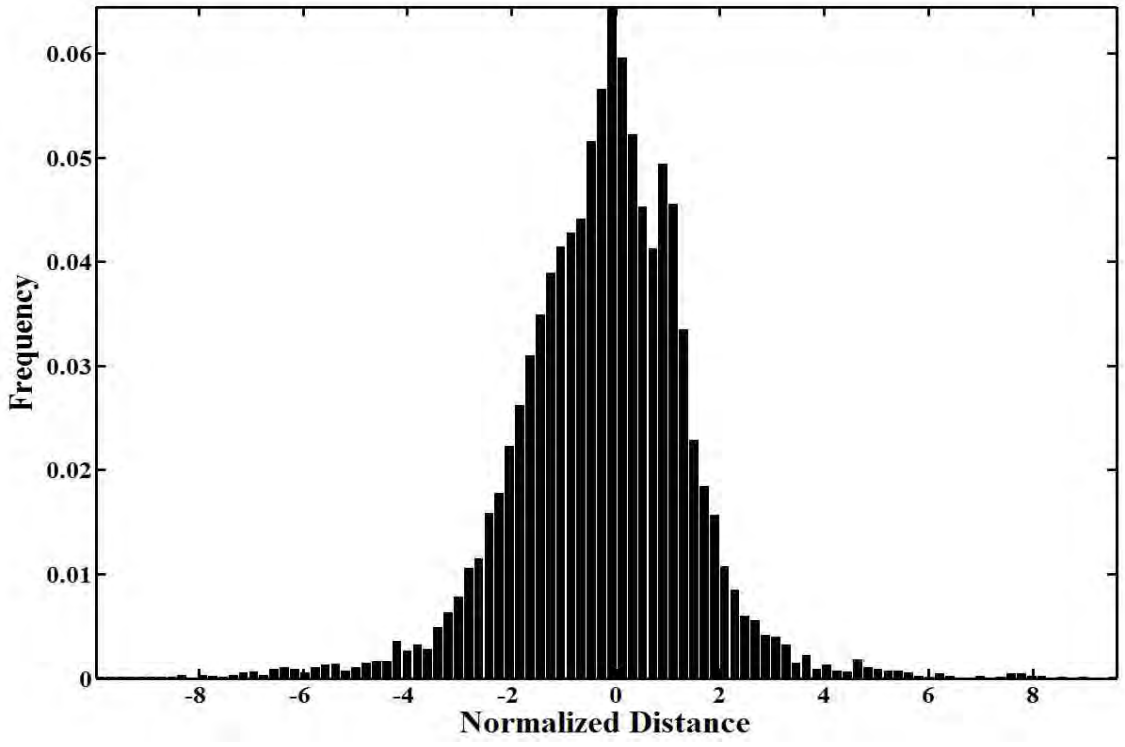

(b)

Figure B.1.: Histogram of the normalized distances for facades (a) and roofs (b) for the ascending datastack. Only those PS that are located inside at least one buffered outline are considered. Furthermore, an assignments is rejected if the perpendicular projection of the PS onto the bounding surface is located outside the polygon associated with this bounding surface. Note that for displaying purposes normalized distances above 10 are excluded.

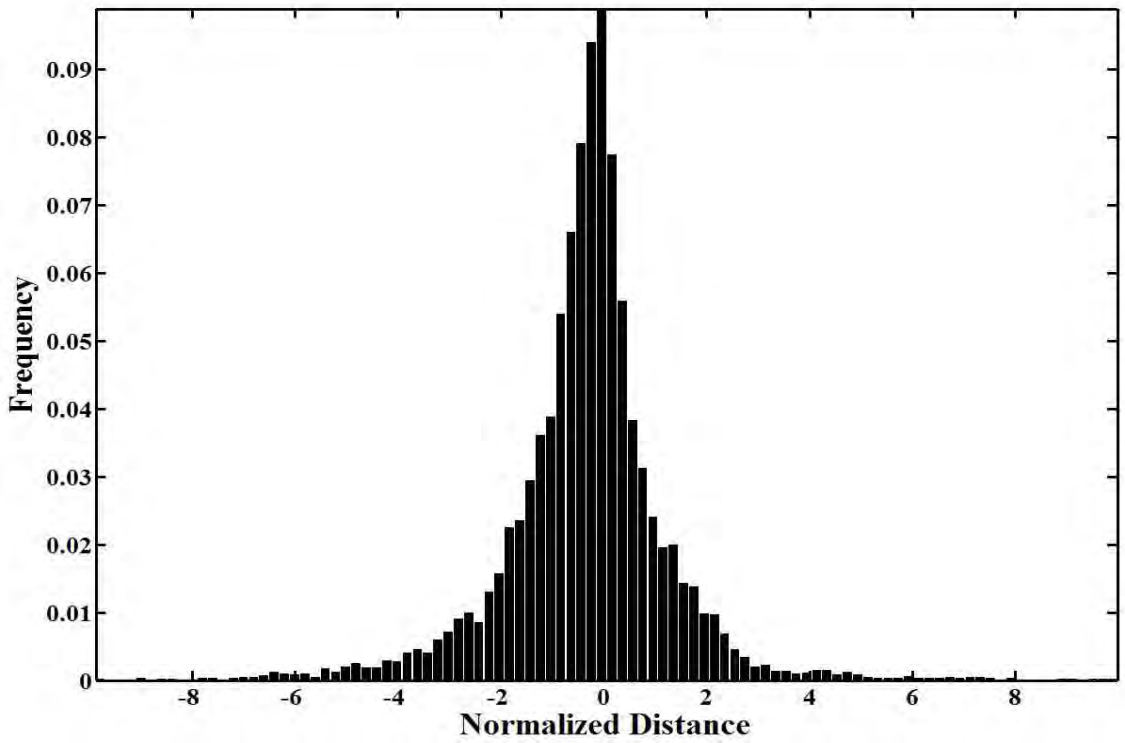

(a)

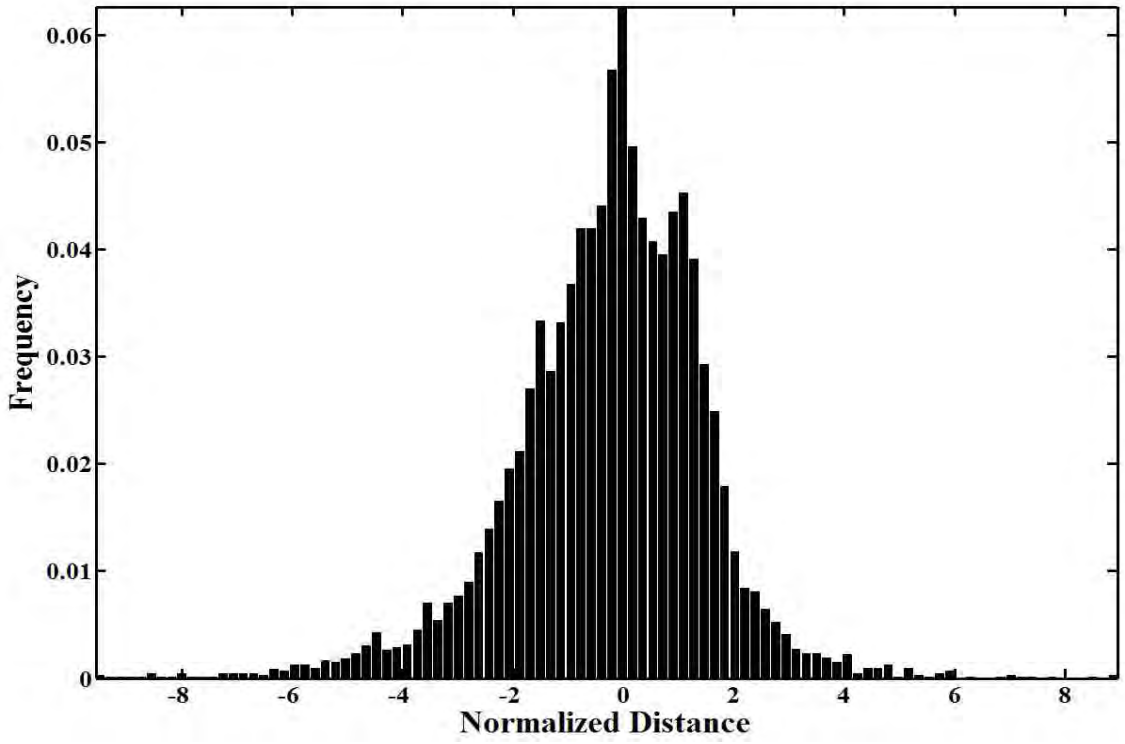

(b)

Figure B.2.: Histogram of the normalized distances for facades (a) and roofs (b) for the descending datastack. Only those PS that are located inside at least one buffered outline are considered. Furthermore, an assignments is rejected if the perpendicular projection of the PS onto the bounding surface is located outside the polygon associated with this bounding surface. Note that for displaying purposes normalized distances above 10 are excluded.

C. Appendix C

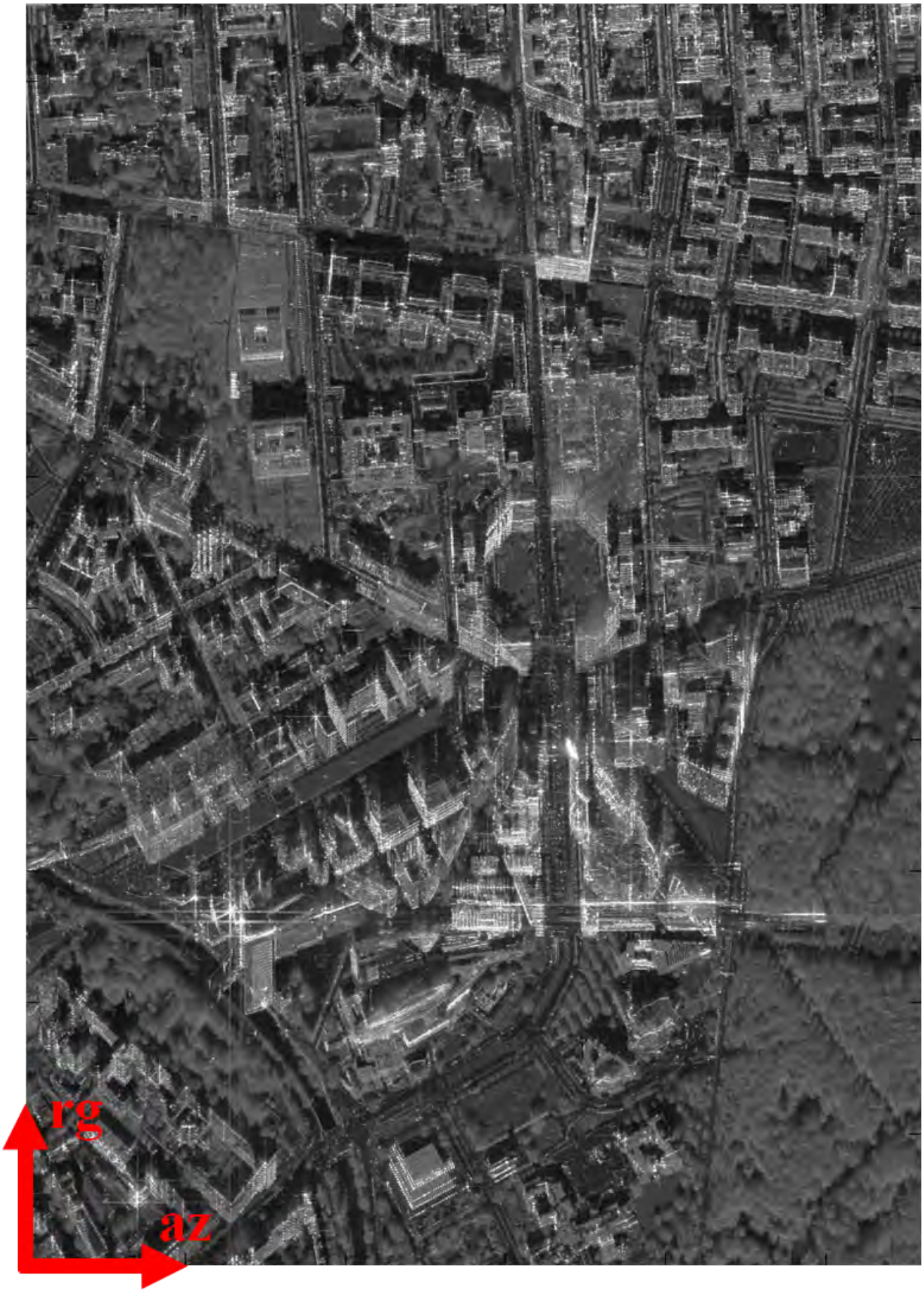

Figure C.1.: Mean amplitude map of the complete ascending dataset.

Figure C.2.: Mean amplitude map of the complete descending dataset.

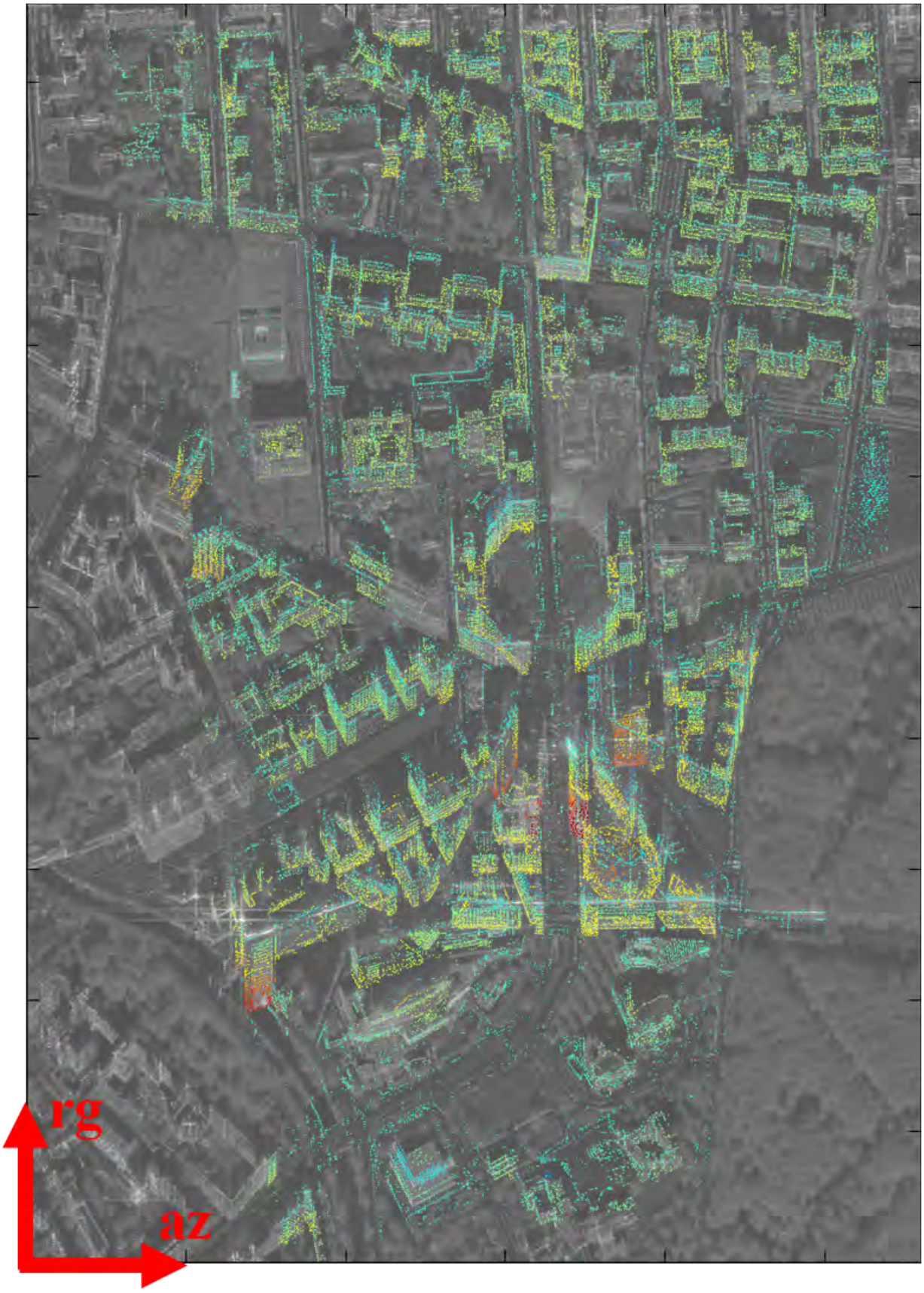

Figure C.3.: PS obtained for the complete ascending dataset overlaid to the mean amplitude map. The colors indicate the estimated PS heights (green - low to yellow - high).

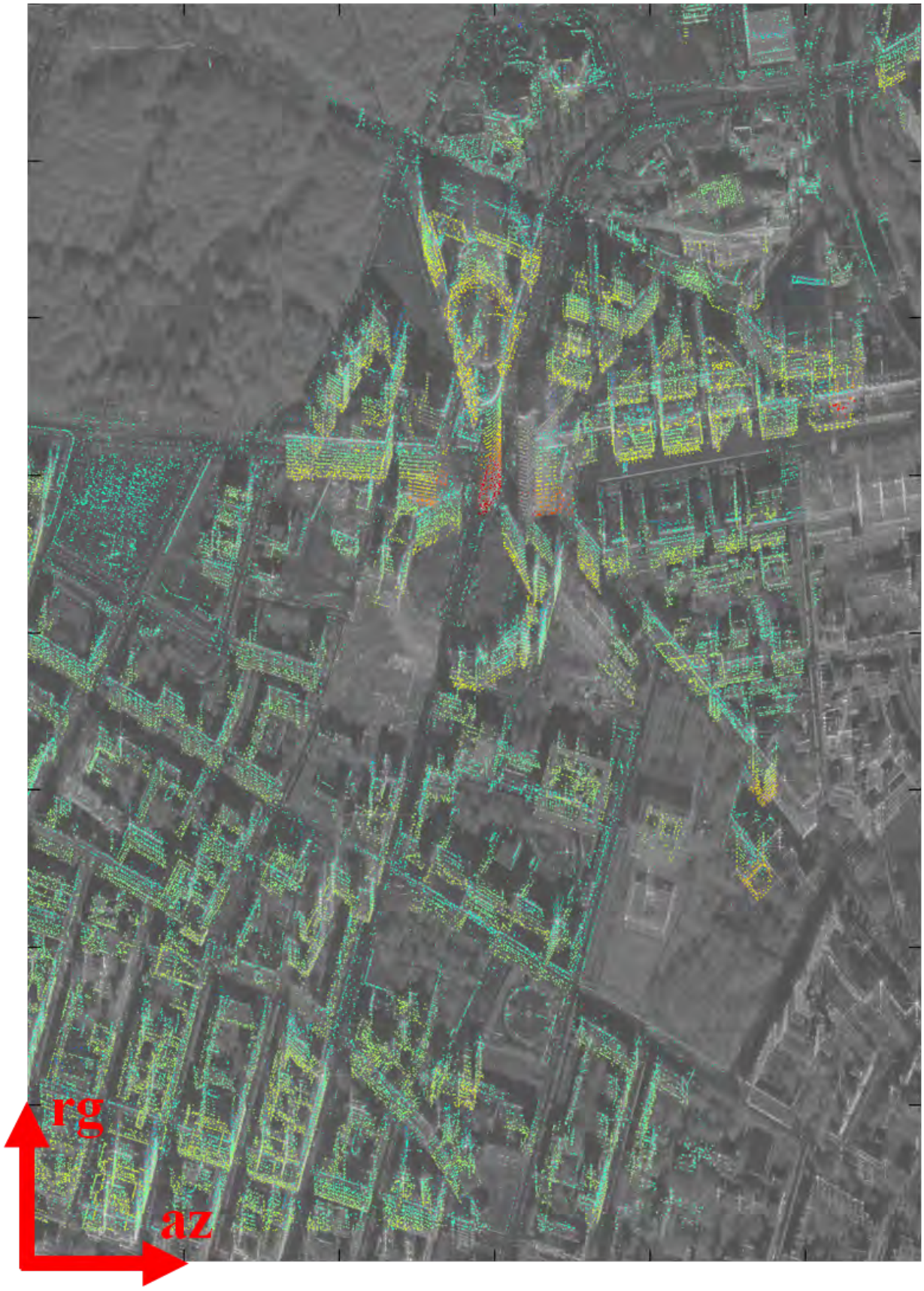

Figure C.4.: PS obtained for the complete descending dataset overlaid to the mean amplitude map. The colors indicate the estimated PS heights (green - low to yellow - high).

D. Appendix D

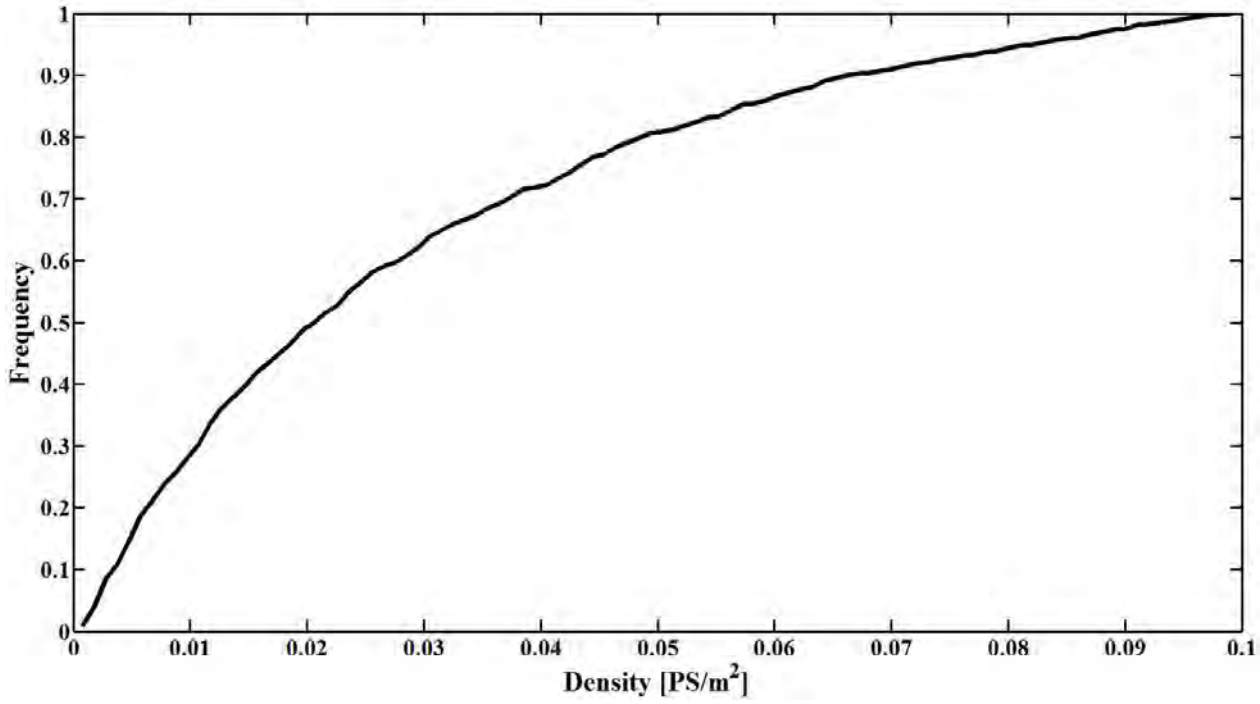

(a)

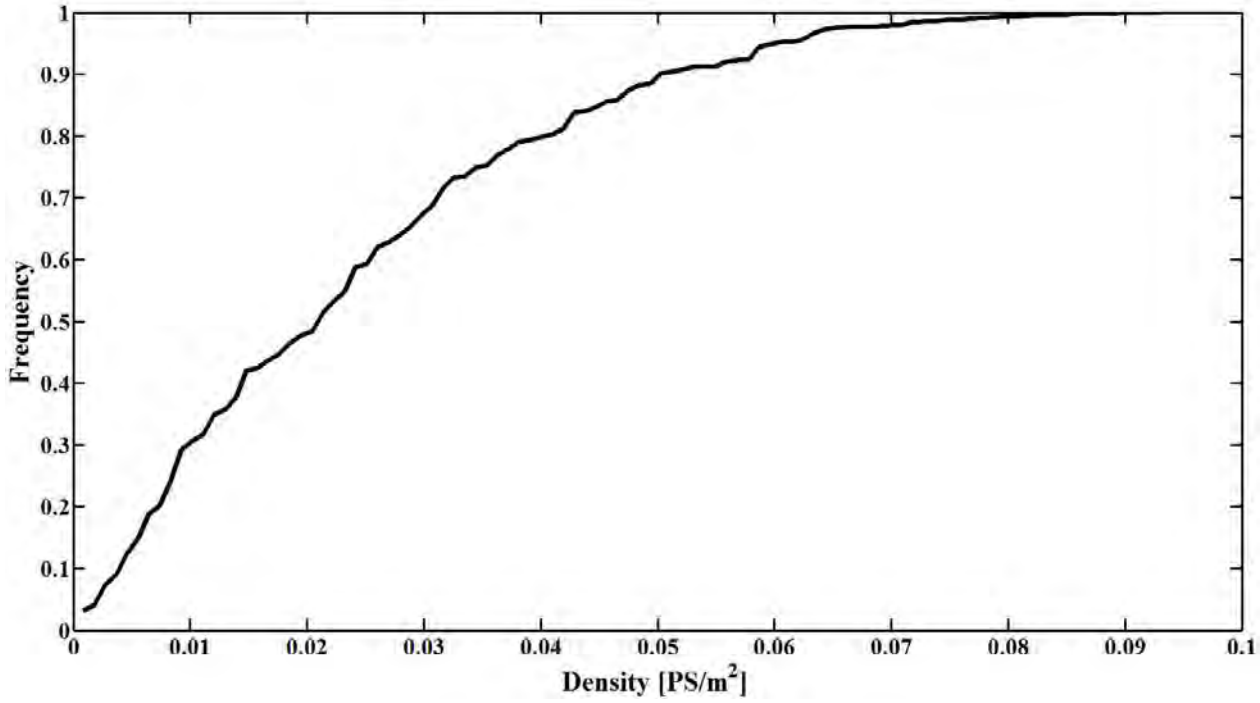

(b)

Figure D.1.: Cumulative Histograms of the PS density for the ascending dataset (b057). Facades (a) and roofs (b).

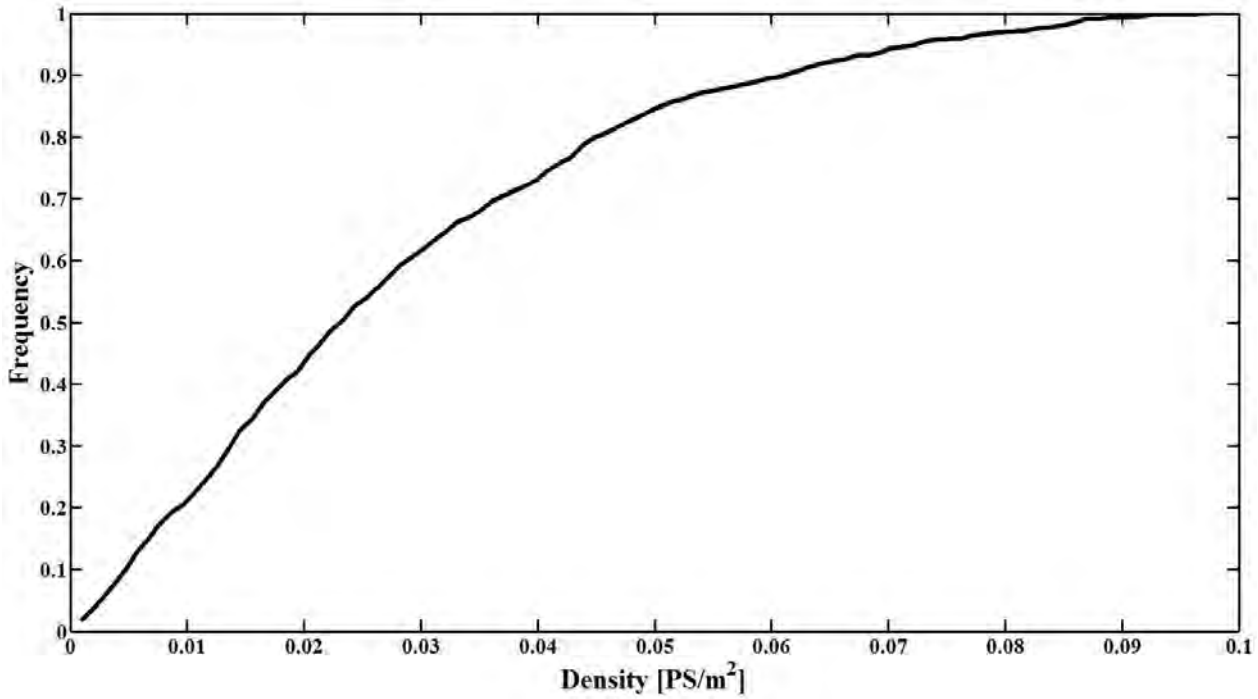

(a)

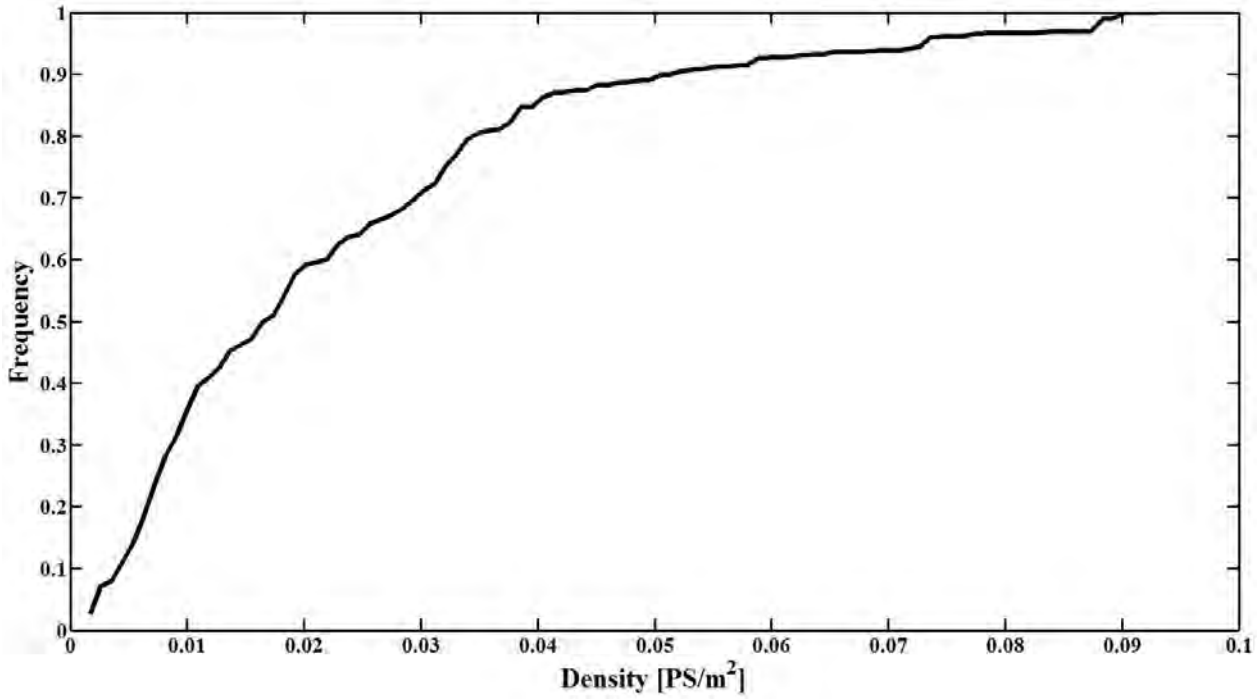

(b)

Figure D.2.: Cumulative Histograms of the PS density for the descending dataset (b042). Facades (a) and roofs (b).

List of Figures

2.1. Illustration of SAR imaging geometry 28

2.2. Left: Sketch of targets within one resolution cell that contribute to the measured signal. The arrows indicate the strength and the phase of each contribution by their length and direction, respectively. Right: Coherent summation of the signal contributions in the complex plane. While each targets contribution is approximately equal in situation (a), one target is much stronger than all others in situation (b). 30

2.3. Illustration of the three geometrical effects present in SAR images. Foreshortening appears between the points A and B, while Layover arises between the point C and D. Finally, no information is acquired between the points D and F due to shadowing. 32

2.4. Sketch of the basic principle of SAR interferometry. A point P on the Earth's surface, which is located at height h_P above the reference surface is observed. Window **win1** shows the geometrical configuration of master and slave acquisition, which are separated by a baseline B. The sensitivity of the interferometer to topography is determined by the baseline $B_\perp$ perpendicular to the range direction. Window **win2** illustrates the effect of deformation. The traversed signal path becomes longer, leading to a phase difference. Only the projection of the deformation vector δ_p into the LoS, termed δ'_P, is measured. 34

2.5. The solid line represents the CRLB of the elevation estimate as a function of the coherence for a stack characterized in table 2.1. The dashed line shows the CRLB for the b057 stack (cf. table 4.1). 41

3.1. Workflow of the grouping procedure. Image coordinates and estimated height values of the PS are determined within the PSI processing. In order to identify facades visible to the sensor in the 3D city model, the orientations of all vertical faces are compared to the sensors LoS. Facades that are oriented towards the sensor are projected to the SAR image geometry (i.e. radarcoded) and serve as prior information for the location and orientation of PS groups. The height is used to mitigate problems induced by layover. 44

3.2. (a) Acquisition of a building by a SAR sensor. The focus of attention is on the facade shown in gray with its vertices a, b, c, and d. The angle between the facade and the flight direction of the sensor is α. (b) Schematic representation of the facade in the range-azimuth geometry. The facade has the shape of a parallelogram with a shear angle of α. 45

3.3. (a) Outline of a facade (red line) and associated PS (blue dots) in range-azimuth geometry. (b) Associated PS in a coordinate system having its abscissa (X') in the direction of the outline and its ordinate in range direction. (c) Resulting density estimate (blue line) of X'-differences of PS pairs exhibiting sufficiently small range differences (i.e. smaller than $\Delta Y'_{tol}$). The blue asterisks show the available samples. The local maxima of the density estimate are marked as red asterisks. 47

3.4. Illustration of the search process. Starting from the reference PS, a search area is defined. If a PS is found therein, it is added to the group and a new search area is constructed. The process terminates if no successor is found. Since the reference PS may be located at an arbitrary X' position, the outlined process is applied equivalently to both sides. 48

3.5. (a) Estimated $\sigma_{\Delta Y'}$ as a function of the outline orientation α. Different distances in X'-direction between the two PS are shown. The distances are chosen according to typical facade lengths. (b) Estimated $\sigma_{\Delta X'}$ as a function of the outline orientation α. Different distances between the two PS are illustrated, which are chosen relative to the typical spacing of facade elements. 50

3.6. CRLB of elevation estimate for a data stack as given by table 2.1 for coherence values ranging from 0.7 to 1.0 and different group sizes (N=1,3,5,10). For comparison the CRLB of the b057 stack (cf. table 4.1) is shown in grey. 52

3.7. Simplified case of the assignment of one PS to a rectangular building, shown as a topview. The building is bordered by four vertical faces F_1 to F_4 with associated normal vectors $\mathbf{n}_1$ to $\mathbf{n}_4$. In case a PS is located within the buffered outline (indicated by a grey rectangle), all distances to the bounding surfaces of this building are evaluated. The width of the buffer is referred to as W_{ol}. The PS is associated with the closest face. 56

4.1. Map of the test site (©Microsoft®Bing™Maps), overlaid with building outlines taken from OpenStreetMaps. The red rectangle marks the area which is covered by the SAR image sections displayed in figure 4.2. 62

4.2. Mean amplitude maps of ascending (a) and descending (b) data stack. The green rectangles encompass the tower of the German railway service, which induces massive layover due to its height. The red rectangles enclose an area which is shown as a close up in figure 4.3 and figure 4.4, respectively, including the identified PS. 64

4.3. Close-up of the area framed by the red rectangles in figure 4.2 (a). (a) The PS identified in the ascending data stack overlaid with the respective section of the mean map. The colors indicate the estimated PS heights (green - low to yellow - high). The facade framed by the red rectangle is discussed in detail in figure 4.5. (b) Oblique view aerial image having approximately the same viewing direction as the SAR data in (a). 65
4.4. Close-up of the area framed by the red rectangle in figure 4.2 (b). (a) The PS identified in the descending data stack overlaid with the respective section of the mean map. The colors indicate the estimated PS heights (green - low to yellow - high). (b) Oblique view aerial image having approximately the same viewing direction as the SAR data in (a). 66
4.5. Terrestrial photograph of the facade marked by the red rectange in figure 4.3 (a) on the left and the corresponding SAR data on the right. The SAR data are rotated to approximately match the photograph. The identified PS are shown as colored points. The color indicates the height(green - low to yellow - high). The correspondence between the arrangement of windows and the lattice-like structure of the PS is clearly visible. 67
4.6. Ascending (green) and descending (red) PS displayed as topview. Most PS correspond to building structures. Facades, in particular, contain the majority of the PS. The descending data consist of approximately 35000 points, while the ascending dataset is composed of roughly 40000 points. Due to the fusion, both PS solutions are well aligned. 68
4.7. Histogram of the a-posteriori standard deviations of the elevation estimates for the descending (a) and the ascending (b) dataset. The estimates using the ascending data are more accurate due to the larger baseline span (cf. table 4.1). 69
4.8. (a): Histogram of signed distances between vertical faces (i.e. horizontal distances) and LIDAR data, (b): Histogram of signed distances between horizontal faces (i.e. vertical distances) and LIDAR data. Gaussians fitted to the histograms are shown in red. The standard deviations are 0.8 and 1.2 meters, respectively. The estimated shift has been applied before calculation of the distances. 71
4.9. Facades visible to the sensor for ascending (a) and the descending (b) dataset in the respective range-azimuth plane. The facades are depicted as colored parallelograms. In the background, the mean amplitude maps are shown. The blue dots represent the identified PS. 74
4.10. Grouping results for the ascending dataset using $\kappa = 2$ (a) and $\kappa = 3$ (b). The outlines are shown as colored line segments. The affiliated groups are indicated by connected dots of the same color. The mean amplitude image is depicted in the background. All PS located in at least one facade footprint are illustrated as blue dots. 75
4.11. Close-ups of the windows present at the facades marked by the frames in figure 4.10 (a). The numbers (1)-(3) correspond to the rectangles (1)-(3). 76

4.12. Grouping results for the descending dataset using $\kappa = 2$ (a) and $\kappa = 3$ (b). The outlines are shown as colored line segments. The affiliated groups are indicated by connected dots in the same color. The mean amplitude image is depicted in the background. All PS located in at least one facade are illustrated as blue dots. 78

4.13. The solid lines indicate the shifts estimated in the single iterations. The dashed lines represent the $\pm 2 \cdot \sigma$ intervals. The vertical axis is cut at 0.5 meters for presentation purposes. The iteration is converged after iteration 7. 80

4.14. Assignment of PS to buildings. The colors indicate the determined relations. Dark brown PS are unassigned. The used building models are shown as thin black lines. . 82

4.15. (a) PS assigned to the facades. (b) PS assigned to the horizontal bounding surfaces. The red arrow in (a) indicates the viewing direction in (b). The point colors and the black lines connecting the PS to the building faces show the affiliation. The red dashed line in (b) depicts the building surface as discernible in the LIDAR data. Note that a considerable number of LIDAR points are located underneath the roof superstructure, which is indicated by the thin red line. 84

4.16. Oblique view aerial image of the building addressed in figure 4.15 (© Microsoft Bing™Maps). 85

4.17. Unassigned PS and PS with large normalized distance (i.e. 2.5 to 3) shown as green and red points, respectively. (a) depicts a topview, while (b) shows the scene as side view. 86

4.18. (a) Side view of the building part marked in (c) by the red rectangle. The red arrow in (c) marks the viewing direction in (a). Green and red points depict the attributed and unassigned PS, respectively. The black lines show the affiliation of the PS to the faces of the building model. The building surface as discernible in the LIDAR data is displayed by the dashed blue line. The rectangles r1 and r2 distinguish the areas discussed in more detail. (b) The facade of the investigated building together with the PS relevant for area r2 are shown. The dashed lines signify PS located approximately at the same height. (c) Oblique view aerial image of the investigated building (© Microsoft Bing™Maps). 87

4.19. Oblique view aerial image (© Microsoft Bing™Maps) of the two buildings analyzed in figure 4.20. The red arrows indicate the viewing direction used in the latter depiction. 89

4.20. Comparison of the grouped PS with the facade structures present in the LIDAR data for the buildings (b1) in (a) and (b2) in (b). Either image exhibits the same scale. The viewing direction is represented by the red arrows in figure 4.19. Bold and dashed black lines depict the relevant faces of the building models. The LIDAR patterns are indicated as dotted lines and black rectangles. The latter mark location and extension of the LIDAR structures extending into the image plane. The grouped PS are depicted as red points. The colored rectangles illustrate the affiliation of the encircled PS to front or side facades (cf. table 4.3). 90

4.21. Map of PS density for the ascending (a) and the descending (b) dataset. The viewing direction roughly correspond to the LoS of the respective data stacks. The colorscales used in (a) and (b) are equal. For displaying purposes values above 0.1 PS per square meter are clipped. The numbered rectangles mark the case studies presented in the following. 93

4.22. Dependence of the PS density on the surface structure. (a) Density map of the descending PS result. (b) Corresponding oblique view aerial image (© Microsoft Bing™Maps). The two facades marked by the dashed red rectangles are completely plain which leads to a very low PS density. 94

4.23. Dependence of the PS density on the surface structure. (a) Density map of the ascending PS result. (b) Corresponding oblique view aerial image (© Microsoft Bing™Maps). The colors of the polygons in (b) indicate facades of similar structures. In (a) the correlation in density between similar facades is recognizable. 95

4.24. Impact of shadowing on the PS density. (a) Density map of the ascending PS result. The bottom part of the left building is occluded by the building on the right. Only the upper part is visible to the sensor (red rectangle), which results in a very low density (dashed red rectangle). (b) Density map of the descending result showing the other side of the building. The facade marked by the dashed red rectangle exhibits a quite high density and accommodates the same structures as the facade indicated accordingly in (a). 96

4.25. Dependence of the PS density on the aspect. (a) Density map of the ascending PS result. (b) Corresponding oblique view aerial image (© Microsoft Bing™Maps). The PS density depends on the orientation of the facade with respect to the sensor's LoS. This is nicely illustrated by the increase in point density at the facades going from right to left. 96

4.26. Influence of quasi-random processes on the PS density. (a) and (b) Density map of the ascending and the descending PS result. (c) and (d) Corresponding oblique view aerial images (© Microsoft Bing™Maps). One half of the building complex shows medium densities, while the other hardly accommodates any PS. The reason is ongoing construction during the acquisition of the data stacks. This becomes apparent from the scaffolds visible in the oblique view aerial images. 97

A.1. Definition of Heading Angle H 110

B.1. Histogram of the normalized distances for facades (a) and roofs (b) for the ascending datastack. Only those PS that are located inside at least one buffered outline are considered. Furthermore, an assignments is rejected if the perpendicular projection of the PS onto the bounding surface is located outside the polygon associated with this bounding surface. Note that for displaying purposes normalized distances above 10 are excluded. 114

B.2. Histogram of the normalized distances for facades (a) and roofs (b) for the descending datastack. Only those PS that are located inside at least one buffered outline are considered. Furthermore, an assignments is rejected if the perpendicular projection of the PS onto the bounding surface is located outside the polygon associated with this bounding surface. Note that for displaying purposes normalized distances above 10 are excluded. 115

C.1. Mean amplitude map of the complete ascending dataset. 118
C.2. Mean amplitude map of the complete descending dataset. 119
C.3. PS obtained for the complete ascending dataset overlaid to the mean amplitude map. The colors indicate the estimated PS heights (green - low to yellow - high). 120
C.4. PS obtained for the complete descending dataset overlaid to the mean amplitude map. The colors indicate the estimated PS heights (green - low to yellow - high). 121

D.1. Cumulative Histograms of the PS density for the ascending dataset (b057). Facades (a) and roofs (b). 124
D.2. Cumulative Histograms of the PS density for the descending dataset (b042). Facades (a) and roofs (b). 125

List of Tables

2.1. Table of acquisition parameters of hypothetical data stack used to illustrate the CRLB of the elevation estimate as a function of the coherence (cf. figure 2.5) 40
2.2. Numeric Values of the quantities σ_s, σ_r, and σ_a for both discussed stacks (i.e. the b057 and the hypothetical stack with parameters as displayed in table 2.1) and different coherence values. 41

4.1. Table of acquisition parameters of both SAR data stacks 63
4.2. Table of settings used for the grouping experiments 73
4.3. Mean vertical distances and corresponding error estimates for PS groups located at fronto-parallel facades (Front) and frontages perpendicular to the image plane (Side). Those are marked by blue and green rectangles in figure 4.20, respectively. 91
4.4. Mean values and standard deviations of the PS densities for both data stacks separately for facades and roofs. 94

B.1. Probability that the normalized distances are within the bounds ± 1.0, ± 2.0, or ± 3.0 for facade PS from both datastacks (cf. figure B.1 (a) and figure B.2 (a)). For comparison the corresponding values of a standard normal distribution are given. . . 113

Danksagung

Eine wissenschaftliche Arbeit ist nie das Werk einer einzelnen Person, deshalb ist es jetzt an der Zeit, mich bei allen Menschen zu bedanken, die mir die Erstellung dieser Dissertation ermöglicht haben.

Meinem Doktorvater Uwe Sörgel, der mir stets in allen Fragen zur Seite stand, gebührt mein besonderer Dank.

Weiterhin danke ich Christian Heipke und Steffen Schön für die Übernahme der Referate und die wertvollen Anmerkung, die wesentlich zur Verbesserung der vorliegenden Arbeit beigetragen haben.

Meinen Kollegen am Institut für Photogrammetrie und GeoInformation und am Fraunhofer-Institut für Optronik, Systemtechnik und Bildauswertung danke ich für die schöne Zeit und das immer freundschaftliche Miteinander.

Besonders hervorheben möchte ich Markus Even, der mich bei meinen ersten Schritten in der wissenschaftlichen Welt begleitet hat, Jan Wegner, der einen wesentlichen Anteil an meiner persönlichen Entwicklung in den letzten Jahren hatte, und Lukas Schack, der mir in den Monaten vor der Abgabe den Rücken freigehalten hat.

Schließlich gilt mein größter Dank meiner Familie und insbesondere meinen Eltern für ihre uneingeschränkte Unterstützung, ohne die diese Arbeit nicht möglich gewesen wäre.

Curriculum Vita

Personal Information

Name	**Schunert, Alexander**
Date of birth	23.02.1983 in Hildesheim, Germany

Work Experience

Dates	**Since April 2009**
Name and address of employer	Institut für Photogrammetrie und GeoInformation, Leibniz Universität Hannover, 30167 Hannover
Occupation or position held	Scientific collaborator

Dates	**October 2008 - April 2009**
Name and address of employer	Institut für Optronik und Mustererkennung (FGAN-FOM), 76275 Ettlingen
Occupation or position held	Scientific collaborator

Education and Training

Dates	**October 2003 - September 2008 Course Geodesy and Geoinformatics**
Title of qualification awarded	Diplom-Ingenieur Geodäsie und Geoinformatik
Name and type of organisation	Leibniz Universität Hannover

Dates	**September 2007 - March 2008 ERASMUS Exchange**
Name and type of organisation	University College London (UCL)

Dates	**1989 - 2002 High School**
Title of qualification awarded	Allgemeine Hochschulreife
Name and type of organisation	Grundschule Banteln, CJD Elze, Gymnasium Alfeld